STARS

Electronic Theses and Dissertations, 2004-2019

2004

Polarimetric Characterization Of Random Electromagnetic Beams And Applications
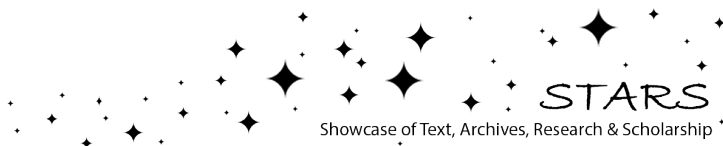
Mircea Mujat
University of Central Florida

University of Central Florida

STARS
Showcase of Text, Archives, Research & Scholarship

www.manaraa.com

POLARIMETRIC CHARACTERIZATION
OF RANDOM ELECTROMAGNETIC BEAMS
AND APPLICATIONS

by

MIRCEA MUJAT
B.S. University of Bucharest, 1994
M.A. Temple University, 1998
M.S. University of Central Florida, 2001

A dissertation submitted in partial fulfillment of the requirements
for the degree of Doctor of Philosophy
in the School of Optics
at the University of Central Florida
Orlando, Florida

Spring Term
2004

ABSTRACT

Polarimetry is one of the principal means of investigating the interaction of light with matter. Theoretical models and experimental techniques are presented in this dissertation for polarimetric characterization of random electromagnetic beams and of signatures of random media in different scattering regimes and configurations.

The degree of polarization rather than the full description of the state of polarization is of interest in multiple scattering and free space propagation where the statistical nature and not the deterministic component of light bears the relevant information. A new interferometric technique for determining the degree of polarization by measuring the intensity fluctuations in a Mach-Zehnder interferometric setup is developed. For this type of investigations, one also needs a light source with a controllable degree of polarization. Therefore, also based on a Mach-Zehnder interferometer, we proposed a new method for generating complex random electromagnetic beams. As a direct application of the cross-spectral density matrix formalism, it is shown that the spectral and the polarimetric characteristics of light can be controlled by adjusting the correlations between parallel components of polarization propagating through the two arms of the interferometer.

When optical beams are superposed in the previous applications it is desirable to understand how their coherence and polarimetric characteristics are combined. A generalization of the interference laws of Fresnel and Arago is introduced and as a direct application, a new imaging polarimeter based on a modified Sagnac interferometer is demonstrated. The system allows full

ii

polarimetric description of complex random electromagnetic beams. In applications such as active illumination sensing or imaging through turbid media, one can control the orientation of the incident state of polarization such that, in a given coordinate system, the intensities are equal along orthogonal directions. In this situation, our novel interferometric technique has a significant advantage over standard Stokes imaging polarimetry: one needs only one image to obtain both the degree of polarization and the retardance, as opposed to at least three required in classical Stokes polarimetry.

The measurement of the state of polarization is required for analyzing the polarization transfer through systems that alter it. Two innovative Mueller matrix measurement techniques are developed for characterizing scattering media, either in quasi real-time, or by detection of low level signals. As a practical aspect of Mueller polarimetry, a procedure for selecting the input Stokes vectors is proposed.

The polarimetric signatures of different particulate systems are related to their structural properties and to the size distribution, shape, orientation, birefringent or dichroic properties of the particles. Various scattering regimes and different geometries are discussed for applications relevant to the biomedical field, material science, and remote sensing. The analysis is intended to elucidate practical aspects of single and multiple scattering on polydisperse systems that were not investigated before.

It seems to be generally accepted that depolarization effects can only be associated to multiple scattering. It is demonstrated in this dissertation that depolarization can also be regarded as an indication of polydispersity in single scattering.

In order to quantify the polarizing behavior of partially oriented cylinders, the polarization transfer for systems consisting of individual layers of partially aligned fibers with different

degrees of alignment and packing fractions is also analyzed in this dissertation. It is demonstrated that a certain degree of alignment has the effect of a partial polarizer and that the efficiency of this polarizer depends on the degree of alignment and on the packing fraction of the system.

In specific applications such as long range target identification, it is important to know what type of polarization is better preserved during propagation. The experimental results demonstrate that for spherical particles smaller than the wavelength of light, linear polarization is better preserved than circular polarization when light propagates through turbulent media. For large particles, the situation is reversed; circular polarization is better preserved. It is also demonstrated here that this is not necessarily true for polyhedral or cylindrical particles, which behave differently.

Optical activity manifests as either circular birefringence or circular dichroism. In this dissertation, a study is presented where both the effect of optical activity and that of multiple scattering are considered. This situation is relevant for medical applications and remote sensing of biological material. It is demonstrated here that the output state of polarization strongly depends on the optical density of the scattering medium, the optical rotatory power and the amount of circular dichroism associated to the scattering medium. This study shows that in the circular birefringence case, scattering and optical activity work together in depolarizing light, while in the dichroic case the two effects compete with each other and the result is a preservation of the degree of polarization.

To characterize highly diffusive media, a very simple model is developed, in which the scattering is analyzed using the Mueller matrix formalism in terms of surface and volume contributions.

ACKNOWLEDGEMENTS

I wish to acknowledge the contribution to this dissertation of my advisor, Dr. Aristide Dogariu, who made this entire endeavor possible. I am indebted to him for opening to me the exciting and rich field of polarimetry.

I am grateful to Professor Emil Wolf for his continuous support and encouragement while working together on some of the subjects presented here.

I extend my appreciation to all the committee members for their advice and for taking their time to be part of this.

I had a lot of help and positive interaction with all the members of the Random group.

The School of Optics has been an ideal place for education and research, and I will rely on all of my experiences here to develop my career path in optics and academia. I learned a lot from all my teachers in CREOL, and it has been a lot of fun to interact with most of the CREOL students in a very friendly and diverse environment.

Last but not least, maybe the most important, I am grateful for my family's support along the way.

TABLE OF CONTENTS

LIST OF FIGURES

x

LIST OF TABLES

LIST OF SYMBOLS

a – particle radius, $[a] = m$;

B – magnetic field, $[B] = T$;

C – contrast of intensity fluctuations;

d – depolarization coefficient; also thickness of the scattering medium, $[d] = m$;

D – depolarization index;

D – diattenuation;

DC – DC component of the photocurrent, $[DC] = A$;

e – electric field amplitudes, $[e] = V/m$;

$\mathbf{E}$ – electric field vector, $[\mathbf{E}] = V/m$ **;**

E – electric field components, $[E] = V/m$;

f – phase factor; also modulation frequency, $[f] = Hz$;

g – anisotropy factor;

h – height, $[h] = m$;

i – photocurrent, $[i] = A$;

I – intensity, $[I] = V^2/m^2$; also Fourier components of the photocurrent, $[I] = A$;

ΔI – intensity fluctuation, $[\Delta I] = V^2/m^2$;

j_i – Jones matrix components, i=1-4;

J – polarization, coherence, covariance matrix; also Bessel function;

k – wave number, $[k] = m^{-1}$;

l – scattering mean free path, $[l] = m$;

l^* – transport mean free path mean free path, $[l^*] = m$;

L – characteristic length, $[L] = m$;

m – normalized Mueller matrix elements;

M – Mueller matrix;

n – refractive index;

n' – imaginary part of the refractive index;

OD – optical density;

p_e – probability;

P – degree of polarization; also Jones matrix of a polarizer;

$P(s)$ – optical path-length probability density, $[P(s)] = m^{-1}$;

$P(\varepsilon)$ – slope probability density, $[P(\varepsilon)] = rad^{-1}$;

PL, PC – degree of polarization of the scattered light for linear, circular input;

q – normalized second Stokes vector component;

Q – second Stokes vector component, $[Q] = V^2/m^2$;

r – intensity ratio; also complex Fresnel reflection coefficients;

$\mathbf{r}$ – position vector, $[\mathbf{r}] = m$;

R – Jones matrix of a rotator; also relative position vector, $[R] = m$; also ratio PL/PC ;

s – optical path-length, $[s] = m$;

S – Stokes vector; also spectral density;

SNR – signal to noise ratio;

t – time, $[t] = s$;

T – Jones matrix;

u – normalized third Stokes vector component;

U – third Stokes vector component, $[U] = V^2/m^2$;

v – normalized forth Stokes vector component;

V – forth Stokes vector component, $[V] = V^2/m^2$; also volume of a tetrahedron inscribed in the Poincare sphere; also Verdet constant, $[V] = m^{-1}T^{-1}$;

W – cross-spectral density matrix;

$\hat{\mathbf{x}}, \hat{\mathbf{y}}$ – unit vectors;

z_0 – extrapolation length;

α – angle, $[\alpha] = rad$; also attenuation coefficient, $[\alpha] = m^{-1}$; also rotary power, $[\alpha] = rad./m$;

β – phase, $[\beta] = rad$; also dichroism, $[\beta] = \deg./cm$;

ε – angle, $[\varepsilon] = rad$;

γ – complex degree of coherence;

Γ – full width half maximum, $[\Gamma] = rad$;

δ – retardance, $[\delta] = rad$; also angle, $[\delta] = \deg$;

δ_o – linear birefringence;

δ_c – circular birefringence;

θ – angle, $[\theta] = rad$;

λ – wavelength, $[\lambda] = nm$; also eigenvalue;

φ – phase, also ellipticity, $[\varphi] = rad$;

Δ – phase difference, also ellipsometric angle, $[\Delta] = rad$;

Ψ – ellipsometric angle, $[\Psi] = rad$;

μ – spectral degree of coherence of the electric field;

μ_{xy} – complex degree of coherence of the electric vibrations in the x and y directions;

ρ – angle, $[\rho] = rad$;

σ – variance, standard deviation of intensity fluctuations, $[\sigma] = V^2/m^2$; also rms roughness, $[\sigma] = m$;

σ_i – Pauli spin matrices, i=0..3;

ω – optical angular frequency, $[rad/s]$; also angular frequency, $[rad/s]$;

ψ – phase, $[\psi] = rad$;

CHAPTER 1

INTRODUCTION

The measurement of light polarization is one of the principal means of investigating the interaction of light with matter. All scattering processes lead to changes of polarization properties of light.

A brief, chronological review of the milestones in polarimetry is given here. The interference laws of Fresnel and Arago,[1] derived from experimental observations of interference with polarized light, were explained by Stokes using the assumption that light vibrations are transversal to the direction of propagation. Stokes was trying to mathematically describe unpolarized light, and as a result, he developed the four "Stokes parameters" (even before Maxwell formulated his theory) for complete description of the state of polarization.[2] The geometrical representation of pure states of polarization on the "Poincarè sphere" was introduced by Poincarè. Jones introduced the "Jones calculus"[3] for representation and transfer of pure states of polarization. Mueller formulated his calculus[4] based on the work done by Soleillet who pointed out that Stokes vectors transform linearly, and by Perrin that showed that the linear relations can be put in matrix form. The polarization matrix, also known as coherence matrix,[5] was introduced by Wiener[6] and by Wolf[7] to completely describe the state of polarization in a close relation to quantum mechanics. Very recently, the cross-spectral density matrix formalism was developed by Wolf,[8] de-

1

riving the polarimetric, spectral and coherence properties from a common mathematical description of random electromagnetic fields.

The basic concepts and notations of the Jones, Stokes-Mueller, polarization matrix, and cross-spectral density matrix formalisms used for the description of random electromagnetic beams and of polarization transfer are reviewed below. References to these definitions will be made throughout this dissertation.

1.1. Jones calculus

The Jones vector[3] $\mathbf{E} = \begin{bmatrix} E_x \\ E_y \end{bmatrix} = \begin{bmatrix} e_x \\ e_y e^{i\delta} \end{bmatrix}$ completely describes pure states of polarization and the total intensity of the beam ($I = e_x^2 + e_y^2$) using three parameters (the field amplitudes e_x, e_y and the retardance δ). The spatial and the temporal/spectral characteristics of the light field were left aside here. Only two parameters, the ratio of the field amplitudes e_x/e_y and the retardance δ, are needed to graphically represent a pure state of polarization in the ellipse representation. Non-image forming optical devices, for which the light beam enters and emerges as plane wave, are represented by a 2x2 transformation matrix T,

$$T = \begin{bmatrix} j_1 & j_2 e^{i\delta_2} \\ j_3 e^{i\delta_3} & j_4 e^{i\delta_4} \end{bmatrix} \tag{1}$$

usually known as the Jones matrix.[3] The elements of the Jones matrix have deterministic and complex values, dealing only with transformations of pure states of polarization into pure states of polarization. By its nature, the Jones calculus cannot describe either partially polarized light or random, depolarizing media.

2

An important advantage of the Jones formalism is that it deals with field amplitudes and phases and can be directly applied to interference phenomena. It allows for coherent addition of fields for analyzing interference of coherent light beams in interferometric setups. Of course, incoherent addition of intensities is just a particular case here. An important disadvantage is that it does not make use of measurable quantities, however, all parameters can be retrieved from measurements of total intensities in various polarimetric configurations using retarders and polarizers.

1.2. Stokes-Mueller formalism

The state of polarization of light can be completely described by the Stokes vector $S = \{I, Q, U, V\}^T$.[2] The four Stokes vector components are defined as follows:

$$
\begin{aligned}
I &= I_x + I_y = e_x^2 + e_y^2 \\
Q &= I_x - I_y = e_x^2 - e_y^2 \\
U &= I_{45°} - I_{-45°} = 2e_x e_y \cos(\delta) \\
V &= I_l - I_r = 2e_x e_y \sin(\delta),
\end{aligned}
\tag{2}
$$

where e_x, e_y are the electric field amplitudes, δ is the phase difference between orthogonal electric field components. A polarizer oriented horizontal (x), vertical (y) or at $\pm 45°$ would let to pass through light with intensity $I_{x/y}$ or $I_{45°/-45°}$ as components of linear polarization along x, y or $\pm 45°$ directions, while a quarter-wave plate followed by a polarizer oriented at $\pm 45°$ with respect to the slow axis of the waveplate would transmit $I_{l/r}$ as the intensities of left and right components of circular polarization. It is important to notice that the

3

sum of the intensities of any two orthogonal components gives the total intensity I which is the first component of the Stokes vector: $I_x + I_y = I_{45°} + I_{-45°} = I_l + I_r = I$.

Sometimes, it is convenient to normalize the Stokes vector to the total intensity

$$q = \frac{Q}{I}; \ u = \frac{U}{I}; \ v = \frac{V}{I}; \ S = \{1, q, u, v\}^T, \tag{3}$$

and to define a degree of polarization P

$$P = \frac{\sqrt{Q^2 + U^2 + V^2}}{I} = \sqrt{q^2 + u^2 + v^2} \tag{4}$$

that measures the fraction of the light which is polarized; $P = 1$ represents pure state of polarization, $P = 0$ corresponds to natural, unpolarized light, while $0 < P < 1$ describes partially polarized light. The Stokes vector cannot be made of any combination of four numbers; only those combinations of four real numbers that satisfy the so-called "Stokes criterion", $0 \leqslant P \leqslant 1$, can be associated to a state of polarization of light.

The state of polarization can be graphically illustrated as an ellipse as well as on the Poincarè sphere, alternative representations that will also be used here.

The interaction of light (input Stokes vector S_{in}) with an object (or scattering system) could result in a change of the state of polarization. The transfer function that describes this change is represented by a real 4x4 matrix M, called Mueller matrix. The output Stokes vector S_{out} is then given by $S_{out} = MS_{in}$.[4] If the light passes through a cascaded system, each part of the system being described by an individual matrix M_i, then the output state of polarization is simply given by $S_{out} = M_n..M_2M_1S_{in}$. A physically meaningful Mueller matrix must allow S_{out} to satisfy the Stokes criterion for any S_{in}, however, the degree of polarization of the output state could be different from the

degree of polarization of the input state. For instance, a polarizer would increase P, while multiple scattering in a particulate system will tend to decrease it. For scattering media, the dependence on wavelength of the incident light, scattering angle, size, shape and orientation of the scatterers, concentration of the sample, and the complex refractive index of the scatterers relative to the medium are all contained in the Mueller matrix associated with that medium, and are well described in literature for single scattering regime;[9–12] the Mueller matrix contains all the information that can be retrieved optically from a scattering sample.

The depolarization index[13]

$$D = \frac{1}{M_{11}^2} \sum_{i,j=1}^{4} M_{ij}^2 = \sum_{i,j=1}^{4} m_{ij}^2, \tag{5}$$

where $m_{ij} = M_{ij}/M_{11}$ (i,j=1..4) are the normalized Mueller matrix elements, provides useful information about the global depolarization characteristics of a transfer system; $D = 4$ meaning an interaction with no depolarization effects, while $D = 1$ characterizes a total depolarizer.

For reference, the Mueller matrices for the standard objects, most commonly used in polarization investigations: polarizer, quarter-wave and half-wave plate, and variable retarder are presented below.

The Mueller matrix of a polarizer at an angle θ is[14]

$$M_{pol}(\theta) = \frac{1}{2} \begin{bmatrix} 1 & \cos(2\theta) & \sin(2\theta) & 0 \\ \cos(2\theta) & \cos^2(2\theta) & \frac{1}{2}\sin(4\theta) & 0 \\ \sin(2\theta) & \frac{1}{2}\sin(4\theta) & \sin^2(2\theta) & 0 \\ 0 & 0 & 0 & 0 \end{bmatrix}. \tag{6}$$

5

A quarter-wave plate at an angle ρ is described by

$$M_{\lambda/4}(\rho) = \begin{bmatrix} 1 & 0 & 0 & 0 \\ 0 & \frac{1+\cos(4\rho)}{2} & \frac{\sin(4\rho)}{2} & -\sin(2\rho) \\ 0 & \frac{\sin(4\rho)}{2} & \frac{1-\cos(4\rho)}{2} & \cos(2\rho) \\ 0 & \sin(2\rho) & -\cos(2\rho) & 0 \end{bmatrix}, \tag{7}$$

while a retarder with retardance δ is characterized in its coordinate system by

$$M_w(\delta) = \begin{bmatrix} 1 & 0 & 0 & 0 \\ 0 & 1 & 0 & 0 \\ 0 & 0 & \cos(\delta) & \sin(\delta) \\ 0 & 0 & -\sin(\delta) & \cos(\delta) \end{bmatrix}. \tag{8}$$

The Mueller matrix of a rotator (half wave-plate) is given by

$$M_{\lambda/2}(\rho) = \begin{bmatrix} 1 & 0 & 0 & 0 \\ 0 & \cos(4\rho) & \sin(4\rho) & 0 \\ 0 & \sin(4\rho) & -\cos(4\rho) & 0 \\ 0 & 0 & 0 & -1 \end{bmatrix} \tag{9}$$

where $\rho = \theta/2$ is the orientation of the retarder and θ is the rotation of a linear input.

Jones calculus and Mueller calculus have much in common. Both describe the state of polarization in a vector form and its transformation in a matrix form. In both calculi there is a fixed routine in which matrices and vectors are multiplied following the elementary rules of matrix algebra. There are, however, important differences. The Mueller calculus can handle problems involving depolarization, while the Jones calculus cannot. The Jones calculus allows one to preserve information as to absolute phase, while the Mueller calculus

6

cannot. The Jones calculus follows the evolution of the electric field amplitudes, while the Mueller calculus considers combinations of intensities. This way, the Jones calculus is well suited to combining beams that are coherent, while the Mueller calculus can do that with great difficulty. The Jones matrix contains no redundancy in the non-depolarizing case, while in the Mueller matrix only seven elements out of sixteen are independent.

Mueller matrix polarimetry is becoming a more and more important tool in investigating the characteristics of various scattering media. Without attempting to be comprehensive, notable areas were Mueller matrix polarimetry has been successfully utilized in light scattering by small particles are biomedical field,[15–22] marine and submarine environment,[23–25] polymer science,[26,27] remote sensing,[28–31] magneto-optics[32] spatiotemporal strain mapping in experimental mechanics.[33]

1.3. Polarization matrix formalism

The polarization matrix J, also known as the *coherence* or the *covariance* matrix,[7,34] is given by

$$J = \begin{bmatrix} \langle E_x^* E_x \rangle & \langle E_x^* E_y \rangle \\ \langle E_y^* E_x \rangle & \langle E_y^* E_y \rangle \end{bmatrix}, \tag{10}$$

where E_i $(i = x, y)$ are statistically fluctuating orthogonal field components as random variables described by an ensemble, which we shall assume to be stationary, and $\langle ... \rangle$ denotes ensemble averaging. The polarization matrix completely describes the state of polarization of a plane wave. The degree of polarization can be expressed in terms of the unitary invariants (independent of the coordinate system) of the J matrix, namely the

7

determinant (det) and trace (Tr) of J in the form

$$P = \sqrt{1 - 4\frac{\det J}{(TrJ)^2}}. \tag{11}$$

TrJ represents in fact the total intensity of the beam.

The intensity of a wave passing through a compensator (which introduces a delay δ) and a polarizer (oriented at an angle θ with the x-axis) can be expressed in terms of the incident polarization matrix J as

$$I(\theta, \delta) = J_{xx}\cos^2\theta + J_{yy}\sin^2\theta + J_{xy}\sin\theta\cos\theta\exp(-i\delta) + J_{yx}\sin\theta\cos\theta\exp(i\delta). \tag{12}$$

This can be rearranged as

$$I(\theta, \delta) = J_{xx}\cos^2\theta + J_{yy}\sin^2\theta + 2\sqrt{J_{xx}J_{yy}}\sin\theta\cos\theta\,|\mu_{xy}|\cos(\beta_{xy} - \delta) \tag{13}$$

where

$$\mu_{xy} = |\mu_{xy}|\exp(i\beta_{xy}) = \frac{J_{xy}}{\sqrt{J_{xx}J_{yy}}} \tag{14}$$

represents the complex degree of coherence of the electric vibrations in the x and y directions. The absolute value $|\mu_{xy}|$ is a measure of the degree of correlation of the vibrations and its maximum value is equal to the degree of polarization P of the wave. The Eq. 13 is formally identical with the basic interference law of partially coherent fields.

There is a direct relationship between the polarization matrix and the Stokes vector in the form

$$J = \frac{1}{2}\sum_{i=0}^{3} S_i\sigma_i \tag{15}$$

where σ_0 is the unit 2x2 matrix and σ_i $(i = 1..3)$ are the Pauli spin matrices. All properties of the polarization matrix can be extended this way to the Stokes vector.

8

A deterministic, non-depolarizing, non-imaging optical device described by a Jones matrix T will affect the polarization matrix according to the transformation

$$J' = T J T^{\dagger} \tag{16}$$

where $T^{\dagger}$ is the Hermitian adjoint (transpose conjugate) of T. There are, however, linear optical systems that cannot be described by a single Jones matrix or a transformation given by Eq. 16. Depolarizing systems can be described by an ensemble of Jones matrices $T^{(e)}$ assumed to occur with a probability p_e.[35] The transformation of the polarization matrix is given in this case by the ensemble averaging

$$J' = \sum_e (p_e T^{(e)} J T^{(e)\dagger}) = \left\langle T^{(e)} J T^{(e)\dagger} \right\rangle_e. \tag{17}$$

In principle, this procedure permits the description of depolarizing systems using Jones matrices. However, there is no unique way for constructing the ensemble of Jones matrices, as compared to the Mueller matrix of a depolarizing system, which is uniquely determined.

The polarization matrix formalism can easily handle partially polarized waves and their transfer through linear optical systems, and also deals with measurable quantities, since the polarization matrix elements appear naturally as intensity coefficients in the analysis of a simple experiment. However, interference of partially polarized waves cannot be easily described since the elements of the polarization matrix are already ensemble averaged.

9

1.4. Cross-spectral density matrix

The second-order coherence properties of a random electromagnetic field are characterized by the cross-spectral density matrix[8]

$$W(\mathbf{r}_1, \mathbf{r}_2, \omega) = \begin{bmatrix} \langle E_x^*(\mathbf{r}_1, \omega) E_x(\mathbf{r}_2, \omega) \rangle & \langle E_x^*(\mathbf{r}_1, \omega) E_y(\mathbf{r}_2, \omega) \rangle \\ \\ \langle E_y^*(\mathbf{r}_1, \omega) E_x(\mathbf{r}_2, \omega) \rangle & \langle E_y^*(\mathbf{r}_1, \omega) E_y(\mathbf{r}_2, \omega) \rangle \end{bmatrix}, \tag{18}$$

where the angular brackets $\langle ... \rangle$ represent ensemble average, and * stands for complex conjugate. Particularized to one point, the cross-spectral density matrix reduces to the coherence matrix[7] given by the Eq. 10 that completely describes the state of polarization of light, and the spectral degree of polarization is calculated as

$$P(\mathbf{r}, \omega) = \sqrt{1 - 4 \frac{\det W(\mathbf{r}, \mathbf{r}, \omega)}{Tr^2[W(\mathbf{r}, \mathbf{r}, \omega)]}}. \tag{19}$$

Also in one point, the trace of W represents the spectral density (the spectrum of light)

$$S(\mathbf{r}, \omega) = Tr[W(\mathbf{r}, \mathbf{r}, \omega)]. \tag{20}$$

From the cross-spectral density matrix, the spectral degree of coherence of the electric field can also be obtained

$$\mu(\mathbf{r}_1, \mathbf{r}_2, \omega) = \frac{Tr[W(\mathbf{r}_1, \mathbf{r}_2, \omega)]}{\sqrt{Tr[W(\mathbf{r}_1, \mathbf{r}_1, \omega)] Tr[W(\mathbf{r}_2, \mathbf{r}_2, \omega)]}}, \tag{21}$$

and quantifies the ability of light originating from two points of the field at $\mathbf{r}_1$ and $\mathbf{r}_2$ to interfere.

The state polarization (in particular the degree of polarization) and the spectral density cannot be predicted as a result of propagation since they are defined as one point

10

quantities. The cross-spectral density matrix W, however, depends on two spatial arguments, and also satisfies two Helmholtz equations of the form

$$\nabla_i^2 W(\mathbf{r}_1, \mathbf{r}_2, \omega) + k^2 W(\mathbf{r}_1, \mathbf{r}_2, \omega) = 0, \tag{22}$$

where ∇_i^2 is the Laplacian operator acting with respect to $\mathbf{r}_i$ $(i = 1, 2)$. Knowing the cross-spectral density matrix W in the source plane, one can predict the spectral degree of coherence μ, the spectral density S, and the spectral degree of polarization P in a new plane by propagating W first to the new plane and then calculating μ, S, and P in the new plane.

The formalism used in a certain analysis is generally selected based on the complexity of the problem. Transfer of pure polarization through non-depolarizing systems is simply analyzed with the Jones formalism. When depolarization is involved, Stokes-Mueller and polarization matrix formalisms can be used equivalently. The cross-spectral density matrix is required if spectral and coherence properties are also of interest, and for prediction of field properties in propagation. In the subsequent Chapters, the formalism is selected to appropriately describe each specific case.

<u>1.5. Applications of polarized light scattering</u>

Scattering problems that can be solved without explicit reference to the state of polarization of the incident and scattered light are not often encountered. On the other hand, there are many applications of polarized light scattering, and some of the most important are mentioned below.

11

1.5.1. Optical medical diagnostics

In medical applications, polarization-based optical properties of tissues are very important in noninvasive medical diagnostics. In dermatology, detection of skin cancer[36,37], as well as discrimination between normal and cancerous tissue (moles), and identification of Lupus lesions,[38,39] are possible using Mueller matrix imaging polarimetry. Currently, the only available method to diagnose the suspected cancerous tissue (skin cancer) is surgical biopsy.[36]

Real-time measurement of skin stretch and estimation of stresses are required in wound closure, healing and scar tissue formation,[40] as well as in plastic surgery. A noninvasive investigation method is desired. Currently available methods are direct contact and ultrasonic imaging.[41] Tissue structure changes under strain are visible as birefringence variations in polarimetric images.

Birefringence is related to various biological components like collagen fibers, muscle fibers, keratin, and glucose. Measurement of form birefringence helps in structural characterization of retina and other tissues. Retinal polarization imaging reveals valuable information about diabetes and other diseases that could lead to blindness; measuring the blood oxygen saturation in the large vessels of the retina near the optic disc improves the chances of early detecting diabetic retinopathy.[42] The spatial distribution of the complex index of refraction can be determined from diattenuation and retardance images,[39] providing a new contrast mechanism for medical imaging.[43,44]

In addition to polarimetry,[45] significant efforts have been made to develop a noninvasive blood glucose sensor by use of optical approaches, including near-infrared absorp-

12

tion spectroscopy, near-infrared scattering measurements, Raman spectroscopy, photoacoustics, and OCT.[46]

1.5.2. Biology

Optical activity measurements have routinely been performed by chemists and biologists for more that a century, but only on clear solutions. Measurements on optically active particles are still to be done. Glucose is the major carbohydrate energy source that is utilized by living organisms. The ability to noninvasively detect glucose concentrations in biological media provides fascinating possibilities in the field of analytical chemistry and biosensing in areas like cell culture bioreactors (used in tissue engineering). However, scattering cannot be neglected for bioparticles like red blood cells membranes, viruses nuclei, mitochondria and ribosomes. One cannot dilute such media without destroying their structural elements.[47] Measuring noninvasively optical activity effects in such systems is very important.

Microbiologists are concerned with rapid and unambiguous identification of different microorganisms.[48] Conventional methods are time consuming and expensive. Several researchers have found that unique signatures can be gathered for particular microorganisms from polarized scattering measurements.[16,17,49] There is also an increasing interest in microbiology in determining how bacteria are able to rapidly adjust their physical parameters to changing growth conditions. Size distribution for a population of rod-shape cells can be measured in real-time and in-vivo.[21] Routine use of structural investigations is desired in clinical bacteriology.

13

Marine environment contains very diverse types of particles, like marine chlorella and phytoplankton, with interesting characteristics (core-shell structure, nonspherical, optically active) that can be retrieved from polarized scattering.[25]

Honeybee, anthropoids, squid and octopuses have eyes sensitive to polarized light. They use it either for orientation or for a better visualization of the environment through polarization difference imaging (cross polarized channels).[29]

1.5.3. Remote sensing

Here are some of the most important remote sensing applications of Mueller matrix imaging polarimetry: target identification, discrimination between natural and man-made targets based on depolarization characteristics,[28, 29] shape and orientation determination of a target,[30] detection of biological contamination, target acquisition and mine detection in infrared.[31]

Polarization imaging techniques offer the distinct possibility of yielding images with higher inherent visual contrast than normal techniques.[50] The performance of a polarization imager can be improved by using active illumination. Recent research on linear polarization difference imaging[51] demonstrated that ranges 2-3 times greater than in conventional intensity imaging in scattering suspensions could be achieved.

In astronomy and astrophysics a great deal of knowledge can be obtained by analyzing the radiation scattered by particles in the atmosphere of planets and satellites, planetary ring systems, interplanetary dust cloud, circumstellar matter and interstellar medium.[52]

1.5.4. Industry and research

The shape of particles and their orientation in space are of importance in the manufacture of aerosols, pharmaceuticals, paints and coatings, and to applications in remote sensing and imaging through obscuring random media.[53]

Nondestructive, noninvasive and fast light scattering techniques have been used in quality control for defects identification. This gives excellent results for monodisperse, homogeneous and dilute suspensions of spheres. However, if the particles become non-spherical, have a complex size distribution, are composed of different layers or are in concentrated solutions, the mean size calculated by the commercial particle sizing instruments can be very different from the real mean size. Several scattering geometries can give the same intensity pattern,[54] and, therefore, polarization sensitivity is required to extract the correct information from the scattering measurements.

Optical rotation and circular dichroism measurements on transparent and weakly absorbing samples have been employed to provide information on the identity, electronic structure, stereochemistry, and concentration of constituent chiral molecules. There is much current interest in chiral systems for which standard transmission methods are not appropriate, as, for example, chiral thin films, strongly absorbing chiral materials, inhomogeneous chiral media, and chiral material with surface roughness.[55]

Flow birefringence occurs when a fluid becomes optically anisotropic in flows with a velocity gradient, particularly significant in polymer solutions.[26] By directly measuring flow birefringence, polarimetry is a unique experimental tool in studying the static and dynamic properties of polymers.

15

The size distribution of spherical SiO$_2$ particles upon a silicon wafer has been obtained from Mueller matrix measurements[56] with important applications in semiconductor industry.

Imaging the Mueller matrix has been used for determining the polarization aberration matrices for strain birefringence of a plastic lens, the point spread matrix of a LCTV, and characterization of spatial light modulators, polarizing beamsplitters,[57] and optoelectronic devices.[58]

Investigation of phase and structural transformations for rapidly pulse-heated metallic materials, thin film characterization and monitoring, and determination of optical properties of pure liquid metals can be done by measuring the ellipsometric parameters.[59,60] The effect of surface roughness and observation angle on the degree of polarization of thermal radiation is also of interest for imaging purposes in $10 - 11\mu m$ band.[61]

Heterodyne polarimetry can be used for measuring the Faraday rotation for far-infrared laser radiation transmitted through tokamak plasma, to determine the poloidal field distribution and subsequently the current density profile that plays a crucial role in plasma equilibrium and stability.[62]

Short vs. long-path photons (ballistic vs. diffuse background) emerging from a scattering medium can be discriminated by means of polarization techniques.[63] Other techniques that demonstrated similar capabilities with the purpose of improving imaging quality and depth penetration in turbid media are time-of-flight spectrophotometry,[64] time-gated imaging employing delayed-coincidence,[65] optical heterodyne[66] and second–

16

harmonic-generation cross-correlation techniques.[67] These imaging systems are expensive and complex, and are limited by the response time of the detectors.

All these applications have in common the fact that the main goal is the determination of inhomogeneities of the complex refractive index which is polarization sensitive in the form of linear or circular birefringence or dichroism. Structural characteristics of scattering media are subsequently related to physical properties of interest in biomedical field, remote sensing, industry and research. Noninvasive, sensitive, and fast measurement methods are needed. In the following Chapters, various measurements techniques for polarimetric characterization of electromagnetic fields and of scattering systems are developed. These techniques are then used for analyzing inhomogeneous media in different scattering regimes and geometries, relevant for applications such as the ones enlisted above.

17

CHAPTER 2

MEASUREMENT TECHNIQUES

New techniques for polarimetric characterization of random electromagnetic beams and of the transfer of these beams through various systems will be discussed in this Chapter.

The degree of polarization rather than the full description of the state of polarization is of interest in multiple scattering and free space propagation where the statistical nature and not the deterministic component of light bears relevant information. A new interferometric technique based on the measurement of intensity fluctuations will be presented for determining polarimetric characteristics of light governed by Gaussian statistics. In order to investigate such situations one needs a light source with a controllable degree of polarization. A novel light source with controllable spectral, polarimetric and coherence properties across the beam will be demonstrated here using phase modulators in a Mach-Zehnder interferometer illuminated with broadband unpolarized light. In particular, the degree of polarization is controlled by adjusting the correlation between parallel components of polarization propagating through the two arms of the interferometer.

These interferometric techniques used for tuning and measuring the degree of polarization require a good understanding of how random electromagnetic beams are superposed. A closer examination of the interference of such beams will lead us to a second interferometric measurement technique that actually provides complete description of the state

of polarization. A generalization of the laws of Fresnel and Arago is first developed for the interference of electromagnetic beams with any state of coherence and polarization. As a direct application of this new generalized interference law, an imaging polarimeter is proposed based on a modified Sagnac interferometer.

The measurement of the state of polarization is needed for analyzing the polarization transfer through systems that alter it. The choice of the measurement technique depends on the specific requirements of the experiment such as wavelength, time scale of the process investigated, precision required, and the cost of the instrumentation. A relatively inexpensive apparatus with no moving parts is highly desirable. In the second part of this Chapter, after a review of the current measurement techniques, two methods for performing Mueller polarimetry based on intensity measurements will be presented. The first method is fast involving no moving optical components and allowing a compact design, while the second one provides a high dynamic range in measuring very low power optical signals typical for multiple scattering. Practical considerations like calibration and optimization of Mueller polarimeters, as well as decomposition and noise filtering of Mueller matrices will also be discussed.

2.1. Interferometric techniques for characterization of electromagnetic beams

Complete description of the state of polarization in each spatial point of a random electromagnetic field is given by the Stokes vector or the coherence matrix, as described in Chapter 1. The statistical properties are reflected by the degree of polarization in that point, while the deterministic component of the fluctuating field is described by the

19

pure part of the state of polarization. The degree of polarization is directly related to the correlation of the orthogonal components of the electric field. This correlation can be obtained interferometrically by analyzing the fluctuations of the total intensity, or by projecting the orthogonal components along the same direction. Intensity fluctuations are first analyzed here in an interferometric technique for measuring the degree of polarization. A light source with a controllable degree of polarization is also demonstrated using an interferometric technique. Interference phenomena are governed by the interference laws of Fresnel and Arago. A generalization of these laws is proposed here for any state of coherence and polarization, followed by a direct application, namely, an interferometric imaging polarimeter.

2.1.1. Interferometric measurement of the degree of polarization based on intensity fluctuations

The electric field components, and therefore, the total intensity of a partially polarized random electromagnetic field are generally fluctuating. Mandel and Wolf[34] give the following formula $\left\langle (\Delta I)^2 \right\rangle = (1 + P^2) \left\langle I \right\rangle^2 / 2$ for the variance of the intensity fluctuations for partially polarized light in a coordinate system in which $\langle I_x \rangle = \langle I_y \rangle$, where the angular brackets $\langle ... \rangle$ denote the ensemble average, P is the degree of polarization, and $\langle I \rangle$ is the average intensity. The formula is obtained assuming Gaussian statistics for the fluctuations of the electric field components E_x and E_y which are partially correlated; the degree of correlation is related to the degree of polarization P. The contrast of the intensity fluctuations, calculated as the ratio between the standard deviation $\sigma = \left\langle (\Delta I)^2 \right\rangle^{1/2}$ and

20

the average intensity $\langle I \rangle$, can be written as $C = [(1 + P^2)/2]^{1/2}$, which gives $C = 1/\sqrt{2}$ for unpolarized light and $C = 1$ for fully polarized light. This formula shows a simple relationship between the contrast C of the intensity fluctuations and the degree of polarization P of light. The degree of polarization, the intensity and its variance, are all coordinate system invariant. Experimentally, the degree of polarization can be determined by simply measuring the contrast using a regular intensity detector which is also coordinate system invariant. However, if additional information is required about the polarized component of the light, more measurements are necessary using optical components which are polarization sensitive (polarizers, waveplates), and therefore, a coordinate system has to be specified for the orientation of the optical components and of the state of polarization. The use of polarizers to select specific polarimetric components is sometimes disadvantageous since a significant amount of light is blocked by the polarizer. A method is presented here for doing polarimetric measurements without using a polarizer, where a simple Mach-Zehnder interferometer is used for simultaneous measurement of the degree of polarization and of the second component of the Stokes vector, based on only two measurements. In addition to obtaining polarimetric information from contrast measurement this technique permits increasing the signal-to-noise ratio up to 40% in certain circumstances. A similar experimental setup was previously[68] used for adjusting the degree of polarization and the spectrum of light based on tuning the correlations between parallel components of the electric field coming from the two arms of the interferometer.

The degree of polarization rather than the full description of the state of polarization is of interest in multiple scattering[69] and free space propagation[70–72] where the statistical nature and not the deterministic component of light bears relevant information.

The polarization matrix formulation, as described in Section 1.3 is used here to describe the new technique.

For a Mach-Zehnder interferometer, the total output field is represented by the ensemble $\{\mathbf{E}^{(T)}\} = \{E_x^{(1)} + E_x^{(2)}\}\widehat{\mathbf{x}} + \{E_y^{(1)} + E_y^{(2)}\}\widehat{\mathbf{y}}$, where $\widehat{\mathbf{x}}$ and $\widehat{\mathbf{y}}$ denote the unit vectors along the x and y directions, 1 and 2 representing the two arms of the interferometer, as shown in Fig. 2.1. Considering that the field components in the two arms differ only by a phase factor $\exp(i\varphi_j)$ $(j = x, y)$, the total field can be expressed as function of the initial field components as $\{\mathbf{E}^{(T)}\} = \{E_x\}f_x\widehat{\mathbf{x}} + \{E_y\}f_y\widehat{\mathbf{y}}$, where $f_j = \left[1 + \exp(i\varphi_j)\right]/2$. The total output average intensity is then $\langle I \rangle = |f_x|^2 \left\langle |E_x|^2 \right\rangle + |f_y|^2 \left\langle |E_y|^2 \right\rangle$.
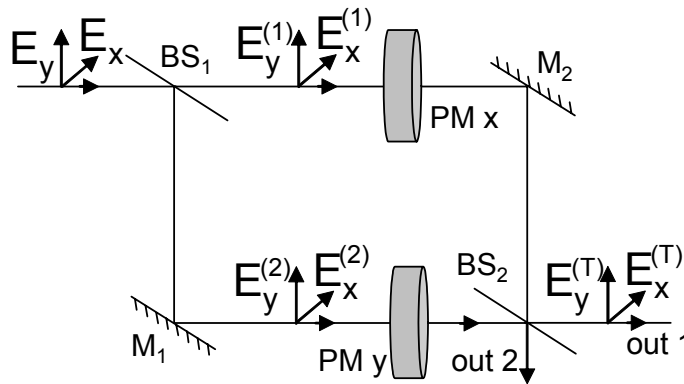
Figure 2.1. Mach-Zehnder interferometer: BS_1 and BS_2 - non-polarizing beamsplitters, M_1 and M_2 - mirrors, PM x and PM y - phase modulators controlling the phase along x and y directions, respectively.

In order to quantify the fluctuations of the output intensity one needs the intensity-intensity correlation

$$\langle I^2 \rangle = \left\langle \left(|f_x|^2 |E_x|^2 + |f_y|^2 |E_y|^2 \right)^2 \right\rangle \tag{23}$$

$$= |f_x|^4 \langle |E_x|^4 \rangle + |f_y|^4 \langle |E_y|^4 \rangle + 2 |f_x|^2 |f_y|^2 \langle |E_x|^2 |E_y|^2 \rangle,$$

which, for Gaussian statistics, can be written as

$$\langle I^2 \rangle = 2 |f_x|^4 J_{xx}^2 + 2 |f_y|^4 J_{yy}^2 + 2 |f_x|^2 |f_y|^2 \left(J_{xx} J_{yy} + |J_{xy}|^2 \right). \tag{24}$$

The variance of the intensity fluctuations is then given by

$$\langle (\Delta I)^2 \rangle = \langle I^2 \rangle - \langle I \rangle^2 \tag{25}$$

$$= |f_x|^4 J_{xx}^2 + |f_y|^4 J_{yy}^2 + 2 |f_x|^2 |f_y|^2 |J_{xy}|^2,$$

and therefore, the contrast can be obtained as

$$C = \frac{\sigma}{\langle I \rangle} = \frac{\left(|f_x|^4 J_{xx}^2 + |f_y|^4 J_{yy}^2 + 2 |f_x|^2 |f_y|^2 |J_{xy}|^2 \right)^{1/2}}{|f_x|^2 J_{xx} + |f_y|^2 J_{yy}}. \tag{26}$$

We further note that the off-diagonal term of the coherence matrix, J_{xy} can be expressed as function of the degree of polarization P from the Eq. 11

$$|J_{xy}|^2 = J_{yy}^2 \frac{P^2(r+1)^2 - (r-1)^2}{4}, \tag{27}$$

where $r = J_{xx}/J_{yy} = I_x/I_y$ is the ratio of intensities along the two orthogonal polarizations, x and y. Using this expression in formula 26 one can obtain the contrast of the output light fluctuations as function of the degree of polarization of the input light and the input intensity ratio r

$$C(f_x, f_y, r, P) = \frac{\left[|f_x|^4 r^2 + |f_y|^4 + |f_x|^2 |f_y|^2 \frac{P^2(r+1)^2 - (r-1)^2}{2} \right]^{1/2}}{|f_x|^2 r + |f_y|^2} \tag{28}$$

23

where $|f_j|$ varies between 0 and 1; $|f_j| = 1$ means no phase introduced, and $|f_j| = 0$ corresponds to π phase difference between the j components of the electric field through the two arms of the interferometer.

Since the intensity ratio r is not independent of the degree of polarization P, we need a more meaningful representation of the contrast as function of the state of polarization of the input light. The usual decomposition of the Stokes vector S into the fully polarized and fully unpolarized components[73] is used here

$$
S = \begin{bmatrix} I \\ Q \\ U \\ V \end{bmatrix} = \begin{bmatrix} I_x + I_y \\ I_x - I_y \\ U \\ V \end{bmatrix} = IP \begin{bmatrix} 1 \\ q \\ u \\ v \end{bmatrix} + I(1-P) \begin{bmatrix} 1 \\ 0 \\ 0 \\ 0 \end{bmatrix}. \tag{29}
$$

The intensity ratio r is given by $r = I_x/I_y = (I+Q)/(I-Q) = (1+Pq)/(1-Pq)$, where q is the normalized second element of the Stokes vector that describes the pure polarized component of the input light as shown in formula 29. Using this representation of the intensity ratio r one obtains the contrast C as function of the degree of polarization P, the normalized Stokes element q, and the phase factors f_j

$$
C(f_x, f_y, q, P) = \frac{\left[|f_x|^4 (1+Pq)^2 + |f_y|^4 (1-Pq)^2 + 2|f_x|^2 |f_y|^2 P^2(1-q^2) \right]^{1/2}}{|f_x|^2 (1+Pq) + |f_y|^2 (1-Pq)}. \tag{30}
$$

After simple algebraic manipulations, formula 30 can be simplified to

$$
C(f_x, f_y, q, P) = \left[1 - \frac{B(1-P^2)}{(APq+1)^2} \right]^{1/2} \tag{31}
$$

where the parameters $A = (|f_x|^2 - |f_y|^2)/(|f_x|^2 + |f_y|^2)$ and $B = 2|f_x|^2 |f_y|^2 (|f_x|^2 + |f_y|^2)^{-2}$ can be adjusted experimentally by tuning the phase factors f_x and f_y. This

24

simple formula directly relates the contrast C of the output intensity fluctuations to the degree of polarization P and the normalized Stokes element q of the input light. Using CCD cameras as detectors one can determine P and q in every point of a beam. Several practical consequences of this relationship are analyzed in the following.

The relationship between the contrast C and the polarimetric characteristics P and q can be used both ways: one can determine P and q by measuring C, or one can modify the contrast of the intensity fluctuations by either changing the input state of polarization or by adjusting the phase factors f_x and f_y.

Until now, only one output of the Mach-Zehnder interferometer was considered. The second output is complementary to the first one, and there is an additional π phase shift between parallel components of the electric field to be overlapped as compared to the first output. The previous analysis is similar for the second output, the only required modification being the replacement of the phase factors $f_j = \left[1 + \exp(i\varphi_j)\right]/2$ by $1 - f_j = \left[1 - \exp(i\varphi_j)\right]/2$. The parameters A and B in the formula 31 can be explicitly written as function of the phases φ_j introduced along the two orthogonal directions of polarization

$$A_{1,2} = \frac{\pm \cos(\varphi_x) \mp \cos(\varphi_y)}{2 \pm \cos(\varphi_x) \pm \cos(\varphi_y)} \tag{32}$$

$$B_{1,2} = \frac{2\left[1 \pm \cos(\varphi_x)\right]\left[1 \pm \cos(\varphi_y)\right]}{\left[2 \pm \cos(\varphi_x) \pm \cos(\varphi_y)\right]^2}, \tag{33}$$

where 1 and the top symbol correspond to output 1, while 2 and the bottom symbol correspond to output 2.

One can simultaneously measure the contrast of the intensity fluctuations for the two

outputs of the Mach-Zehnder interferometer and solve the following equations

$$C_{1,2} = \left[1 - \frac{B_{1,2}(1 - P^2)}{(1 + A_{1,2}Pq)^2} \right]^{1/2} \tag{34}$$

for the degree of polarization P and the normalized Stokes element q of the input light to

finally obtain

$$P = \left[1 - \frac{1 - C_1^2}{B_1} \left(\frac{A_2 - A_1}{A_2 - MA_1} \right)^2 \right]^{1/2} \tag{35}$$

and

$$q = \frac{M - 1}{A_2 - MA_1} \left[1 - \frac{1 - C_1^2}{B_1} \left(\frac{A_2 - A_1}{A_2 - MA_1} \right)^2 \right]^{-1/2} \tag{36}$$

where

$$M = \left(\frac{B_2}{B_1} \frac{1 - C_1^2}{1 - C_2^2} \right)^{1/2}. \tag{37}$$

Since B_1 is always positive and the contrast C is always smaller than 1, the second term in

the formula 35 is also positive. Therefore, the measured value of the degree of polarization

will always be nonnegative and smaller than or equal to unity.

We would like to mention here that for no additional phases, $\varphi_j = 0$, and $q = 0$,

formula 31 reduces to the one given by Mandel and Wolf[34] in the particular case of

$\langle I_x \rangle = \langle I_y \rangle$ $(q = 0)$.

Note that in this measurement the entire energy of the input light is used since

measurements are made on both outputs of the interferometer. In contrast, most of

the standard polarimetric techniques that use polarizers waste a considerable amount of

energy. We should also point out that this technique requires only two measurements

for determining the degree of polarization. In Stokes polarimetry four measurements are

26

necessary to completely determine the Stokes vector and to calculate subsequently the degree of polarization.

Fig. 2.2 shows the contrast C of the intensity fluctuations for output 1 of the interferometer as function of the phase φ_x for different values of q as indicated on each plot. As seen in Fig. 2.2 the contrast strongly depends on both P and q while changing the phase φ_x between 0 and π. However, $C = 1$ for $\varphi_x = \pi$ independent of P and q of the input light, as expected, since the output light is fully polarized (destructive interference for the x components of the electric field). Note that q is related to the ellipsometric parameters azimuth (α) and ellipticity $(tan(\omega))$ through this relationship $q = \cos(2\omega)\cos(2\alpha)$.
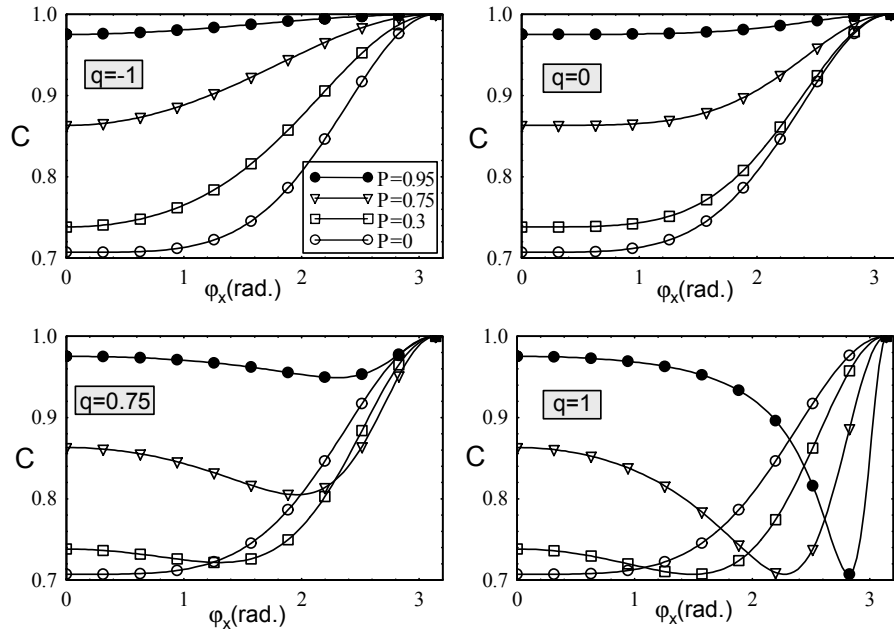
Figure 2.2. Contrast of intensity fluctuations for output 1 of the interferometer as function of the phase φ_x for different values of q as indicated on each plot, and different degrees of polarization as indicated in the legend.

By using both outputs it is not necessary to tune the phases along the two arms of the interferometer. A fixed waveplate placed in one arm of the interferometer and oriented with its axis parallel to the x-y coordinate system introduces different phases φ_x and φ_y along the x and y polarizations, sufficiently different such that $A_{1,2} \neq 0$. However, it is also possible to use only one output of the interferometer. Instead of $A_{1,2}$ and $B_{1,2}$ as given in the Eqns. 32-33 one can use A_1 and B_1 for different values of φ_x while keeping $\varphi_y = 0$ and still obtain both P and q. In this case, sequential measurements are required as opposed to simultaneous measurements when using both outputs.

Another important practical consequence of the relationship between the contrast C of the intensity fluctuations and the polarimetric characteristics P and q shown in the Eq. 31 is that the contrast can be modified by either changing the input state of polarization or by adjusting the phase factors f_x and f_y. Modifying the state of polarization might not always be possible, while adjusting the phase factors can be easily implemented using simple phase modulators. For simplicity, let us assume that there is no phase introduced along y direction and we use only one phase modulator along x axis ($f = |f_x|$) in one arm of the interferometer; $\varphi_y = 0$ gives $|f_y| = 1$.

The signal-to-noise ratio defined as the inverse of the contrast ($SNR = 1/C = \langle I \rangle / \sigma$) also depends on the input state of polarization and the phase factors. For Gaussian statistics of the fluctuations of the unpolarized input, SNR decreases from $\sqrt{2}$ to 1 while changing the phase φ_x from 0 to π. For a partially polarized input, however, SNR can be increased up to 40% while changing the phase φ_x. SNR or C, rather than the intensity

28

fluctuation is the relevant quantity since both the variance and the average intensity are modified by φ_x.

In Fig. 2.3, the signal-to-noise ratio SNR is show for output 1 of the interferometer as function of the phase φ_x for $q = 1$. As seen in Fig. 2.3, SNR can be increased by changing the phase φ_x between certain values for partially polarized light.
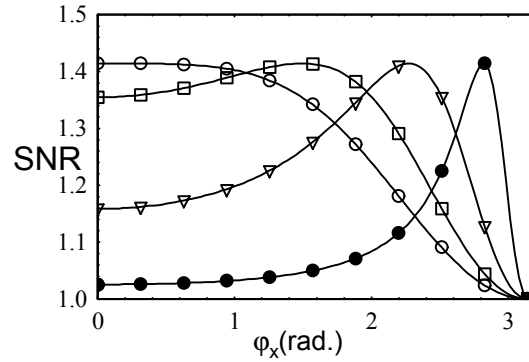
Figure 2.3. Signal-to-noise ratio for output 1 of the interferometer as function of the phase φ_x for $q = 1$, and different degrees of polarization as indicated in the legend of Fig. 2.2.

In conclusion, a technique for determining polarimetric characteristics of light (governed by Gaussian statistics) by measuring the contrast of the intensity fluctuations in an interferometric setup was presented. The method allows simultaneous measurement of the degree of polarization P and of the second normalized Stokes component q based on only two measurements. By measuring q one can determine the ellipticity, if one has apriori knowledge of the orientation α, or viceversa, knowing the ellipticity one can get the orientation. Another advantage is that, since both outputs of the interferometer are used for measurements, no input light is wasted, as opposed to the use of a polarizer. It

29

was also shown that the signal-to-noise ratio can be increased using phase modulation in certain conditions.

Finally, in this analysis only uniform phase applied across the beam was considered. Using spatial light modulators it is possible to control the contrast and therefore the SNR in every point across the beam, a capability which might be of interest for certain applications involving random electromagnetic beams.

2.1.2 Generation of complex electromagnetic beams

For complete characterization of a random electromagnetic field one has to specify its spectral, coherence and polarization properties. These field characteristics are related to each other and they generally change on propagation.[70,74,75] In certain applications, optical beams are superposed and it is, therefore, desirable to understand how these characteristic features combine. The recently developed unified theory of coherence and polarization of random electromagnetic beams[8] provides a theoretical framework for deriving the spectral density, the spectral degree of coherence and the spectral degree of polarization, namely the cross-spectral density matrix. As a direct application of this theory, it is shown here that, under certain conditions, the spectral and the polarimetric characteristics are related and can be controlled through field correlations.

Let us consider two optical fields which are stationary, at least in the wide sense. Within the frame of the second-order coherence theory in the space frequency domain (see Ref.[76]), their statistical properties may be characterized by ensembles (denoted by curly brackets) of realizations, $\{\mathbf{E}^{(A)}(\mathbf{r},\omega)\}$ and $\{\mathbf{E}^{(B)}(\mathbf{r},\omega)\}$, where $\mathbf{r}$ represents a position

30

vector of a typical field point and ω denotes the frequency. The frequency dependence will be omitted, to simplify the formulas, while the spatial dependence will be shown explicit only when it is necessary for the sake of clarity.

Let us consider two unpolarized beams which propagate along the z-axis. Since the light is unpolarized

$$\left\langle E_x^{(C)*} E_x^{(C)} \right\rangle = \left\langle E_y^{(C)*} E_y^{(C)} \right\rangle \tag{38}$$

$$\left\langle E_x^{(C)*} E_y^{(C)} \right\rangle = 0 \tag{39}$$

where the asterisk denotes the complex conjugate, the angular brackets denote the ensemble averages, $E_x^{(C)}$ and $E_y^{(C)}$ represent the components of the complex electric field along two mutually orthogonal directions, and the two individual beams are labeled as A or B. The first condition shows that the average intensity along the two orthogonal directions is the same, while the second implies that the two orthogonal components of the electric field are uncorrelated. If the two beams are superposed, the resulting total field is represented by the ensemble

$$\{\mathbf{E}^{(T)}\} = \{E_x^{(A)} + E_x^{(B)}\}\widehat{\mathbf{x}} + \{E_y^{(A)} + E_y^{(B)}\}\widehat{\mathbf{y}}, \tag{40}$$

where $\widehat{\mathbf{x}}$ and $\widehat{\mathbf{y}}$ denote the unit vectors along the x and y directions.

The second-order coherence properties of the total field are characterized by the cross-spectral density matrix[8]

$$\underline{W}^{(T)}(\mathbf{r}_1, \mathbf{r}_2) = \left\langle \mathbf{E}^{(T)*}(\mathbf{r}_1)\mathbf{E}^{(T)}(\mathbf{r}_2) \right\rangle = \tag{41}$$

$$= \left\langle (\mathbf{E}^{(A)}(\mathbf{r}_1) + \mathbf{E}^{(B)}(\mathbf{r}_1))^* (\mathbf{E}^{(A)}(\mathbf{r}_2) + \mathbf{E}^{(B)}(\mathbf{r}_2)) \right\rangle.$$

31

It follows that

$$\underline{W}^{(T)}(\mathbf{r}_1, \mathbf{r}_2) = \underline{W}^{(A)}(\mathbf{r}_1, \mathbf{r}_2) + \underline{W}^{(B)}(\mathbf{r}_1, \mathbf{r}_2) + \underline{W}^{(A,B)}(\mathbf{r}_1, \mathbf{r}_2) + \underline{W}^{(B,A)}(\mathbf{r}_1, \mathbf{r}_2) \qquad (42)$$

where $\underline{W}^{(A)}$ and $\underline{W}^{(B)}$ are the cross-spectral density matrices of each of the two beams to be superposed, and $\underline{W}^{(A,B)}$ and $\underline{W}^{(B,A)}$ are the mutual cross-spectral density matrices. This formula represents *the superposition law for the cross-spectral density matrices of electromagnetic beams.*

Two important quantities of practical interest are derived from the cross-spectral density matrix, as described in Section 1.4, namely the spectral density

$$S^{(T)}(\mathbf{r}) = Tr[\underline{W}^{(T)}(\mathbf{r}, \mathbf{r})] \qquad (43)$$

and the spectral degree of polarization

$$P^{(T)}(\mathbf{r}) = \left(1 - \frac{4 Det[\underline{W}^{(T)}(\mathbf{r}, \mathbf{r})]}{\{Tr[\underline{W}^{(T)}(\mathbf{r}, \mathbf{r})]\}^2} \right)^{\frac{1}{2}} \qquad (44)$$

of the total field at a point $\mathbf{r}$.

Taking $\mathbf{r}_1 = \mathbf{r}_2$ in Eq. 42 and making use of Eq. 43 and of the fact that the mutual spectral densities $S^{(A,B)}$ and $S^{(B,A)}$ are complex conjugate of each other, it follows that

$$S^{(T)} = S^{(A)} + S^{(B)} + 2 \operatorname{Re} S^{(A,B)} \qquad (45)$$

where Re denotes the real part. This formula is *the spectral interference law for the superposition of random electromagnetic fields.*

To analyze the spectral interference represented by the last term on the right-hand side of Eq. 45, let us denote the cross-correlations of mutually parallel electric field components

32

in the two beams as $S_x^{(A,B)} = \left\langle E_x^{(A)*} E_x^{(B)} \right\rangle$ and $S_y^{(A,B)} = \left\langle E_y^{(A)*} E_y^{(B)} \right\rangle$. Formula 45 can then be expressed in the form

$$S^{(T)} = S^{(A)} + S^{(B)} + 2\operatorname{Re} S_x^{(A,B)} + 2\operatorname{Re} S_y^{(A,B)}, \tag{46}$$

while the spectral degree of polarization becomes

$$P^{(T)} = \frac{2\left|\operatorname{Re} S_x^{(A,B)} - \operatorname{Re} S_y^{(A,B)}\right|}{S^{(A)} + S^{(B)} + 2\operatorname{Re} S_x^{(A,B)} + 2\operatorname{Re} S_y^{(A,B)}}, \tag{47}$$

and the state of polarization is given by the polarization matrix (Section 1.3)

$$
\begin{aligned}
J &= \begin{bmatrix} \frac{(S^{(A)}+S^{(B)})}{2} + 2\operatorname{Re} S_x^{(A,B)} & 0 \\[2mm] 0 & \frac{(S^{(A)}+S^{(B)})}{2} + 2\operatorname{Re} S_y^{(A,B)} \end{bmatrix} \\[3mm]
&= 2\left(\operatorname{Re} S_x^{(A,B)} - \operatorname{Re} S_y^{(A,B)}\right) \begin{bmatrix} 1 & 0 \\ 0 & 0 \end{bmatrix} + \left[\frac{(S^{(A)} + S^{(B)})}{2} + 2\operatorname{Re} S_y^{(A,B)}\right] \begin{bmatrix} 1 & 0 \\ 0 & 1 \end{bmatrix}
\end{aligned} \tag{48}
$$

which represents incoherent superposition of linearly polarized and unpolarized light. The polarized component of such superposition is always linear since there is no deterministic phase introduced between the x and y components of the electric field.

If the real parts of the two field correlations are equal, i.e. if $\operatorname{Re} S_x^{(A,B)} = \operatorname{Re} S_y^{(A,B)}$, then $P^{(T)} = 0$ and the output is unpolarized. However, if the two correlations differ, then the output is partially polarized. By controlling the value of the field correlations one can change both the spectral density and the spectral degree of polarization on superposition. This can be easily implemented using phase modulators in interferometric setups, for example by using a Mach-Zehnder interferometer, as shown in Fig. 2.1. Since the two beams derive from a common source, $S_x^{(A,B)} \neq 0$ and $S_y^{(A,B)} \neq 0$, in general.

Consider now the situation where each arm of the interferometer contains a phase modulator that controls only the phase along x axis for beam A and along the y axis for

33

the beam B. If these two modulators introduce the phases $\psi_x(\omega)$ and $\psi_y(\omega)$, respectively, then the field correlations along x and y directions become

$$S_j^{(A,B)} = \left\langle E_j^{(A)*} E_j^{(B)} \exp(i\psi_j(\omega)) \right\rangle. \qquad (49)$$

The two individual beams remain unpolarized and their spectrum is not affected by the additional phases.

The properties of the phase $\psi_j(\omega)$ will determine the properties of the field correlations $S_j^{(A,B)}$. The output spectrum (the superposition of A and B) given by Eq. 46 and the total spectral degree of polarization given by Eq. 47 can be controlled by adjusting the value of the two field correlations $S_j^{(A,B)}$.

Assuming that the first beamsplitter divides the beam into identical replicas, then $E_x^{(A)} = E_x^{(B)} = E_x/\sqrt{2}$, $E_y^{(A)} = E_y^{(B)} = E_y/\sqrt{2}$, and $S^{(A)} = S^{(B)} = \frac{1}{2}S_0$. Since the second beamsplitter has a 50% intensity transmission (reflection), there is an additional factor $\sqrt{2}$ in the denominator of the fields to be overlapped in Eq. 40. This gives an additional factor $\frac{1}{2}$ for all the correlations encountered in the previous calculations.

If there is no phase change introduced by the phase modulators ($\psi_j(\omega) = 0$), then there is complete spectral interference ($S^{(T)} = S_0$ for one output), and the degree of polarization is zero. If both phases are equal to π the spectrum and the degree of polarization vanish. The two outputs of the interferometer are complementary, maximum for one output corresponds to minimum for the other output. The calculations for the second output require subtraction instead of addition of fields in Eq. 40 because of the additional π phase shift for one of the beams.

34

If $\psi_j(\omega)$ are random functions of zero mean, than $S_j^{(A,B)}$ are zero, and $S^{(T)} = \frac{1}{2}S_0$, $P^{(T)} = 0$. There is no interference of the two fields and the total spectrum is the sum of the two individual spectra.

If the two phases are $\psi_x(\omega) = 0$, and $\psi_y(\omega) = \pi$, then the output spectral density is half of the input one, while the degree of polarization reaches its maximum, $P^{(T)} = 1$. This can be easily explained considering that the x components of the individual fields are identical, and therefore, interfere constructively, while the y components are π phase shifted interfering destructively. The situation is reversed for the second output of the interferometer which will be linearly polarized along y direction. It is worth noting that no power is lost while the two outputs are fully polarized and orthogonal to each other.

To illustrate these results experimentally, a Mach-Zehnder interferometer is used, as shown in Fig. 2.1, composed of two mirrors (M_1 and M_2) and two 50/50 broadband nonpolarizing beamsplitters (BS_1 and BS_2). The unpolarized light source was a collimated broadband LED with an initial spectral density as shown by the doted line in Fig. 2.4. The phase modulators were wide aperture liquid crystal modulators aligned with their slow axis along x and y direction, respectively. The interferometer was perfectly aligned to obtain the zero-order white-light fringe, and the central part of the zero-order fringe was coupled into a multimode optical fiber and was analyzed with an optical spectrum analyzer. A broadband polarizer was used for measuring the x and y components of the spectral densities. In the present experiment the spectral resolution was 2nm; the relative errors in measuring the spectral density and the degree of polarization were 0.81% and 3%, respectively.

The phase ψ introduced by a liquid crystal modulator depends on both the wavelength and the applied voltage

$$\psi(V, \lambda) = \frac{2\pi}{\lambda} d G(V) \frac{\lambda^2 \lambda^{*2}}{\lambda^2 - \lambda^{*2}}, \tag{50}$$

where d is the thickness of the liquid crystal slab, λ^* is the mean electronic transition wavelength, and $G(V)$ is a voltage dependent proportionality constant.[77] Fig. 2.4 presents both the measured total spectral density (dots) and the theoretical spectrum (continuous line) calculated with the formula

$$S^{(T)} = S^{(A)} + S^{(B)} + 2 \left(S_x^{(A)} S_x^{(B)} \right)^{\frac{1}{2}} \cos(\psi_x) + 2 \left(S_y^{(A)} S_y^{(B)} \right)^{\frac{1}{2}} \cos(\psi_y), \tag{51}$$

where $S_j^{(A)}$ and $S_j^{(B)}$ are the spectral densities of the individual beams measured using a polarizer along the j direction ($j = x, y$). The expression 51 was obtained from Eq. 46 by explicitly writing the real part of the field correlations.
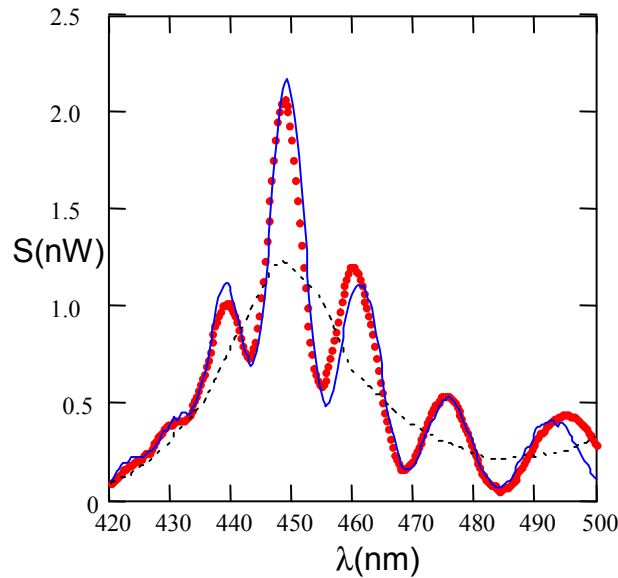
Figure 2.4. Measured spectral density (dots) together with the prediction of Eq. 51 for our experimental situation (continuous line). Also shown by dotted line is the spectral density of the light source.

As can be seen in Fig. 2.4, calculations based on formula 51 agree well with the experimental data over a broad range of wavelengths.

Since there is no deterministic phase introduced between the x and y electric field components of the superposition, the degree of polarization defined in the Eq. 44 can simply be determined using a polarizer along orthogonal directions that give maximum and minimum intensity (spectrum density), respectively, (x and y directions in this case).

The corresponding values of the spectral degree of polarization are shown in Fig. 2.5. The dots represent the measured spectral degree of polarization of the superposition, obtained from

$$P_{\exp}^{(T)} = \frac{\left| S_x^{(T)} - S_y^{(T)} \right|}{S_x^{(T)} + S_y^{(T)}}, \tag{52}$$

where $S_j^{(T)}$ are the spectral densities of the superposition measured using a polarizer along j direction $(j = x, y)$.
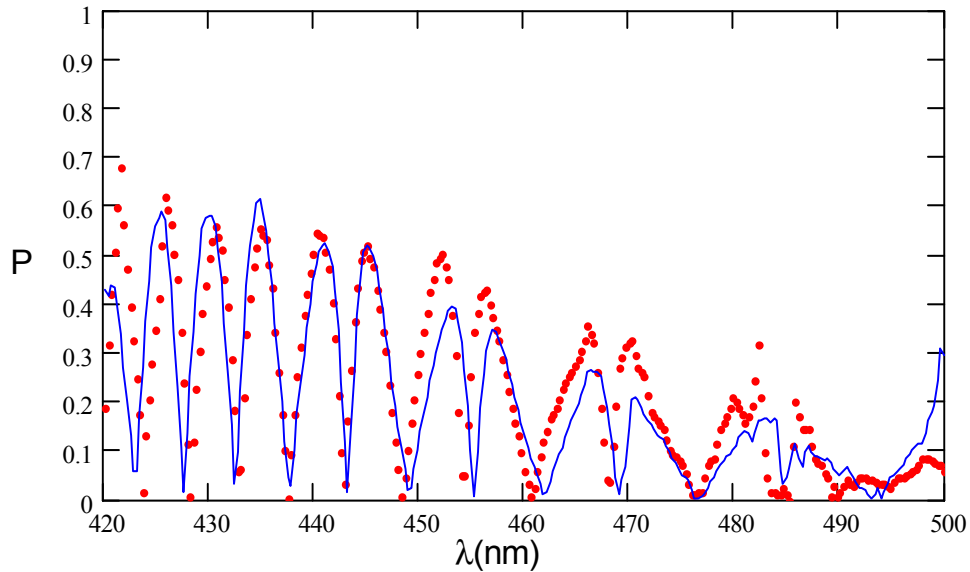
Figure 2.5. Measured spectral degree of polarization (dots) together with the prediction of Eq. 53 for our experimental arrangement (continuous line).

37

The continuous line in Fig. 2.5 represents the theoretical spectral degree of polarization calculated with the formula

$$P^{(T)} = \frac{2 \left| \left(S_x^{(A)} S_x^{(B)} \right)^{\frac{1}{2}} \cos(\psi_x) - \left(S_y^{(A)} S_y^{(B)} \right)^{\frac{1}{2}} \cos(\psi_y) \right|}{S^{(T)}}, \tag{53}$$

which is obtained from the Eq. 47. As can be seen, the output is partially polarized, demonstrating the possibility of generating light with adjustable spectral degree of polarization while only controlling the phase along x direction in one arm of the interferometer.

Since the input light is unpolarized and there is no correlation between the x and y components of the electric field vector, one can analyze the interferometer as being made of two independent interferometers (x and y), overlapped, illuminated with quasi-monochromatic linearly polarized light along x and y direction, respectively. The same output of both interferometers will have maximum intensity when they are perfectly aligned. Adjusting the phase along one arm in only one interferometer (x) will decrease the output intensity toward minimum (by increasing it in the second output of the x interferometer), while the y interferometer remains unchanged. The Eq. 38 is not satisfied anymore and the total output of the overlapped interferometers is linearly polarized along y direction.

It is also mention here that the spectral degree of coherence of the total electric field, as described in Section 1.4, is

$$\mu_{12}^{(T)} = \frac{\left\langle E_{x1}^{(A)*} E_{x2}^{(A)} \right\rangle + \left\langle E_{x1}^{(B)*} E_{x2}^{(B)} \right\rangle + \left\langle E_{y1}^{(A)*} E_{y2}^{(A)} \right\rangle + \left\langle E_{y1}^{(B)*} E_{y2}^{(B)} \right\rangle +}{\sqrt{S_1^{(T)}} \sqrt{S_2^{(T)}}} \tag{54}$$
$$+ \frac{\left\langle E_{x1}^{(A)*} E_{x2}^{(B)} \right\rangle + \left\langle E_{x1}^{(B)*} E_{x2}^{(A)} \right\rangle + \left\langle E_{y1}^{(A)*} E_{y2}^{(B)} \right\rangle + \left\langle E_{y1}^{(B)*} E_{y2}^{(A)} \right\rangle}{\sqrt{S_1^{(T)}} \sqrt{S_2^{(T)}}}.$$

38

One can see in the first line of the Eq. 54 that $\mu_{12}^{(T)}$ depends on the coherence properties of the individual fields to be overlapped, the correlations between parallel components of the same fields, A or B, in pairs of points. The second line of the Eq. 54 shows that $\mu_{12}^{(T)}$ also depends on the correlations that might exist between parallel components of the two fields, also in pairs of points. In the experiment described above, the second set of correlations can be controlled by adjusting the phases in the two arms of the interferometer, demonstrating the potential of controlling the coherence properties of the total beam using spatial phase modulators.

In conclusion, it was shown that under certain interferometric conditions the spectral density and the spectral degree of polarization are related through field correlations. The results suggested the possibility of producing light with controllable spectral density and controllable degree of polarization. Using phase modulators in a Mach-Zehnder interferometer illuminated with broadband unpolarized light, it was demonstrated that partially polarized light can be generated by controlling field correlations. This novel light source permits analyzing subtle details of the propagation of partially polarized beams through turbid media.

2.1.3. Generalization of the interference laws of Fresnel and Arago

The interference laws of Fresnel and Arago relate the ability of two waves to interfere with their polarimetric characteristics. They were derived almost 200 years ago based on experimental observations using a double-pinhole Young's interferometer.[1] Their modern formulation was presented by Hanau,[78] Collett[79] and Brosseau.[11] A theoretical derivation

39

of the four laws was given by Collett[79] without, however, any reference to the coherence properties of the field at the pinholes plane, and only for linearly polarized or unpolarized light source. A generalization of the interference laws for any state of coherence and polarization of the field is proposed in this Section. Just for clarity, the original four laws are stated here:

1) Two waves linearly polarized with perpendicular polarization, cannot interfere.

2) Two waves linearly polarized in the same plane, can interfere.

3) Two waves, linearly polarized with perpendicular polarizations, if derived from perpendicular components of unpolarized light and subsequently brought into the same plane, cannot interfere.

4) Two waves, linearly polarized with perpendicular polarizations, if derived from the same linearly polarized light and subsequently brought into the same plane, can interfere.

Let us consider a double-pinhole Young's interferometer with the pinholes in plane $\mathfrak{A}$, and an observation plane $\mathfrak{B}$ placed in the focal plane of a lens with the focal length f, as illustrated in Fig. 2.6. Immediately following the pinholes there are two polarizers P_1 and P_2 oriented at θ_1 and θ_2, respectively. A rotator R is placed after the polarizer P_1.

The cross-spectral density matrix[8] formalism is used here, as presented in Section 1.4, to characterize the second-order coherence properties of a random electromagnetic field.

40
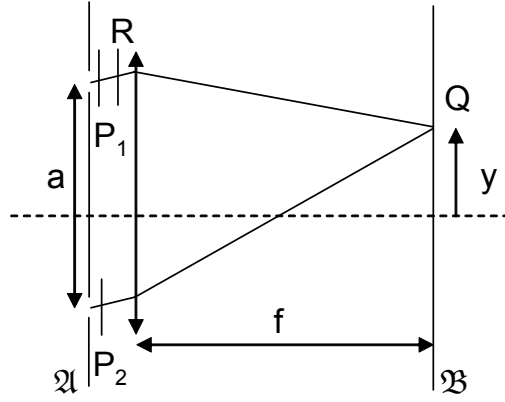
Figure 2.6. Typical Young's interference setup. P_1 and P_2 - polarizers, R - rotator.

The electric field at the observation point Q when only the pinhole 1 is open is

$$\mathbf{E}_1\left(\mathbf{r}_1, \theta_1, \alpha, \varphi_1, \omega\right) = R\left(\alpha\right) P\left(\theta_1\right) \exp\left(i\varphi_1\right) \begin{bmatrix} E_x\left(\mathbf{r}_1, \omega\right) \\ \\ E_y\left(\mathbf{r}_1, \omega\right) \end{bmatrix} = \tag{55}$$

$$= \left[E_x\left(\mathbf{r}_1, \omega\right) \cos\left(\theta_1\right) + E_y\left(\mathbf{r}_1, \omega\right) \sin\left(\theta_1\right)\right] \exp\left(i\varphi_1\right) \begin{bmatrix} \cos\left(\theta_1 - \alpha\right) \\ \\ \sin\left(\theta_1 - \alpha\right) \end{bmatrix},$$

while when only the pinhole 2 is open is given by

$$\mathbf{E}_2\left(\mathbf{r}_2, \theta_2, \varphi_2, \omega\right) = P\left(\theta_2\right) \exp\left(i\varphi_2\right) \begin{bmatrix} E_x\left(\mathbf{r}_2\right) \\ \\ E_y\left(\mathbf{r}_2\right) \end{bmatrix} = \tag{56}$$

$$= \left[E_x\left(\mathbf{r}_2, \omega\right) \cos\left(\theta_2\right) + E_y\left(\mathbf{r}_2, \omega\right) \sin\left(\theta_2\right)\right] \exp\left(i\varphi_2\right) \begin{bmatrix} \cos\left(\theta_2\right) \\ \\ \sin\left(\theta_2\right) \end{bmatrix},$$

where φ_1 and φ_2 are the geometric phases accumulated by light travelling from the two pinholes to the observation point Q, and $P\left(\theta\right)$ and $R\left(\alpha\right)$ are the Jones matrices for a polarized and a rotator,[80] respectively.

41

The total spectral density at the observation point Q, calculated as

$$S(Q) = \langle (\mathbf{E}_1^* + \mathbf{E}_2^*) \cdot (\mathbf{E}_1 + \mathbf{E}_2) \rangle, \tag{57}$$

is then given by

$$S(Q) = S_c(Q) + 2\cos(\theta_1 - \alpha - \theta_2) S^{12}(Q) \tag{58}$$

where

$$
\begin{aligned}
S_c(Q) = & \; S_x(\mathbf{r}_1)\cos^2(\theta_1) + S_y(\mathbf{r}_1)\sin^2(\theta_1) + \\
& + 2\sin(\theta_1)\cos(\theta_1)\operatorname{Re} W_{xy}(\mathbf{r}_1, \mathbf{r}_1) + \\
& + S_x(\mathbf{r}_2)\cos^2(\theta_2) + S_y(\mathbf{r}_2)\sin^2(\theta_2) + \\
& + 2\sin(\theta_2)\cos(\theta_2)\operatorname{Re} W_{xy}(\mathbf{r}_2, \mathbf{r}_2)
\end{aligned}
\tag{59}
$$

is the constant contribution to the spectral density pattern in the plane $\mathfrak{B}$ and only contains the incoherent addition of the spectral densities at Q corresponding to the pinholes being open one at a time ($S_m(\mathbf{r}_j)$ [$m = x, y$, $j = 1, 2$] is the spectral density at $\mathbf{r}_j$ along direction m of polarization). The term $W_{xy}(\mathbf{r}_j, \mathbf{r}_j)$ is the off diagonal term of the coherence matrix[7] and is related to the state of polarization of the field at $\mathbf{r}_j$.

The second term in the Eq. 58 represents a superposition of four fringe patterns

$$
\begin{aligned}
S^{12}(Q) = & \; \cos(\theta_1)\cos(\theta_2)\operatorname{Re}\left[W_{xx}(\mathbf{r}_1, \mathbf{r}_2)\exp(i\Delta)\right] + \\
& + \sin(\theta_1)\sin(\theta_2)\operatorname{Re}\left[W_{yy}(\mathbf{r}_1, \mathbf{r}_2)\exp(i\Delta)\right] + \\
& + \cos(\theta_1)\sin(\theta_2)\operatorname{Re}\left[W_{xy}(\mathbf{r}_1, \mathbf{r}_2)\exp(i\Delta)\right] + \\
& + \sin(\theta_1)\cos(\theta_2)\operatorname{Re}\left[W_{yx}(\mathbf{r}_1, \mathbf{r}_2)\exp(i\Delta)\right],
\end{aligned}
\tag{60}
$$

42

where Re stands for real part, $\Delta = \varphi_2 - \varphi_1 = 2\pi(R_2 - R_1)/\lambda$, and θ_1, θ_2 and α are the orientations of the two polarizers and of the rotator, respectively. The first two fringe patterns correspond to the correlations of parallel electric field components (x-x and y-y) as generally known in the classical coherence theory. The last two fringe patterns are the result of correlations of orthogonal electric field components (x-y and y-x) that were made parallel by the rotator.

The two polarizers select the field components to be overlapped and the rotator modifies one of them to set the relative orientation of the electric field components finally overlapped at the observation plane. Formula 58 is a *generalization of the interference laws of Fresnel and Arago for an electromagnetic field of any state of coherence and any state of polarization* in the plane $\mathfrak{A}$. It contains all four interference laws for particular choices of the orientations of the polarizers and rotator, as we will see later.

The mutual complex degree of coherence is introduced here, similar to the classical theory of scalar coherence

$$\mu_{mn}^{12} = \frac{W_{mn}\left(\mathbf{r}_1, \mathbf{r}_2\right)}{\sqrt{S_m\left(\mathbf{r}_1\right)}\sqrt{S_n\left(\mathbf{r}_2\right)}} = \left|\mu_{mn}^{12}\right| \exp\left(i\beta_{mn}^{12}\right), \tag{61}$$

where $m, n = x, y$. In particular, for $m = n$

$$\mu_{xx}^{12} = \frac{W_{xx}\left(\mathbf{r}_1, \mathbf{r}_2\right)}{\sqrt{S_x\left(\mathbf{r}_1\right)}\sqrt{S_x\left(\mathbf{r}_2\right)}}, \ \mu_{yy}^{12} = \frac{W_{yy}\left(\mathbf{r}_1, \mathbf{r}_2\right)}{\sqrt{S_y\left(\mathbf{r}_1\right)}\sqrt{S_y\left(\mathbf{r}_2\right)}} \tag{62}$$

are identical to the degree of coherence in scalar theory, except that in vector theory it might be different for different directions of polarization. These particular expressions of the mutual complex degree of coherence are related to the overall complex degree of coherence[8] derived from the cross-spectral density matrix (formula 21) through the

following relation

$$\mu^{12}\sqrt{[S_x(\mathbf{r}_1) + S_y(\mathbf{r}_1)][S_x(\mathbf{r}_2) + S_y(\mathbf{r}_2)]} = \mu_{xx}^{12}\sqrt{S_x(\mathbf{r}_1) S_x(\mathbf{r}_2)} + \mu_{yy}^{12}\sqrt{S_y(\mathbf{r}_1) S_y(\mathbf{r}_2)}.$$

(63)

For $m \neq n$ and $\mathbf{r}_1 \neq \mathbf{r}_2$, μ_{mn}^{12} is a *generalization of the complex degree of polarization coherence*[81] μ_{xy}^{jj}, introduced for $\mathbf{r}_1 = \mathbf{r}_2$ as a measure of the correlation between the orthogonal components of the electric field in one point. $\left|\mu_{xy}^{jj}\right|$ is directly related to the degree of polarization P_j of light at $\mathbf{r}_j$ ($\left|\mu_{xy}^{jj}\right| \leq P_j$) and $\beta_{xy}^{jj} = \delta_j$ is the retardance, the relative phase difference of the orthogonal vibrations at $\mathbf{r}_j$. μ_{xy}^{12} quantifies the correlation between orthogonal components of the electric field at a pair of points and it can be easily shown that its modulus is smaller than unity.

Using the definition 61 in the Eqns. 59 and 60 one immediately obtains

$$S_c(Q) = S_x(\mathbf{r}_1)\cos^2(\theta_1) + S_y(\mathbf{r}_1)\sin^2(\theta_1) + \tag{64}$$
$$+ 2\sin(\theta_1)\cos(\theta_1)\left|\mu_{xy}^{11}\right|\sqrt{S_x(\mathbf{r}_1) S_y(\mathbf{r}_1)}\cos(\delta_1) +$$
$$+ S_x(\mathbf{r}_2)\cos^2(\theta_2) + S_y(\mathbf{r}_2)\sin^2(\theta_2) +$$
$$+ 2\sin(\theta_2)\cos(\theta_2)\left|\mu_{xy}^{22}\right|\sqrt{S_x(\mathbf{r}_2) S_y(\mathbf{r}_2)}\cos(\delta_2)$$

$$S^{12}(Q) = \cos(\theta_1)\cos(\theta_2)\left|\mu_{xx}^{12}\right|\sqrt{S_x(\mathbf{r}_1) S_x(\mathbf{r}_2)}\cos\left(\Delta + \beta_{xx}^{12}\right) + \tag{65}$$
$$+ \sin(\theta_1)\sin(\theta_2)\left|\mu_{yy}^{12}\right|\sqrt{S_y(\mathbf{r}_1) S_y(\mathbf{r}_2)}\cos\left(\Delta + \beta_{yy}^{12}\right) +$$
$$+ \cos(\theta_1)\sin(\theta_2)\left|\mu_{xy}^{12}\right|\sqrt{S_x(\mathbf{r}_1) S_y(\mathbf{r}_2)}\cos\left(\Delta + \beta_{xy}^{12}\right) +$$
$$+ \sin(\theta_1)\cos(\theta_2)\left|\mu_{yx}^{12}\right|\sqrt{S_y(\mathbf{r}_1) S_x(\mathbf{r}_2)}\cos\left(\Delta + \beta_{yx}^{12}\right).$$

One can see from the formula 64 that for any orientation of the polarizers, other than $0°$ and $90°$, $S_c(Q)$ depends on the state of polarization ($S_x(\mathbf{r}_j)$, $S_y(\mathbf{r}_j)$, and δ_j), as well as

44

on the degree of polarization (through $\left|\mu_{xy}^{jj}\right|$) at each pinholes. Also, the interference term $S^{12}(Q)$ is independent on the degree of polarization at the two pinholes. It only depends on the coherence properties along x and y and on the correlation between orthogonal components of the electric field at a pair of points defined by μ_{xy}^{12}. It is worth noting that the four interference patterns described by the formula 65 have the same fringe spacing but have different shifts given by β_{mn}^{12}. The four interference patterns can be visualized independently by suitably choosing the orientations of the two polarizers and of the rotator as we will see in the particular case of the original interference laws.

2.1.3.1. Example 1

Orthogonal components of the electric field are selected if $\theta_1 - \theta_2 = \pi/2$; for example, $\theta_1 = \alpha = 0$, and $\theta_2 = \pi/2$. The rotator R has no role here. In this case, the total spectral density is $S_x(Q) = S_x(\mathbf{r}_1) + S_y(\mathbf{r}_2)$. There is no interference between orthogonal components of the electric field.

2.1.3.2. Example 2

By fulfilling the condition $\theta_1 - \alpha = \theta_2$ one selects parallel components of the electric field that interfere in the observation plane $\mathfrak{B}$. For clarity, two particular cases are illustrated here from the Eq. 58 by the same formal equation:

$$S_m(Q) = S_m(\mathbf{r}_1) + S_m(\mathbf{r}_2) + 2\left|\mu_{mm}^{12}\right| \sqrt{S_m(\mathbf{r}_1) S_m(\mathbf{r}_2)} \cos\left(\Delta + \beta_{mm}^{12}\right) \qquad (66)$$

a) $m = x$ for $\theta_1 = \theta_2 = \alpha = 0$, and

b) $m = y$ for $\theta_1 = \theta_2 = \pi/2$, $\alpha = 0$.

45

Parallel components of the electric field can interfere depending on their correlation, which might be different for different directions of the polarization, and independent on the degree of polarization at the two pinholes.

2.1.3.3. Example 3

If the orthogonal components of the electric field selected by $\theta_1 - \theta_2 = \pi/2$ are subsequently made parallel using the rotator R, choosing for example $\theta_1 = 0$, and $\alpha = \theta_2 = \pi/2$, then the total spectral density is

$$S\left(Q\right) = S_x(\mathbf{r}_1) + S_y(\mathbf{r}_2) - 2\left|\mu_{xy}^{12}\right|\sqrt{S_x\left(\mathbf{r}_1\right)S_y\left(\mathbf{r}_2\right)}\cos\left(\Delta + \beta_{xy}^{12}\right). \tag{67}$$

Interference fringes are observed if there is statistical similarity between the orthogonal components of the electric field at the two pinholes. In particular, if the field at the pinholes plane is derived from a fully polarized light source, there is complete correlation between the orthogonal components of the electric field. However, if the light source is unpolarized, there is no correlation between such components and no interference is observed. A partially polarized light source generates a certain degree of correlation between orthogonal components of the electric field in the plane $\mathfrak{A}$, and, therefore, a fringe pattern is obtain in the observation plane $\mathfrak{B}$ with a visibility directly related to the degree of polarization of light at the source.

In conclusion, following the previous analysis based on the formula 58 we can state three generalized laws of interference:

1) Orthogonal components of a random electromagnetic field cannot interfere irrespective of the coherence and polarization properties of the field.

46

2) Parallel components of a random electromagnetic field can interfere depending on the coherence and polarization properties of the field.

3) Orthogonal components of a random electromagnetic field subsequently brought into the same plane can interfere depending on the mutual complex degree of coherence of the field.

2.1.4. Imaging polarimeter based on a modified Sagnac interferometer

Polarimetric imaging systems are widely used in biomedical[36–38] and remote sensing[28,29] applications for improving the imaging depth in turbid media or for mapping the distribution of complex refractive index.[39] Various techniques such as continuously rotating two retarders,[82,83] classical Mueller polarimetry,[84,85] four liquid crystal variable retarders,[86] or four cameras,[87,88] are used for polarimetric characterization of scattering media. These methods generally require acquisition of a large number of images. There are, however, applications such as the ones where scattering is dominant, where complete polarimetric characterization is not required because the relevant information is obtained from the degree of polarization of light. We introduce here a method in which the degree of polarization can be recovered from only one image.

Single scattering on a cloud of particles in both forward and backward directions, has the characteristic that one cannot define a scattering plane. Using this assumption of rotational symmetry and other symmetry considerations, van de Hulst[9] concludes that the Mueller matrix for forward and backward scattering is diagonal with $m_{22} = m_{33} \neq m_{44}$. This happens in certain cases of interest, such as a collection of randomly oriented iden-

47

tical particles each of which has a plane of symmetry, or particles and mirror particles in equal number. Similar considerations apply to multiple scattering in forward and backward direction where the Mueller matrix is also diagonal with $m_{22} = m_{33} \neq m_{44}$, and the diagonal elements decay exponentially with the optical density. In these cases, the ratio m_{33}/m_{44} can be related to the size of the spherical scatterers[69, 89] and the orientation of the state of polarization of the initial beam remains unchanged. What changes is only the ellipticity and the degree of polarization which vary with the particle size distribution in single scattering regime or with the optical density in multiple scattering. In applications such as active illumination sensing or imaging through turbid media, one can control the orientation of the incident state of polarization such that, in a given coordinate system, the intensities along the orthogonal directions x and y are equal. In this situation, the measurement technique that is proposed here has a significant advantage over the standard Stokes polarimetry, namely, it requires only one frame to obtain both the degree of polarization and the retardance. In Stokes polarimetry, one needs at least three images (for example: $\pi/4$, left, and right polarization components) to determine the Stokes vector and subsequently to calculate the degree of polarization and the ellipticity.

The proposed technique is based on a modified Sagnac interferometer, where orthogonal polarization components are projected along the same direction by a polarizer. Their interference depends on their degree of correlation, and is directly related to the degree of polarization of the analyzed light.

The procedure can easily be understood on the basis of the interference laws of Fresnel and Arago.[1, 11, 78, 79] A generalization of the interference laws for any state of coherence

48

and polarization of the field was presented in the previous Section. The original laws 3 and 4 imply a relationship between the polarimetric characteristics of the light and the ability to interfere of orthogonal components subsequently brought in the same plane.

The modified Sagnac interferometer shown in Fig. 2.7 consists of a polarizing beam-splitter PBS and two mirrors M. The two counter-propagating beams are orthogonally polarized, and according to the interference law 1 (Section 2.1.3), they do not interfere at the output of the interferometer. However, if we use a polarizer with orientation θ with respect to the beamsplitter's coordinate system, the two orthogonal polarizations are now projected along the direction of the polarizer and can interfere if there is any deterministic phase relationship between them. The two beams are overlapped in the observation plane situated in the focal plane of a lens L.
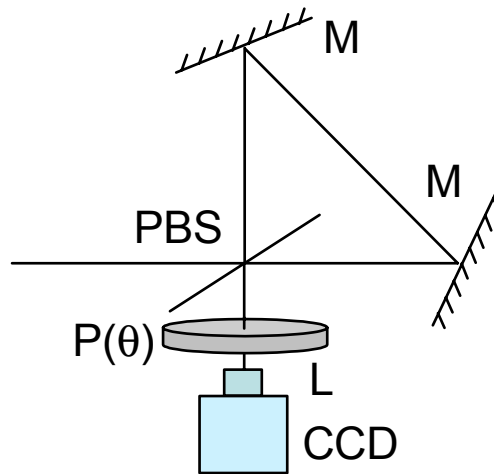
Figure 2.7. Modified Sagnac interferometer. PBS - polarizing beamsplitter, M - mirrors, P(θ) - polarizer oriented at θ, L - imaging optics for the CCD camera.

The electric fields to be overlapped on the CCD are

$$\mathbf{E}_1\left(\theta, \varphi_1\right) = P\left(\theta\right) P\left(0\right) P\left(0\right) \begin{bmatrix} E_x \\ E_y \end{bmatrix} \exp\left(i\varphi_1\right) = \tag{68}$$

$$= E_x \cos\left(\theta\right) \exp\left(i\varphi_1\right) \begin{bmatrix} \cos\left(\theta\right) \\ \sin\left(\theta\right) \end{bmatrix},$$

and, respectively,

$$\mathbf{E}_2\left(\theta, \varphi_2\right) = P\left(\theta\right) P\left(\pi/2\right) P\left(\pi/2\right) \begin{bmatrix} E_x \\ E_y \end{bmatrix} \exp\left(i\varphi_2\right) = \tag{69}$$

$$= E_y \sin\left(\theta\right) \exp\left(i\varphi_2\right) \begin{bmatrix} \cos\left(\theta\right) \\ \sin\left(\theta\right) \end{bmatrix}.$$

The phases φ_1 and φ_2 are the geometric phases accumulated by light travelling through the interferometer to the observation plane, and $P\left(\theta\right)$ is the Jones matrix of a polarizer.[80] $P\left(0\right)$ and $P\left(\pi/2\right)$ represent the effect of the polarizing beamsplitter on the incident light, and it is worth mentioning here that in the present configuration the light experiences two reflections at the beamsplitter along one propagation direction through the interferometer, and two transmissions along the other direction, seeing, actually, the same polarizer twice along each path.

The total intensity at an observation point Q on the CCD, calculated as $I\left(Q\right) = \langle\left(\mathbf{E}_1^* + \mathbf{E}_2^*\right) \cdot \left(\mathbf{E}_1 + \mathbf{E}_2\right)\rangle$, can be written as

$$I\left(Q\right) = I_c(Q) + I_{int}(Q) \tag{70}$$

50

where

$$I_c(Q) = I_x \cos^2(\theta) + I_y \sin^2(\theta) \tag{71}$$

$$I_{int}(Q) = 2\sin(\theta)\cos(\theta)\,\mathrm{Re}\left[J_{xy}\exp(i\Delta)\right] \tag{72}$$

and Re stands for real part, $\Delta = \varphi_2 - \varphi_1$. $I_c(Q)$ represents the incoherent addition of the intensities corresponding to the orthogonal components of the incident light ($I_m = J_{mm}$) overlapped by the polarizer. The second term in the Eq. 70, $I_{int}(Q)$, represents the interference of the orthogonal components of the electric field projected along the same direction by the polarizer.

By normalizing the off-diagonal element J_{xy} of the coherence matrix to the diagonal elements[81]

$$\mu_{xy} = \frac{J_{xy}}{\sqrt{J_{xx}J_{yy}}} = \left|\mu_{xy}\right|\exp(i\delta) \tag{73}$$

one obtains, as described in Section 1.3, a measure of the degree of correlation between E_x and E_y. Using formula 73 one can rewrite the Eq. 72

$$I_{int}(Q) = 2\sin(\theta)\cos(\theta)\sqrt{I_xI_y}\left|\mu_{xy}\right|\cos(\Delta + \delta), \tag{74}$$

where δ represents the retardance, the relative phase between the two orthogonal electric field components. For a certain orientation θ of the polarizer, $\left|\mu_{xy}\right|$ can be determined as the envelope of the interference fringes, while δ is given by the position of the fringes with respect to a reference that will be discussed in the following.

The magnitude $\left|\mu_{xy}\right|$ can be directly related to the degree of polarization starting from the formula 11

$$P = \sqrt{1 - \frac{4\det(J)}{[tr(J)]^2}} = \sqrt{1 - \frac{4\left(I_xI_y - |J_{xy}|^2\right)}{(I_x + I_y)^2}} = \sqrt{1 - \frac{4I_xI_y\left(1 - \left|\mu_{xy}\right|^2\right)}{(I_x + I_y)^2}}. \tag{75}$$

51

In fact, one can see from the Eq. 75 that $P = |\mu_{xy}|$ if the two intensities I_x and I_y are equal.

Three particular orientations of the polarizer are required for complete determination of the state of polarization. For simplicity, $0°$, $45°$, and $90°$ are chosen here. The Eq. 70 simplifies then to $I(0) = I_x$, $I(90) = I_y$, and $I(45) = (I_x + I_y)/2 + \sqrt{I_x I_y}\,|\mu_{xy}|\cos(\Delta + \delta)$. In an imaging configuration, $I(45)$ provides two parameters in only one shot; the envelope of the interference fringes gives $|\mu_{xy}|$ in every point of the image, while the position of the fringes with respect to a reference frame determines the retardance δ. The reference frame for the position of the fringes is given by an initial calibration of the imaging polarimeter using linearly polarized light for which $\delta = 0$. Four parameters I_x, I_y, $|\mu_{xy}|$, and δ are therefore obtained for every pixel from only three images denoted as $I(0)$, $I(90)$, and $I(45)$ allowing for complete determination of the state of polarization in either coherence matrix or Stokes formalism.

It is worth mentioning here that the fringe spacing is adjustable by translating one mirror of the interferometer, allowing for a tunable resolution in estimating the position and the envelope of the fringes, as opposed to the technique described in the Ref.[90] where the resolution is set by the apex of the birefringent prisms. This feature makes our technique attractive for analyzing scenes with either monotonic or sharp variations of the state of polarization across the image, the only limitation being the resolution of the imaging system.

In order to experimentally demonstrate our technique we need to generate a complex beam with the state of polarization varying across the beam. For this purpose an unpo-

52

larized He-Ne laser and a Mach-Zehnder configuration were used as shown in Fig. 2.8. Two orthogonal polarizers (along x and y directions) are used one in each arm of the Mach-Zehnder interferometer. Since the initial light is unpolarized, there is no deterministic phase relationship between the x and y components of the electric field at the output of the interferometer, and therefore no interference occurs in the observation plane. The degree of polarization of the output light can be varied between 0 and 1 by adjusting the intensity in one arm of the interferometer; for example, $P = 0$ if $I_x = I_y$, and $P = 1$ if either I_x or I_y are zero.
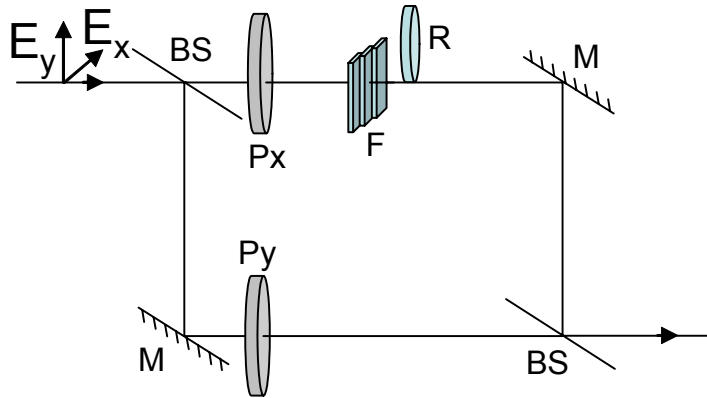
Figure 2.8. Mach-Zehnder interferometer. BS - non-polarizing beamsplitters, M - mirrors, Px, Py - horizontal and vertical polarizers, F - neutral density filters, R - retarder.

The degree of polarization can be varied in each point across the beam by using, for example, a spatial light modulator in between parallel polarizers in one arm of the interferometer. For simplicity, neutral density filters were used shifted with respect to each other across the beam to create steps in the intensity pattern. The variation of the retardance was created by simply inserting a waveplate approximately halfway across the

53

beam. An additional rotator is introduced after the generator to avoid the situation where linearly polarized light enters the analyzer along x or y direction. This is not a degenerate case since the formula 75 gives $P = 1$ if either I_x or I_y are zero and our analysis gives the correct state of polarization; however, no fringes are observed.

The state of polarization across the beam was measured using the modified Sagnac interferometer followed by a polarizer as described above. The state of polarization was also measured using a standard Stokes imaging polarimeter, by recording the x, y, 45°, and right polarization components with suitably oriented polarizer and quarter wave-plate in front of the CCD camera. Note here that the Sagnac interferometer was removed from the optical path.

Fig. 2.9 shows the images obtained with our technique based on the Sagnac interferometer. First row shows the experimental images I_x, I_y and I_{45}. Also the top right corner image represents the interference pattern, described by the Eq. 74 for $\theta = 45°$ and normalized to $\sqrt{I_x I_y}$. The magnitude of the fringes, their envelope provides $|\mu_{xy}|$, the modulus of the degree of polarization coherence, while the position of the fringes gives the retardance δ. The envelope of the fringes is simply obtained as the magnitude of the Hilbert transform for each line of the image, then the position of the fringes is derived by fitting them with a cosine function multiplied with $|\mu_{xy}|$. Therefore, δ and $|\mu_{xy}|$ are determined for each pixel of the image. The interference pattern in the top right corner image clearly shows a displacement of the fringes at the edge of the retarder and at the line 100. Above line 100 and to the left of the retarder, the polarized component of light is linear, and the position of the fringes here provides the reference frame for the retardance.

Second row in Fig. 2.9 shows the calculated normalized Stokes vector components q, u, and v and the degree of polarization P.
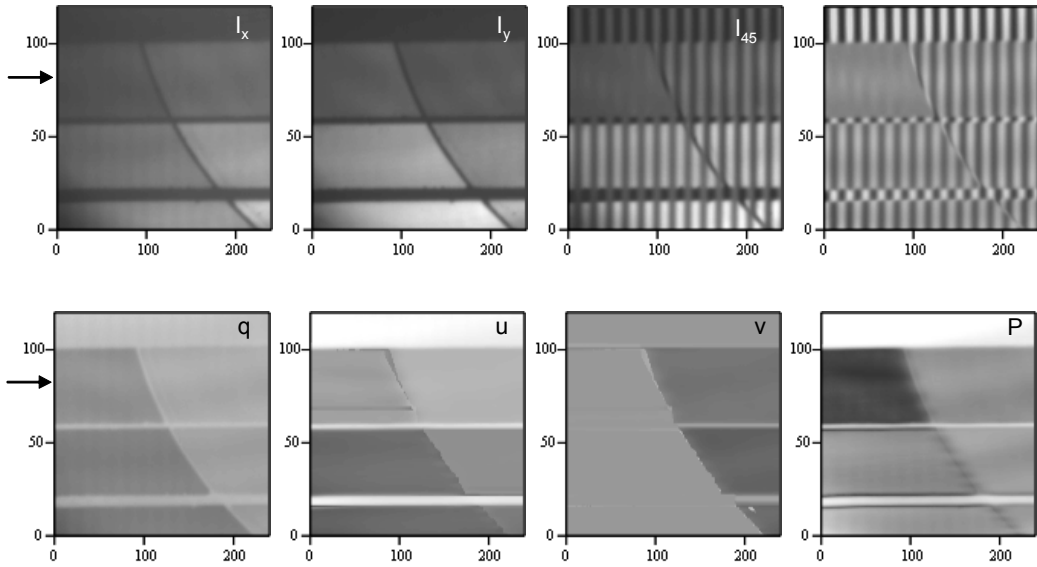
Figure 2.9. Images obtained with the Sagnac interferometer. First row - experimental images I_x, I_y and I_{45}, and the normalized interference pattern. Second row - calculated normalized Stokes vector components q, u, and v and the degree of polarization P.
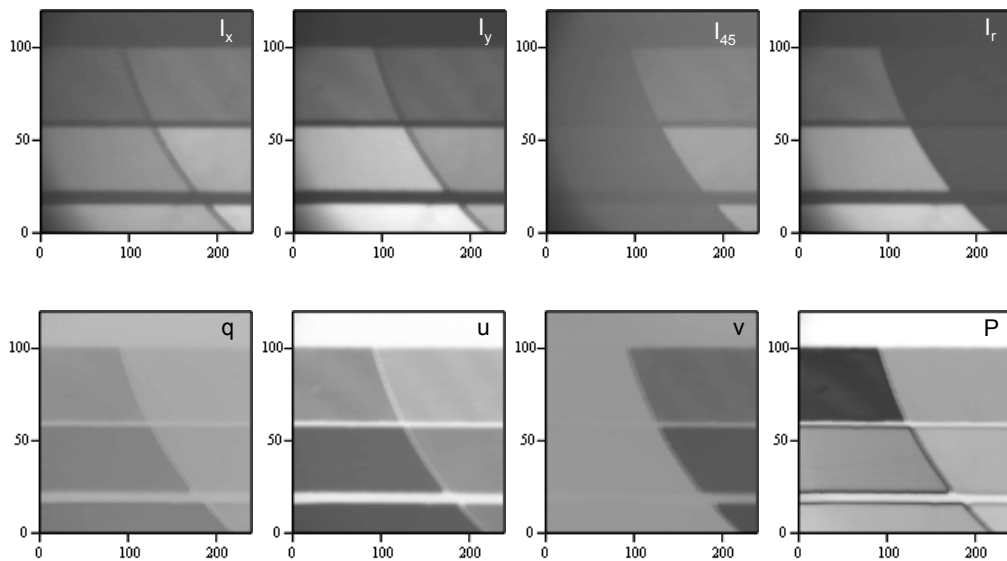
Figure 2.10. Images obtained with standard Stokes polarimetry. First row - experimental images I_x, I_y, I_{45}, and I_r. Second row - calculated normalized Stokes vector components q, u, and v and the degree of polarization P.

55

Fig. 2.10 shows the images obtained with standard Stokes polarimetry. The first row displays the experimental images I_x, I_y, I_{45}, and I_r, and the second row shows the calculated normalized Stokes vector components q, u, and v and the degree of polarization P. The images shown in both the Fig. 2.9 and 2.10 are scaled with 90 shades of grey. White represents 1 for q, u, v, P, and the interference term, and an intensity in arbitrary units of 675 for I_x, I_y, and I_{45}, in Fig. 2.9, and 500 for I_x, I_y, I_{45}, and I_r in Fig. 2.10. Black represents -1 for q, u, v, and the interference term, and 0 for all the other images.

In order to compare the results of standard Stokes polarimetry and our technique, the plots of the total intensity, normalized Stokes vector components q, u, and v, the degree of polarization P, and the retardance δ (corresponding to the line indicated by the arrows in Fig. 2.9) are presented in Fig. 2.11. This comparison shows a very good agreement between the two techniques demonstrating the validity of our method. One can clearly see the step in retardance introduced by the retarder, that also modifies the Stokes vector components.

The intensities I_x and I_y are roughly equal on the left of the retarder and in between lines 60 and 100. One can see that there are no fringes in this area (interference pattern in Fig. 2.9), and consequently, the degree of polarization is small (Fig. 2.11). The retarder changes the ratio of the intensities I_x and I_y, and also introduces a phase relationship between the x and y components of the electric field propagating through the top arm of the Mach-Zehnder interferometer. Therefore, the degree of polarization is changed, as indicated in Fig. 2.11. Note that the edges of the filters and of the retarder are clearly visible in both Figs. 2.9 and 2.10, and also correspond to the jumps in Fig. 2.11.

56
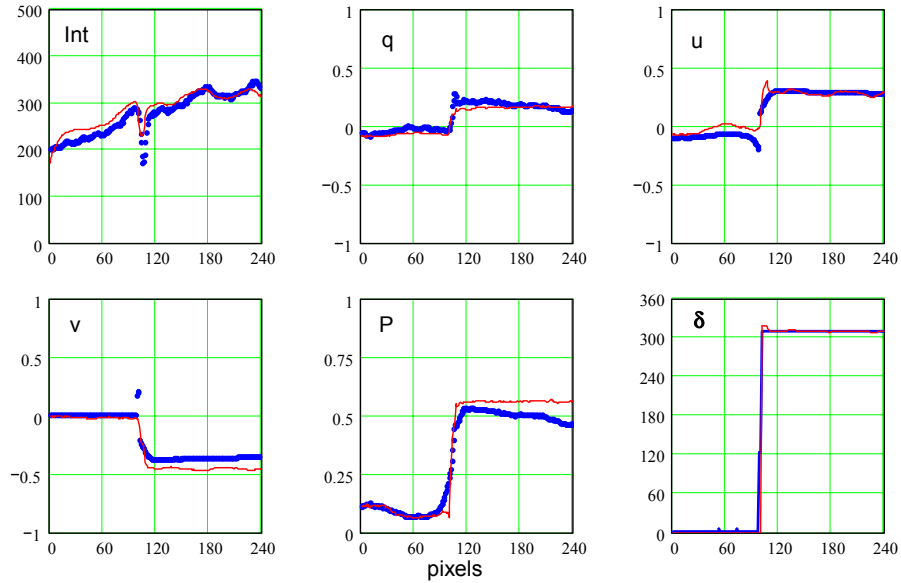
Figure 2.11. Comparison between the results of standard Stokes polarimetry (line) and of our technique (dots). Plots of the total intensity Int, normalized Stokes vector components q, u, and v, the degree of polarization P, and the retardance δ corresponding to the line indicated by the arrows in Fig. 2.9.

It is worth mentioning that if there is no phase relationship between the x and y components of the electric field, the fringe patterns corresponding to $q > 0$ ($I_x > I_y$) and $q < 0$ ($I_x < I_y$) are π phase shifted. If the intensities are equal, the two fringe patterns compensate each other giving no interference and the degree of polarization is zero.

In conclusion, a new measurement technique for imaging polarimetry based on a modified Sagnac interferometer was presented here. The comparison between the Stokes components obtained with our technique and standard Stokes polarimetry shows a very good agreement. This technique can also be regarded as a direct illustration of the interference laws of Fresnel and Arago. In certain applications where the orientation of the state of polarization is known and only the degree of polarization and the retardance fluctuate in time or across the image, one can use our technique to monitor these changes

57

in real time. The main advantage over the standard Stokes polarimetry is that only one image is required to obtain both the degree of polarization and the retardance, as opposed to at least three images in Stokes polarimetry. The fringe spacing is easily adjustable allowing for improved resolution in determining the state of polarization when necessary, as opposed to previously published interferometric techniques.

2.2. Mueller polarimetry

In certain applications, the transfer of the state of polarization through a system (the Mueller matrix), rather than the state of polarization, is of interest. The Mueller matrix elements are related to relevant physical characteristics as described in Section 1.5. Determination of the Mueller matrix requires measurement of the state of polarization for both the incident and the scattered light. A short review of the state-of-the-art in the field is given in this Section, followed by the development of new measurement techniques. Practical aspects of Mueller polarimetry are also discussed.

2.2.1. Classification of measurement techniques

In general, modulation of the state of polarization is required for precise and fast measurement of the Stokes vector or of the Mueller matrix. In the following, a classification of the experimental techniques is presented from the point of view of modulation of the state of polarization.

58

2.2.1.1.1. Sequential measurements

The classical method of measuring the Stokes vector involves six measurements according to Eq. 2. Based on the property $I_x + I_y = I_{45°} + I_{-45°} = I_l + I_r = I$, Collett[91] proposed a method involving just four measurements ($I_x, I_y, I_{45°}, I_l$). Four is practically the minimum number of measurements required for complete determination of the Stokes vector. For the purpose of noise reduction, more measurements are sometimes performed, over-determining the Stokes vector or the Mueller matrix. For circularly polarized input, Ambirajan and Look[92] measure the Stokes vector of scattered light by rotating a retarder at 11 positions. To determine the Mueller matrix, Cariou et al.[13] use two pairs of polarizer/quarter-wave plate. The two polarizers are crossed and stationary, while the two quarter-wave plates are rotated with step motors in 64 combinations.

Bickel and Bailey[93] describe all the combinations of input and output polarizing optics (open hole, polarizer, quarter-wave plate) required for complete determination of the Mueller matrix, giving also physical interpretation to matrix elements.

McClain et al.[94] use two pairs half-wave/quarter-wave plates, one for the incident beam, one for the scattered beam. Each of the four retarders has two angular positions, providing 16 possible combinations. A decomposition technique is used to calculate the Mueller matrix.

None of these methods uses a modulation of the intensity or retardation, and all of them require many consecutive measurements for complete determination of the Mueller matrix.

2.2.1.1.2. Simultaneous measurements of the Mueller matrix

In 1978, Azzam[82] proposed a technique in which all 16 Mueller matrix elements are retrieved from only one detected signal by performing a discrete Fourier transform. The polarizing and analyzing optics consist of stationary parallel polarizers and of two synchronously rotating quarter-wave retarders at angular speeds ω and 5ω. Goldstein[95] uses this method in an infrared polarimeter. To simulate the rotation of each retarder, Azzam[82,96] proposes the use of pairs of Faraday cells.

2.2.1.1.3. Sequential generation - simultaneous analysis

The technique of continuously rotating-retarder fixed-analyzer was first introduced by Sekera.[97] Fourier decomposition of the time varying detected signal gives simultaneously all four Stokes vector components.

The generation part of the incident state of polarization, used by Lewis and Jordan[98,99] for the Mueller matrix measurement, is composed of one fixed polarizer and two adjustable retarders (half-wave and quarter-wave). Six input states are generated sequentially, and the scattered light is analyzed using Sekera's[97] technique.

The idea of division of amplitude for simultaneous measurement of all four Stokes parameters has been introduced by Azzam.[100] The division-of-amplitude photopolarimeter (DOAP) consist of a beamsplitter and two Wollaston prisms followed by four detectors. Azzam,[101] also describes a different version of DOAP that uses four photodetectors with different spatial orientation. The incident beam is partially reflected and partially absorbed, by the first three detectors while the fourth detector is totally absorbing. In a

third version of the DOAP,[102] the four detectors receive light multiply reflected in a paral-lel slab. An important problem in the last two methods is that the four detectors receive different levels of intensity with negative impact on the signal-to-noise ratio. Incidence angle is also extremely critical.

Krishnan and Nordine[59, 103] describe a method in which the input states of polarization are sequentially generated involving a fixed polarizer and a quarter-wave plate rotated in steps of $10°$. The state of polarization of the scattered light is analyzed by a DOAP as proposed by Azzam.[100] Their second paper also describes a polarization state generator based on two liquid crystal variable retarders that generate a series of linear, elliptical and circular polarization states to overdetermine the Mueller matrix.

2.2.1.2. Phase-modulation polarimetry

2.2.1.2.1 Consecutive measurements of the Mueller matrix elements

Bille[19] presents a technique involving four Pockels cells, four pre-selected input states being generated sequentially. The reflected light is analyzed in the same pre-selected states. Sixteen consecutive measurements are performed, allowing determination of the whole Mueller matrix.

2.2.1.2.2. Simultaneous measurement of specific Mueller matrix elements

A few methods have been published about Mueller matrix measurement using one or two photoelastic modulators (PEM). What these methods have in common is that just groups of matrix elements can be determined for each configuration of the setup.

61

Multiple configurations involving rotations of the active elements are required for complete determination of the Mueller matrix.

Jasperson and Schnatterly[104] proposed in 1969 the use of PEM in ellipsometry. Hunt and Huffman[105] used it in 1973 to investigate systems of spherical scatterers. Bell[32] improved the method to measure all 16 elements of the matrix in groups of three elements, given four orientations of the analyzer for each of the two positions of the PEM.

Salzman et al.[16] proposed a method in which only fourteen matrix elements can be determined in two configurations of an apparatus using two PEM's. Anderson[106] and Jellison and Modine[107] suggested an apparatus that uses two PEM's with different resonant frequencies (50 and 60kHz). To determine the whole Mueller matrix, four configurations of the apparatus are necessary. Anderson[106] suggested lock-in detection which would result in sequential measurement of eight matrix elements in each configuration, while Jellison and Modine[107] use a spectral analysis method for simultaneous measurement of groups of eight elements. A similar apparatus has been used by DeVolk et al.[17] for biological particle identification.

2.2.1.2.3. Simultaneous measurement of all Mueller matrix elements

Thompson et al.[108] proposed a photopolarimeter involving four Pockels cells with different orientations, modulated at four different frequencies. The detected signal is analyzed with sixteen lock-in amplifiers. The method is fast, but its drawback is the complexity of the electronics.

Compain and Drevillon improved the Mueller matrix measurement methods by modulating the incident state of polarization. The four Stokes parameters are independently

modulated by a coupled-phase-modulator[109,110] made of two electro-optic phase modulators with a partial polarizer and phase shifter (PPS) in between. They also propose a new polarization modulator[111] based on a double-pass through one PEM with a PPS in between the two passes. For measurement of the state of polarization of the scattered light they suggest the DOAP technique outlined by Azzam.[100] However, the measurements are practically done with a manual single-channel polarimeter[109] that simulates the multichannel one.[112] They combine the new polarization modulator with the DOAP into an ellipsometer.[113]

2.2.1.2.4. Sequential generation - simultaneous analysis

The method presented below can be described as sequential generation - simultaneous analysis. It allows simultaneous measurement of all four Stokes vector components using only one PEM in a single-pass configuration. The beam is split in two by a non-polarizing beamsplitter, analyzed by two polarization channels, and read by two detectors. Four input states of polarization are sequentially produced by the state of polarization generator and the Mueller matrix is obtained with simple matrix algebra after measuring the four output states of polarization.

2.2.2. State of polarization generation

For the generation of the state of polarization, a polarizer P and a combination of two liquid crystal variable retarders LCVR1 and LCVR2 are used as shown in Fig. 2.12. LCVR1 is rotated 45° with respect to the axis of the polarizer, while LCVR2 has one

63

axis (slow or fast) parallel to P. Both variable retarders are controlled from a computer through a National Instruments data acquisition board (DAQ). The desired retardation is introduced by each of the two retarders when a specific voltage is applied on the retarder from the computer.
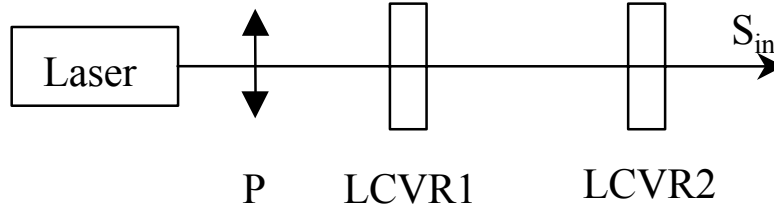
Figure 2.12. Polarization generation unit; P is a polarizer and LCVR1, LCVR2 are liquid crystal variable retarders.

Starting from a linearly polarized input in horizontal direction $S_0 = \{1, 1, 0, 0\}^T$ (after the polarizer P), the generated state of polarization S_{in} can be deduced using the Mueller matrices $M_1(\delta_1)$ and $M_2(\delta_2)$ associated with the two retarders:

$$M_1(\delta_1) = \begin{bmatrix} 1 & 0 & 0 & 0 \\ 0 & \cos(\delta_1) & 0 & -\sin(\delta_1) \\ 0 & 0 & 1 & 0 \\ 0 & \sin(\delta_1) & 0 & \cos(\delta_1) \end{bmatrix} \tag{76}$$

$$M_2(\delta_2) = \begin{bmatrix} 1 & 0 & 0 & 0 \\ 0 & 1 & 0 & 0 \\ 0 & 0 & \cos(\delta_2) & \sin(\delta_2) \\ 0 & 0 & -\sin(\delta_2) & \cos(\delta_2) \end{bmatrix}. \tag{77}$$

64

$S_{in}(\delta_1, \delta_2)$ is given by:[59]

$$S_{in}(\delta_1, \delta_2) = M_2(\delta_2)M_1(\delta_1)S_0 = \begin{bmatrix} 1 \\ \cos(\delta_1) \\ \sin(\delta_2)\sin(\delta_1) \\ \cos(\delta_2)\sin(\delta_1) \end{bmatrix}. \qquad (78)$$

Any possible state of polarization can be obtained in this way if δ_1 varies between $0°$ and $180°$ and δ_2 between $0°$ and $360°$. Eq. 78 resembles the transformation from Cartesian to spherical coordinates, and is the basis for representation of a state of polarization on the Poincarè sphere in which any point on the sphere of radius 1 (centered in the origin of the coordinate system (q, u, v)) represents a pure state of polarization. In this representation $S_{in}(\delta_1, \delta_2)$ covers the whole Poincarè sphere for these variation intervals of δ_1 and δ_2.

An equivalent generation system, which can also produce any state of polarization starting from a linear input, has a quarter-wave plate in between the two liquid crystal variable retarders. In this configuration, the two modulators are parallel, at 45° with respect to the polarizer P, while the quarter-wave plate has the slow axis parallel to P. LCVR1 and the quarter-wave plate act together as a polarization rotator, the polar orientation of the generated linearly polarized light being given by half the phase shift introduced by LCVR1. 0° to 90° rotation of the polarization direction together with 0° to 360° phase shift introduced by LCVR2 are enough to cover the whole Poincarè sphere.

Liquid crystal modulators present the advantage of being extremely easy to use and less expensive than any other light modulator; most important, in comparison with electro-optic modulators, they are driven by applying small voltages. In our setup, the two

65

LCVR's are directly controlled by a computer through a DAQ. There is no need for external power supplies, since the LCVR can be easily powered from the DAQ outputs.

The retardance introduced by a LCVR decreases approximately 0.4% per °C. However, due to the very short duration of the measurement, this is not an issue here. The resolution for controlling the voltage applied to the LCVR is 16 bits, i.e. about $15\mu V$, which corresponds to at most $7.5 \cdot 10^{-3}$nm in retardance introduced by the LCVR.

2.2.3. Phase-modulation analysis

A new technique for measuring the state of polarization of light is presented in this Section. The Stokes analyzer employs a single-pass photoelastic modulator (PEM). A simple Fourier decomposition of the two measured signals allows simultaneous determination of all Stokes vector components. There are no moving parts involved, which simplifies the mechanical setup (allowing for a compact design) and the control of the measurement process. This system used together with the Stokes generator described above, permits the complete determination of the Mueller matrix. Four input states of polarization are generated sequentially, and for each of them, all four Stokes vector parameters are simultaneously measured. A straightforward matrix algebra is used to calculate all sixteen Mueller matrix elements given the four generated input states of polarization and the four measured output states. The entire process (control of the polarization generation unit, measurement and analysis) is controlled by a computer in LabVIEW through a National Instruments DAQ. There is no need for lock-in amplifiers, sophisticated electronics and optics, high-voltage amplifiers and power supplies for electro-optic modulators.

66

Let us consider a setup in which the light passes first through a retarder, described by Eq. 8, followed by a polarizer described by Eq. 6. The detector would be sensitive only to the total intensity which is the first element of the Stokes vector. Given an incident Stokes vector $S_{in} = \{I_0, Q_0, U_0, V_0\}^T$, the output Stokes vector is obtain from: $S_f = M_{pol}(\theta) M_w(\delta) S_{in}$ for which the total intensity I_{final} is given by:

$$I_{final} = \frac{1}{2}\{I_0 + Q_0 \cos(2\theta) + \sin(2\theta)[U_0 \cos(\delta) + V_0 \sin(\delta)]\}. \tag{79}$$

Different retardations δ (or a modulation of the retardance as it will be seen here) allow U_0 and V_0 to be determined independent of the polarizers position (different from 0 or $\pi/2$). The problem is that the polarizer has to be rotated in two different positions θ_1 and θ_2 to allow I_0 and Q_0 to be determined independently. This is solved using a non-polarizing beamsplitter, two polarizers at two different orientations and two detectors in a simple configuration as presented in Fig. 2.13.
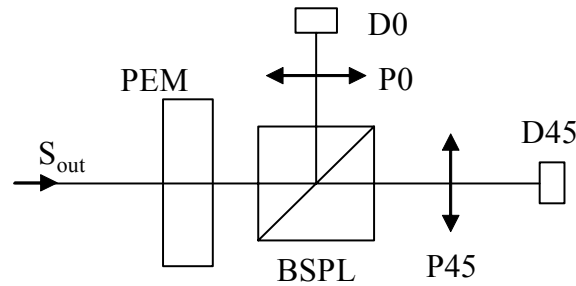
Figure 2.13. Polarization analyzer unit; PEM is a photoelastic modulator, BSPL is a non-polarizing beamsplitter, P0 and P45 are polarizers oriented horizontal, respectively at 45°, and D0, D45 are detectors.

The laser beam for which the Stokes vector S_{out} is to be measured, is first modulated by the photoelastic modulator PEM that introduces a time dependent retardation of the

67

form: $\delta(t) = \delta_o \cos(2\pi f t)$ between the two orthogonal components of the electric field, where δ_o is the maximum retardance and $f = 50 kHz$ is a fixed resonant modulation frequency. The non-polarizing beamsplitter BSPL splits the signal in two equal components that are passed through two polarizers P0 and P45 oriented at $0°$ and $45°$ and analyzed by two detectors D0 and D45. D0 gives a DC signal (DC_0), while D45 gives a time varying signal which is Fourier analyzed to extract the DC term (DC_{45}) and the first two harmonics (I_f, I_{2f}).

The relationship between S_{out} (four components) and $(DC_0, DC_{45}, I_f, I_{2f})$ can be determined by knowing the Mueller matrices of PEM, BSPL, P0 and P45. Assuming that all optical components are ideal and have the proper orientation, we use Eq. 8 in the form $M_{PEM}(\delta(t)) = Mw(\delta(t))$ for PEM, and the following matrices for P0, and P45:

$$
M_{pol}(0) = \frac{1}{2}
\begin{bmatrix}
1 & 1 & 0 & 0 \\
1 & 1 & 0 & 0 \\
0 & 0 & 0 & 0 \\
0 & 0 & 0 & 0
\end{bmatrix}
; M_{pol}(45) = \frac{1}{2}
\begin{bmatrix}
1 & 0 & 1 & 0 \\
0 & 0 & 0 & 0 \\
1 & 0 & 1 & 0 \\
0 & 0 & 0 & 0
\end{bmatrix} .
\tag{80}
$$

It is assumed here that the non-polarizing beamsplitter is ideal, and does not affect the state of polarization both in transmission and in reflection. We can obtain the total intensity on the two detectors by either applying $S_{final} = M_{pol}(\theta) M_{PEM}[\delta(t)] S_{out}$ for the particular matrices of the two polarizers as given in Eq. 80 and keeping just the first element of the Stokes vector as total intensity, or, simpler, particularizing Eq. 79 for $0°$ and $45°$. If i_0 is the current read by the detector D0, and i_{45} is the current read by the

detector D45, they can be related to the Stokes vector parameters through:

$$i_0 = \frac{1}{2}(I_0 + Q_0) \tag{81}$$

$$i_{45}(t) = \frac{1}{2}\{I_0 + U_0 \cos[\delta(t)] + V_0 \sin[\delta(t)]\}. \tag{82}$$

For a time dependent retardation of the form $\delta(t) = \delta_o \cos(2\pi f t)$, a Bessel-Fourier decomposition for $\sin[\delta(t)]$ and $\cos[\delta(t)]$ is generally used:[11,63]

$$\sin[\delta(t)] = 2\sum_{k=0}^{\infty} J_{2k+1}(\delta_o) \sin[(2k+1)\omega t] \tag{83}$$

$$\cos[\delta(t)] = J_0(\delta_o) + 2\sum_{k=1}^{\infty} J_{2k}(\delta_o) \cos(2k\omega t). \tag{84}$$

The two currents i_0 and i_{45} are recorded for a full period. The value of δ_o is chosen to be equal to 2.405 such that $J_0(\delta_o) = 0$. By averaging i_0 and i_{45}, the DC components are obtained as $DC_0 = I_0 + Q_0$, $DC_{45} = I_0$, and, respectively, by averaging $i_{45}\sin(\omega t)$ and $i_{45}\cos(2\omega t)$, the coefficients of the first two harmonics I_f and I_{2f} (the coefficients of $\sin(\omega t)$ and $\cos(2\omega t)$) are obtained as $I_f = V_0 J_1(\delta_o)$ and $I_{2f} = U_0 J_2(\delta_o)$.

Finally, the four components of the Stokes vector are obtained:

$$I_0 = DC_{45} \tag{85}$$

$$Q_0 = DC_0 - DC_{45} \tag{86}$$

$$U_0 = \frac{I_{2f}}{J_2(\delta_o)} \tag{87}$$

$$V_0 = \frac{I_f}{J_1(\delta_o)}. \tag{88}$$

The experimental setup includes a National Instruments DAQ for reading the two currents i_0 and i_{45}, and all the numerical analysis was initially performed in LabVIEW. Measurement of one state of polarization requires simultaneous reading of the two currents

69

i_0 and i_{45} over a period of time $T = 1/f$ of about $20\mu s$. Averaging 100 times for noise reduction gives a time frame of $2ms$ for reading one state of polarization. The time required by the LCVR's to switch between two states of polarization can be made as small as $10ms$. Quasi-real-time measurement of the Mueller matrix is in this way possible allowing monitoring, for instance, the structural dynamics in a variety of particulate systems.

To speed up the measurement process, the Fourier analysis can be done directly using dedicated electronics instead of numerical analysis in the computer. Also, the precision can be improved by modulating the laser power at 1kHz. Filtering out the two detected signals at this frequency, instead of reading DC terms, removes the background noise. The blueprints of the electronics developed for this purpose are presented in Appendix B. Basically, there are 4 channels consisting of bandpass filters centered at 1kHz (2 channels), 50kHz, and 100kHz and a few amplifying stages. By squaring the output of the bandpass filter, or multiplying it with the reference frequency, the square of the amplitude is obtained after a low pass filter that selects only the DC term; $[A\sin(x)]^2 = \frac{A^2}{2}[1 - \cos(2x)]$. The outputs of the 4 channels are proportional to the squares of the 4 Fourier components described above.

Generally, four input states of polarization are required for complete Mueller matrix measurement. In our setup, which is schematically depicted in Fig. 2.14, four input states of polarization $S_{in}(\delta_1, \delta_2)$ are generated sequentially (four combinations of δ_1 and δ_2) and for each of them, the state of polarization S_{out} of the light emerging from the sample is measured. The equation $S_{out} = MS_{in}$ provides now a system of 16 equations with

70

unknowns $M_{i,j}$ with $i, j = 1..4$. The Mueller matrix M associated with the investigated sample is obtained by solving this system.
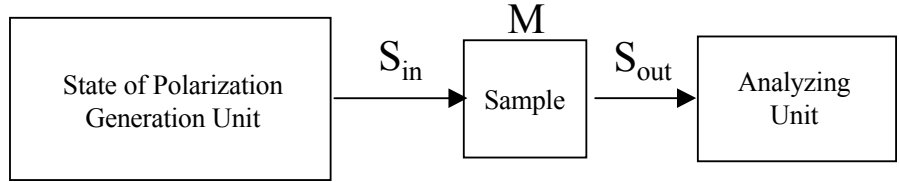
Figure 2.14. Schematic setup for Mueller matrix measurement in transmission.

A reliable way to validate and to check the performance of the present method is by testing standard optical elements such as good quality polarizers and wave plates. The system was tested by measuring the Mueller matrix of a polarizer, and of a quarter-wave plate, each of them rotated in steps of $5°$ from $0°$ to $180°$. The results for the polarizer are presented in Fig. 2.15, and for the quarter-wave plate in Fig. 2.16; the crosses indicate experimental points while the continuous curve is the theoretical prediction as given in Eq. 6, and Eq. 7, respectively.

As a measure of the system's performance, the deviations of the experimental values from the theoretical predictions were quantified by calculating the standard deviation of the Mueller matrix elements. The average standard deviations for the Mueller matrix elements of the polarizer shown in Fig. 2.15, and the quarter-wave plate in Fig. 2.16, are 1.95% and 2.5%, respectively. These deviations could be attributed to both statistic and systematic errors. Statistic, random errors due to laser power fluctuations, electrical noise, and detector dark current fluctuations are minimized by averaging. Systematic errors could be reduced mainly through improving the calibration process, also described

71

in this Chapter. In principle, small errors in the calibration matrix M_{coeff} in Eq. 99 could lead to significant errors in the measured Mueller matrix.
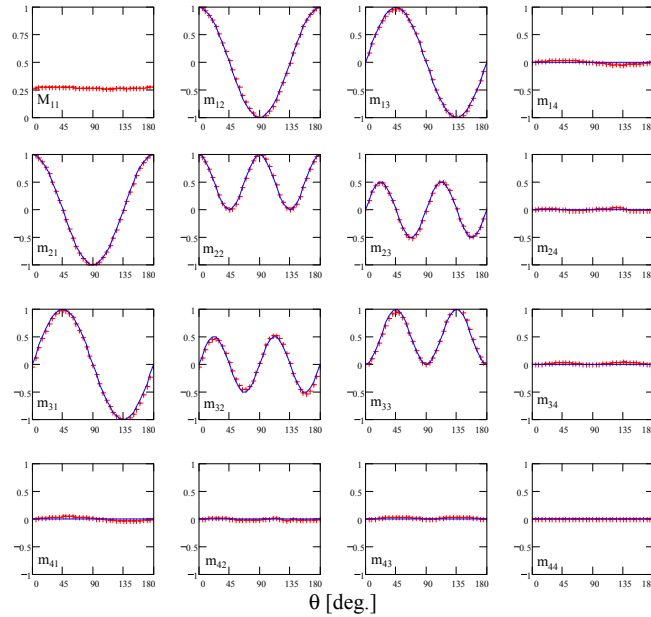
Figure 2.15. Mueller matrix of a polarizer rotated in steps of 5° from 0° to 180°.
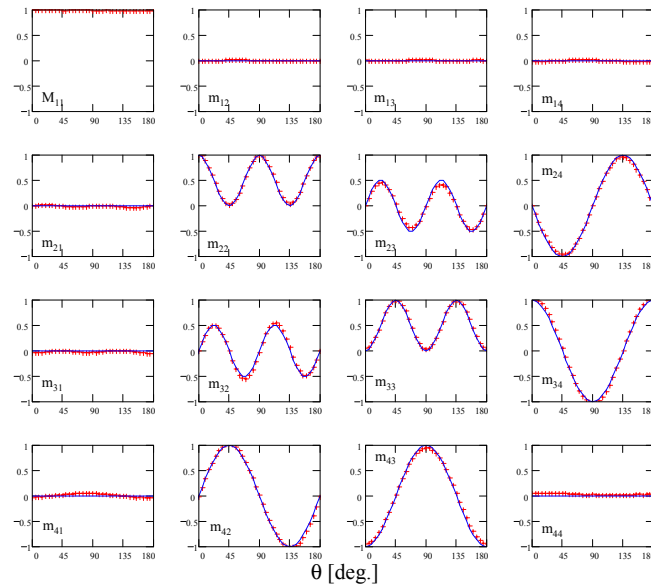
Figure 2.16. Mueller matrix of a quarter-wave plate rotated in steps of 5° from 0° to 180°.

The analysis unit described here can be used independently for measuring just the state of polarization in cases where the Mueller matrix is not required. In combination with the state of polarization generator, the analyzing unit can be used for measuring, for example, the Mueller matrix as function of scattering angle, optical density, shape and orientation of scatterers, or monitoring the structural dynamics of various colloidal systems. Practically, scattered light at any angle between 0° and 180° can be measured by placing the analyzing unit on a rotation table with the axis of rotation passing through the sample. The measurements can also be made in exact backscattering using an additional beamsplitter cube to separate the light scattered by the sample, from the incident beam. In comparison with the transmission measurement, the only difference is that the Mueller matrix of the beamsplitter has to be known for both transmission and reflection in order to relate the real S_{in} and S_{out} (incident and reflected from the sample), with the known S'_{in} (generated) and the measured S'_{out}.

A simplified setup involving no moving parts, that allows simultaneous measurement of all four Stokes parameters, and real-time Mueller matrix measurement, was presented here. The method can be described as sequential generation - simultaneous analysis, where LCVR's are used to control the incident polarization state, having the advantage of being directly driven by a computer. The measurement of the state of polarization involves phase modulation, analysis in two polarization channels, and Fourier decomposition of the detected signals. An overall accuracy better than 2.5% was demonstrated through measurements on standard optical elements. The ability to complete a Mueller matrix measurement in less than 50ms is appealing for monitoring structural dynamics in a

73

variety of applications. The setup is designed to specifically investigate the polarization signature of particulate systems with high volume fractions. A detailed analysis of the Mueller matrix could reveal comprehensive information about the scattering medium, such as size, concentration, shape (deviation from sphericity) of the scatterers, optical activity, global depolarization effects (depolarization index), as well as effects specific to different types of illumination (linear, circular or elliptical polarization).

2.2.4. Static analysis

This second method involves no time modulation of the retardance for any of the active elements in the Stokes generator or analyzer. Fast nodulation would not be suitable for the type of detectors (photomultiplier - PMT, charge-coupled device - CCD) required in certain applications. As mentioned before, the measurement technique has to be chosen based on the specifics of the experiment. The detector of choice in light scattering experiments is, in general, the photomultiplier, being very sensitive to very low power optical signals. The CCD cameras used in imaging applications are by definition "slow" detectors. The method described here uses PMT's as detectors. The main advantage of this technique is that it provides a high dynamic range in measuring very faint signals typical for multiple scattering. The "data" recorded is a photon count.

The Stokes analyzer acquires sequentially two pairs of data in two polarization channels for complete determination of the Stokes vector. If combined with the Stokes generator, as previously described, the system shown in Fig. 2.17 allows full determination of the Mueller matrix.

74

Some of the experimental results obtained with this system will be presented here in subsequent Chapters. A dual channel Stanford Research counter is used to determine the photon count. The result is transmitted to a computer through a GPIB interface and the Mueller matrix is calculated in LabVIEW. The Stokes analyzer rotates around the sample, allowing measurement of the scattering matrix (Mueller matrix as function of the scattering angle). The system is completely automatic; the computer controls the Stokes generator, the counter, the rotation stage, and the data acquisition.
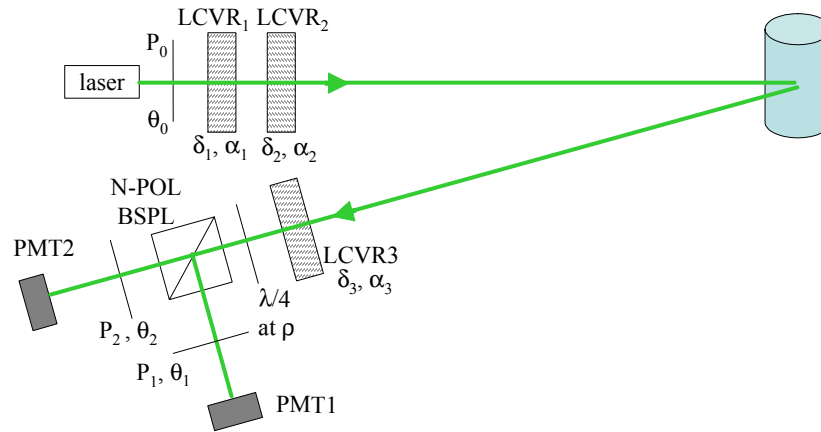
Figure 2.17. Scattering matrix polarimeter.

In the Stokes analyzer, the light first passes through a variable retarder (LCVR3), through a quarter-wave plate oriented at ρ with respect to LCVR3, and then through a non-polarizing beamsplitter. The two polarizers P1 and P2 oriented at θ_1 and θ_2 analyze the light emerging from the beamsplitter. It is assumed here that the non-polarizing beamsplitter is ideal, and does not affect the state of polarization both in transmission and in reflection.

75

Let us consider a setup in which the light passes first through a variable retarder, described by Eq. 8, followed by a quarter-wave plate oriented at an angle ρ as described by Eq. 7, and then through a polarizer oriented at θ and described by Eq. 6. The detector would be sensitive only to the total intensity which is the first element of the Stokes vector. Given an incident Stokes vector $S_{in} = \{I_0, Q_0, U_0, V_0\}^T$, the output Stokes vector (for the light incident on the detector) is obtained from $S_f = M_{pol}(\theta)M_{\lambda/4}(\rho)M_w(\delta)S_{in}$ and the total intensity I_f is

$$I_f(\delta, \rho, \theta) = \frac{1}{2}[I_0 + Q_0 f_1(\rho, \theta) + U_0 f_2(\delta, \rho, \theta) + V_0 f_3(\delta, \rho, \theta)], \tag{89}$$

where

$$
\begin{aligned}
f_1(\rho, \theta) &= \cos[2(\theta - \rho)]\cos(2\rho) \tag{90} \\
f_2(\delta, \rho, \theta) &= -\sin(\delta)\sin[2(\theta - \rho)] + \cos[2(\theta - \rho)]\cos(\delta)\sin(2\rho) \\
f_3(\delta, \rho, \theta) &= \cos(\delta)\sin[2(\theta - \rho)] + \cos[2(\theta - \rho)]\sin(\delta)\sin(2\rho).
\end{aligned}
$$

In the two channel configuration, the Eq. 89 is particularized for the two orientations of the polarizers θ_1 and θ_2. For each of the two retardations δ_1 and δ_2, introduced by the LCVR3, the two detectors acquire simultaneously data as follows: for δ_1, detector 1 acquires data $I_1 = I_f(\delta_1, \rho, \theta_1)$ and detector 2 acquires data $I_2 = I_f(\delta_1, \rho, \theta_2)$, and for δ_2, detector 1 acquires data $I_3 = I_f(\delta_2, \rho, \theta_1)$ and detector 2 acquires data $I_4 = I_f(\delta_2, \rho, \theta_2)$.

The Eq. 89 can be written in matrix form

$$
\begin{bmatrix} I_1 \\ I_2 \\ I_3 \\ I_4 \end{bmatrix} = \frac{1}{2} T(\delta_1, \delta_2, \rho, \theta_1, \theta_2) \begin{bmatrix} I_0 \\ Q_0 \\ U_0 \\ V_0 \end{bmatrix}, \tag{91}
$$

where

$$
T(\delta_1, \delta_2, \rho, \theta_1, \theta_2) = \begin{bmatrix} 1 & [f_1(\rho, \theta_1)] & [f_2(\delta_1, \rho, \theta_1)] & [f_3(\delta_1, \rho, \theta_1)] \\ 1 & [f_1(\rho, \theta_2)] & [f_2(\delta_1, \rho, \theta_2)] & [f_3(\delta_1, \rho, \theta_2)] \\ 1 & [f_1(\rho, \theta_1)] & [f_2(\delta_2, \rho, \theta_1)] & [f_3(\delta_2, \rho, \theta_1)] \\ 1 & [f_1(\rho, \theta_2)] & [f_2(\delta_2, \rho, \theta_2)] & [f_3(\delta_2, \rho, \theta_2)] \end{bmatrix}. \tag{92}
$$

The four Stokes vector components I_0, Q_0, U_0, and V_0 can be determined by recording I_1, I_2, I_3, and I_4 and inverting the Eq. 91. The optimization problem,[97–102] consists in this configuration in determining the values of δ_1, δ_2, θ_1, θ_2, and ρ for which the measurement would be less affected by errors.

A simpler optical configuration would be without the quarter-wave plate shown in Fig. 2.17. The final Stokes vector would be given by $S_f = M_{pol}(\theta) M_w(\delta) S_{in}$ and the matrix T would have a much simpler form

$$
T = \begin{bmatrix} 1 & [\cos(2\theta_1)] & [\sin(2\theta_1)\cos(\delta_1)] & [\sin(2\theta_1)\sin(\delta_1)] \\ 1 & [\cos(2\theta_2)] & [\sin(2\theta_2)\cos(\delta_1)] & [\sin(2\theta_2)\sin(\delta_1)] \\ 1 & [\cos(2\theta_1)] & [\sin(2\theta_1)\cos(\delta_2)] & [\sin(2\theta_1)\sin(\delta_2)] \\ 1 & [\cos(2\theta_2)] & [\sin(2\theta_2)\cos(\delta_2)] & [\sin(2\theta_2)\sin(\delta_2)] \end{bmatrix}. \tag{93}
$$

However, $det(T) \equiv 0$, and the Eq. 91 cannot be inverted to determine the Stokes vector. An additional polarizing element (retarder) is required as described to mix up the four

77

Stokes components such that an analyzer (polarizer) would bring them independently up in the total intensity, the measured quantity. A quarter-wave plate oriented at an angle ρ does the trick. However, ρ cannot be $0°$ or $90°$ (parallel to LCVR3) because f_2 or f_3 would be identically zero and $det(T) \equiv 0$. ρ cannot be $45°$ as well, since f_1 is zero and $det(T) \equiv 0$.

The optimization problem reduces now to maximizing the determinant $\Delta(\delta_1, \delta_2, \rho, \theta_1, \theta_2)$ of the matrix T given by Eq. 92 where the three functions f_1, f_2, and f_3 are given by Eq. 90.

The algebraic expression of the determinant

$$\Delta(\delta_1, \delta_2, \rho, \theta_1, \theta_2) = -8\sin^2(\frac{\delta_1 - \delta_2}{2})\cos(\theta_1 - \theta_2) \cdot \tag{94}$$
$$\sin^2(\theta_1 - \theta_2)\sin(\theta_1 + \theta_2 - 2\rho)\sin(4\rho)$$

can be separated in two functions of independent variables

$$F_1(\delta_1, \delta_2) = \sin^2(\frac{\delta_1 - \delta_2}{2}) \tag{95}$$
$$F_2(\rho, \theta_1, \theta_2) = \cos(\theta_1 - \theta_2)\sin^2(\theta_1 - \theta_2)\sin(\theta_1 + \theta_2 - 2\rho)\sin(4\rho) \tag{96}$$

The maximum value of F_1, which is 1, is obtained for any combination $\delta_1 = \delta_2 \pm \pi$. To obtain the maximum value of F_2, 0.384876, any combination of $\theta_1 = \pm 4°, \pm 5°, \pm 6°$, $\theta_2 = \theta_1 \pm 55°$, and $\rho = \pm 22.5° \pm 45°$ can be used.

There are many solutions for this maximization problem. If we consider the four lines of the matrix T given by Eq. 92 as representing the vertices of a tetrahedron inscribed in a sphere of radius 1, the function Δ, the determinant of the matrix T, is equal to the volume of the tetrahedron. The maximum volume corresponds to a regular tetrahedron, for any

78

orientation of the tetrahedron inside the sphere. This degree of freedom in the orientation of the tetrahedron provides for an infinite number of solutions. From a practical point of view, a step of $0.5°$ in the variation of the 5 variables is reasonable enough, making the number of solutions to be finite.

Here is an example of a set of retardations and orientations for the polarizing elements that provide for the maximum value of the function Δ of 3.079: $\theta_1 = 5°$, $\theta_2 = 130°$, $\rho = 22.5°$, $\delta_1 = 0°$, and $\delta_2 = 180°$. This completely determines the configuration of the Stokes analyzer.

2.2.5. Calibration

To account for inherent errors introduced by non-ideal optical elements or misalignment, an experimental calibration has to be performed.

The previous analysis of the two Stokes analyzers assumes that all the active components are perfectly aligned in a given coordinate system. Also, as mentioned before, the beamsplitter cube was assumed to be non-polarizing. However, any real beamsplitter acts, practically, as both partial polarizer and phase-shifter (retarder), both in transmission and in reflection. An ideal Mueller matrix for a beamsplitter cube that would describe these effects is[14]

$$
M_{\Psi,\Delta} = \begin{bmatrix}
1 & -\cos(2\Psi) & 0 & 0 \\
-\cos(2\Psi) & 1 & 0 & 0 \\
0 & 0 & \cos(\Delta)\sin(2\Psi) & \sin(\Delta)\sin(2\Psi) \\
0 & 0 & -\sin(\Delta)\sin(2\Psi) & \cos(\Delta)\sin(2\Psi)
\end{bmatrix}, \quad (97)
$$

79

where Ψ and Δ are the standard ellipsometric angles and are different for transmission and reflection. A more general matrix should be used to take into account any misalignment (rotation) of the cube.

The splitting ratio of the cube could be different than the ideal 50/50 such that the optical intensities incident on the detectors could be affected by different attenuation factors.

To account for all these issues, it is assumed here that each of the four measured quantities I_1, I_2, I_3, and I_4 depends on all four Stokes vector components:

$$
\begin{bmatrix} I_1 \\ I_2 \\ I_3 \\ I_4 \end{bmatrix} = \begin{bmatrix} a'_1 & a'_2 & a'_3 & a'_4 \\ b'_1 & b'_2 & b'_3 & b'_4 \\ c'_1 & c'_2 & c'_3 & c'_4 \\ d'_1 & d'_2 & d'_3 & d'_4 \end{bmatrix} \begin{bmatrix} I_0 \\ Q_0 \\ U_0 \\ V_0 \end{bmatrix} . \tag{98}
$$

Then, the Stokes vector is obtained by calculating the inverse matrix of this system which we will call M_{coeff}:

$$
\begin{bmatrix} I_0 \\ Q_0 \\ U_0 \\ V_0 \end{bmatrix} = M_{coeff} \begin{bmatrix} I_1 \\ I_2 \\ I_3 \\ I_4 \end{bmatrix} = \begin{bmatrix} a_1 & a_2 & a_3 & a_4 \\ b_1 & b_2 & b_3 & b_4 \\ c_1 & c_2 & c_3 & c_4 \\ d_1 & d_2 & d_3 & d_4 \end{bmatrix} \begin{bmatrix} I_1 \\ I_2 \\ I_3 \\ I_4 \end{bmatrix} . \tag{99}
$$

For example, rewriting the Equations 85-88 for the ideal case, M_{coeff} is given by:

80

$$M_{coeff}^{ideal} = \begin{bmatrix} 0 & 1 & 0 & 0 \\ 1 & -1 & 0 & 0 \\ 0 & 0 & 0 & 1/J_2(\delta_o) \\ 0 & 0 & 1/J_1(\delta_o) & 0 \end{bmatrix}. \tag{100}$$

M_{coeff} could be experimentally determined for four known input states of polarization (Stokes vectors). Eq. 99 provides basically a system of 16 equations with unknowns a_i,b_i,c_i and d_i ($i = 1..4$). M_{coeff} is obtained solving this system. However, using a number of inputs larger than 4, a better calibration can be obtained. By rotating two retarders (quarter-wave and half-wave plate) after a fixed polarizer, a good coverage of the whole Poincarè sphere can be achieved. The best calibration of the Stokes analyzer is obtained by fitting all the generated Stokes vectors, not only a limited set of four.

2.2.6. Polar decomposition and noise filtering

Polarimetric characteristics like depolarization, diattenuation and retardance, very important in optical media characterization, can be obtained from experimental Mueller matrices by polar decomposition.[114] The diattenuation quantizes the difference in transmission, while the retardance describes the phase shift between linear orthogonal polarizations. For certain materials that depolarize light isotropically, the Mueller matrix can be decomposed as a sum of non-depolarizing matrix and a totally depolarizing one

$M = M_J + M_D$ where

$$M_D = \begin{bmatrix} d & 0 & 0 & 0 \\ 0 & 0 & 0 & 0 \\ 0 & 0 & 0 & 0 \\ 0 & 0 & 0 & 0 \end{bmatrix}. \tag{101}$$

d is called depolarization coefficient and is calculated as

$$d = M_{11} - \sqrt{\frac{1}{3}\left[Tr\left(M^T M\right) - M_{11}^2\right]}. \tag{102}$$

The non-depolarizing matrix M_T can be directly derived from a Jones matrix T through the following transformation

$$M_T = A\left(T \otimes \overline{T}\right) A^{-1}, \tag{103}$$

where

$$A = \begin{bmatrix} 1 & 0 & 0 & 1 \\ 1 & 0 & 0 & -1 \\ 0 & 1 & 1 & 0 \\ 0 & i & -i & 0 \end{bmatrix}, \tag{104}$$

$\otimes$ denotes the Kronecker product, and $\overline{T}$ is the complex conjugate of T. The Jones matrix T, that is obtained solving Eq. 103, can be decomposed by polar decomposition in a Hermitian matrix T_P associated with an elliptical partial polarizer and a unitary matrix T_R associated with a pure elliptical retarder ($T = T_P T_R$). The retardance δ and the diattenuation $\mathcal{D}$ can be extracted as follows:

$$\delta = 2arcos\left[\frac{\left|TrT + \frac{detT}{|detT|}TrTJ^*\right|}{2\sqrt{Tr\left(T^*T\right) + 2\left|detT\right|}}\right], \tag{105}$$

82

where T^* is the transpose complex conjugate of T, and

$$\mathcal{D} = \frac{P_x^2 - P_y^2}{P_x^2 + P_y^2},\tag{106}$$

where $P_x^2 = T_{max}$ and $P_y^2 = T_{min}$ given by

$$T_{max,min} = \frac{1}{2}\left\{Tr\left(T^*T\right) \pm \sqrt{\left[Tr\left(T^*T\right)\right]^2 - 4\left|detT\right|^2}\right\}.\tag{107}$$

The random noise associated with experimental Mueller matrices can be filtered out given that the noise is small with respect to the signal. Using the Pauli matrices a Hermitian matrix H can be constructed as

$$H = \frac{1}{2}\sum_{i=0}^{3}\sum_{j=0}^{3} M_{i,j}\sigma_i \otimes \sigma_j.\tag{108}$$

The eigenvalues λ_k and the eigenvectors w_k are calculated for the matrix H. If the largest eigenvalue $\lambda_0 \approx TrH = 2M_{1,1}$ and the other 3 eigenvalues are close to 0, then the noise is considered to be filtered out by removing λ_k with $k = 1, 2, 3$. The matrix H_J is constructed by $H_J = \lambda_0 w_k w_k^*$. The Eq. 103 can be rearranged as

$$F_T = A^{-1}M_T A = T \otimes \overline{T}\tag{109}$$

and F_T can be obtained from H_T using $F_{T(i,k)(j,l)} = H_{T(i,j)(k,l)}$ where $(i,j) = 2i + j$. The Eq. 109 provides now the filtered Mueller matrix M_T.

Using the procedure described above, implemented in a Mathematica program, the overall error of the experimental Mueller matrices was reduced up to 10 times.

2.2.7. Optimization of Mueller polarimeters

There are still many practical questions to be answered related to the measurement of the Mueller matrix. Typically, a Mueller matrix polarimeter is composed of a generator of the state of polarization and an analyzer that measures the output state of polarization, as described above. For ideal Stokes generators and Stokes analyzers there are no obvious problems in retrieving the experimental data. However, in practical situations, fluctuations are unavoidable in both the generation and the analysis process resulting in errors in the measured Mueller matrix. The problem of optimizing the Stokes generator, such that the influence of these fluctuations in the Mueller matrix measurement is minimized, is addressed in the following.

In a typical experiment, the input states of polarization $S_{in}^{(i)}$ are measured first, then the corresponding output states $S_{out}^{(i)}$ are measured when the sample is present. The Mueller matrix of the sample is subsequently calculated from

$$S_{out}^{(i)} = M S_{in}^{(i)} \tag{110}$$

assuming that the input Stokes vectors are constant during measurement. In practice this is obviously not the case because of the laser power variations during the measurement and of the limited reproducibility (fluctuations) of the generation process. Ideally, an additional Stokes analyzer should be used to measure simultaneously the input and the output Stokes vectors such that the Eq. 110 is rigorously applicable. However, this is not always a practical solution. A different approach is proposed here for minimizing the effects of the experimental errors on the calculated Mueller matrix elements. The goal is to answer the question: how should one choose the four input Stokes vectors such that

fluctuations in these vectors propagate with the smallest effect on the calculated Mueller matrix?

There are several examples in the literature for optimization procedures intended to promote noise immunity in Stokes analyzers.[102, 115–119] The common strategy is to minimize various figures of merit such as the inverse of the determinant of the measurement matrix. In practice, the configuration of the measurement system is chosen to maximize the determinant of the matrix that relates the Stokes vector to be determined to the four measured intensities. The optimization discussed here is based on the same mathematical principle, i.e. maximization of the determinant of the transformation matrix that linearly relates the measurement vector (four measured quantities) and the vector representing the four quantities to be calculated. The transformation matrix T is constructed by the four input Stokes vectors and is the same for the four systems of equations that have to be solved for complete determination of the Mueller matrix. We emphasize here that, in the following analysis, an ideal Stokes analyzer is considered, and this discussion addresses (1) the laser power fluctuation between the measurement of the input states (without the sample) and the measurement of the output states (with the sample), and (2) fluctuations in the Stokes vector generation process.

Any Stokes generator is based on a polarizer and at least one retarder. Various combinations can be used to generate all possible states of polarization: stationary polarizer and rotatable half and quarter wave plates, rotatable polarizer and one rotatable waveplate, rotatable polarizer and stationary variable retarder, stationary polarizer and two stationary variable retarders. Common to all these combinations is that two parameters

are available to adjust the generated state of polarization. Between these parameters and the general ellipsometric parameters, ellipticity and azimuth, there is a unique relationship. Working with either set of two variables for describing the state of polarization does not reduce the generality of this analysis. For practical considerations, the combination: rotatable polarizer with its orientation specified by θ and stationary variable retarder with the retardance specified by δ, is selected here. For complete measurement of a Mueller matrix, at least four independent incident states of polarization are required ($i = 1 - 4$):

$$
S_{in}^{(i)} = \begin{bmatrix} I_{in}^{(i)} \\ Q_{in}^{(i)} \\ U_{in}^{(i)} \\ V_{in}^{(i)} \end{bmatrix} = \begin{bmatrix} 1 \\ \cos(2\theta_i) \\ \sin(2\theta_i)\cos(\delta_i) \\ -\sin(2\theta_i)\sin(\delta_i) \end{bmatrix}. \tag{111}
$$

In Eq. 111, θ is the orientation of the polarizer given in the coordinate system of the retarder. After the light interacts with a system that transforms the state of polarization (polarizer, retarder, scattering or optically active medium, etc.), the outgoing Stokes vector is given by Eq. 110. To determine all sixteen elements of the Mueller matrix M, one needs sixteen equations corresponding to four input Stokes vectors $S_{in}^{(i)}$ ($i = 1 - 4$). Eq. 110 can be rewritten as follows $(S_{out}^{(i)})_j = \sum_{k=1}^{4} T_{ik} M_{jk}$, where the transfer matrix T is defined as:

$$
T = \begin{bmatrix} I_{in}^{(1)} & Q_{in}^{(1)} & U_{in}^{(1)} & V_{in}^{(1)} \\ I_{in}^{(2)} & Q_{in}^{(2)} & U_{in}^{(2)} & V_{in}^{(2)} \\ I_{in}^{(3)} & Q_{in}^{(3)} & U_{in}^{(3)} & V_{in}^{(3)} \\ I_{in}^{(4)} & Q_{in}^{(4)} & U_{in}^{(4)} & V_{in}^{(4)} \end{bmatrix}. \tag{112}
$$

The procedure requires the matrix T to be invertible.

86

If the power of the incident beam does not fluctuate significantly from one polarization state to another, one can safely assume that $I_{in}^{(1)} = I_{in}^{(2)} = I_{in}^{(3)} = I_{in}^{(4)} = I_{in}$. Under these circumstances we can write $T = I_{in}Tr$, where the reduced matrix Tr, involving normalized Stokes vector components is

$$Tr = \begin{bmatrix} 1 & q_{in}^{(1)} & u_{in}^{(1)} & v_{in}^{(1)} \\ 1 & q_{in}^{(2)} & u_{in}^{(2)} & v_{in}^{(2)} \\ 1 & q_{in}^{(3)} & u_{in}^{(3)} & v_{in}^{(3)} \\ 1 & q_{in}^{(4)} & u_{in}^{(4)} & v_{in}^{(4)} \end{bmatrix}. \tag{113}$$

In the following, maximization of the determinant of the transfer matrix, should be done for the matrix T as given by Eq. 112. However, the intensity of the input states I_{in} is just a multiplicative factor for the matrix Tr and maximizing the determinant of the matrix T implies the maximization of I_{in} as well. This is an obvious requirement meaning that the accuracy of a measurement is improved when using signals way above the noise level. Even if the intensity I_{in} is explicitly separated from the optimization procedure, the errors due to the laser power fluctuations still have to be considered as noise in the first column of the matrix Tr.

An obvious condition for $det(Tr)$ to be non-zero is to not have all $q_{in}^{(i)}$ equal. The same is true for $u_{in}^{(i)}$, and $v_{in}^{(i)}$. This is equivalent with requiring that not all four input states have the same ellipticity, namely the same v_{in}, or the same orientation of the ellipse. For example, $q_{in}^{(i)} = 0$ for $(i = 1 - 4)$, corresponding to four ellipses with their axes along $45°$ and $-45°$, will not fulfill this condition, resulting in $det(Tr) = 0$. This means that one fixed polarizer and one variable retarder with fixed orientation that would generate only a class of ellipses having the same orientation is not sufficient for a complete determination

87

of the Mueller matrix. Two variable retarders are required in order to generate four

independent input states of polarization, allowing therefore Tr to be invertible.

Using the generated input state of polarization given by Eq. 111, the general form of

the matrix Tr is

$$Tr = \begin{bmatrix} 1 & [\cos(2\theta_1)] & [\sin(2\theta_1)\cos(\delta_1)] & [-\sin(2\theta_1)\sin(\delta_1)] \\ 1 & [\cos(2\theta_2)] & [\sin(2\theta_2)\cos(\delta_2)] & [-\sin(2\theta_2)\sin(\delta_2)] \\ 1 & [\cos(2\theta_3)] & [\sin(2\theta_3)\cos(\delta_3)] & [-\sin(2\theta_3)\sin(\delta_3)] \\ 1 & [\cos(2\theta_4)] & [\sin(2\theta_4)\cos(\delta_4)] & [-\sin(2\theta_4)\sin(\delta_4)] \end{bmatrix}. \quad (114)$$

As mentioned before, $det(Tr) = 0$ if all $q_{in}^{(i)}$ are equal. The condition $\theta_1 = \theta_2 = \theta_3 = \theta_4$

corresponds to a fixed polarizer and only one variable retarder. Also, $\delta_1 = \delta_2 = \delta_3 = \delta_4$ gives $det(Tr) = 0$, corresponding to a polarization rotator followed by a stationary

constant retarder. These configurations cannot be used for complete determination of the

Mueller matrix.

2.2.7.1. Geometrical representation

The four Stokes vectors that form the matrix Tr can be represented on the Poincarè

sphere[10] as the vertices of a tetrahedron as shown in Fig. 2.18. The volume of this

tetrahedron is equal to $det(Tr)$.

Fluctuations of the retardances introduced by the variable retarders bring in a certain

degree of uncertainty in the position of the four input states of polarization on the Poincarè

sphere. Assuming that the fluctuations are small, we can represent these uncertainties

as small surfaces around each of the four points on the sphere as shown in Fig. 2.18.

This results in an uncertainty ΔV of the volume V of the tetrahedron equivalent to an

88

uncertainty in $det(Tr)$ which, in turn, controls the errors in calculating the Mueller matrix elements starting from the Eq. 110. Intuitively, following the visual representation given in Fig. 2.18, these errors can be minimized if the uncertainty ΔV in the volume is small compared with the volume V.
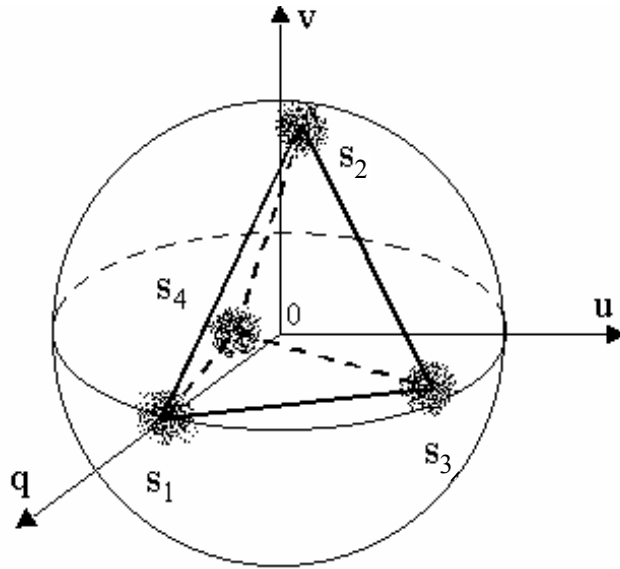
Figure 2.18. The Poincare sphere representing the four input Stokes vectors that construct the matrix Tr. The four points on the sphere are the vertices of a regular tetrahedron.

Assuming that the uncertainty area around a point on the sphere does not depend on the location of the point on the sphere, the ratio $\Delta V/V$ can be minimized by maximizing V, having the 4 points on the sphere as far apart as possible. This gives an intuitive explanation for the requirement to maximize $det(Tr)$ in order to reduce the effect of noise on the calculated Mueller matrix elements. In practical situations however, the assumption of equal uncertainty around any point on the Poincarè sphere might not always be valid. For example, for a liquid crystal variable retarder (LCVR) the dependence of

89

the retardance introduced as function of the applied voltage has a negative exponential shape. The same fluctuation of the voltage brings in a large fluctuation of the retardance for small voltages, as compared to a much smaller fluctuation of the retardance for large voltages. For this reason, it is preferably to choose the four input states that maximize $det(Tr)$, but in the same time correspond to large applied voltages on the LCVR's to minimize the fluctuation that generates ΔV.

It is well known that the maximum volume of a tetrahedron inscribed in a sphere corresponds to a regular tetrahedron. Since any orientation of the tetrahedron maintains its volume $V = det(Tr)$, the problem of finding the set of input states that maximizes $det(Tr)$ has an infinite number of solutions. The following is an example of using this geometrical representation in the maximization process. Selecting one state of polarization and imposing only one limitation on the second state completely determines the tetrahedron with maximum volume. The choice of the first state is arbitrary and can be particularized only by specific constraints on the actual experimental setup. However, the procedure of determining the four input states is the following: the first state is chosen (either arbitrarily or imposed by practical considerations), an additional choice is made for the second state, and then, the other two states are determined such that $det(Tr)$ is maximized. The additional choice for the second Stokes vector cannot be completely arbitrary; it must allow the geometrical distance between S_1 and S_2 in the Poincarè sphere representation to be $4/\sqrt{6}$, which is the size of a regular tetrahedron inscribed in a sphere of radius 1.

Since the orientation of the tetrahedron is not relevant for maximizing its volume, we can chose S_1 on the q axis, as well as S_2 in the $(q0v)$ plane. This means $\theta_1 = 0$, and $\delta_2 = 90°$. δ_1 can take any value and for practical considerations we can choose it equal to δ_2. For a regular tetrahedron, if one vertex is on the q axis, the other three have the same q value. This is equivalent to $\cos(2\theta_2) = \cos(2\theta_3) = \cos(2\theta_4)$, or $\theta_2 = \theta_3 = \theta_4$, since θ represents the orientation of a polarizer, and θ and $\theta + \pi$ correspond to the same orientation of the polarizer. With these simplifications the Eq. 114 becomes

$$Tr = \begin{bmatrix} 1 & 1 & 0 & 0 \\ 1 & \cos(2\theta) & 0 & -\sin(2\theta) \\ 1 & \cos(2\theta) & \sin(2\theta)\cos(\delta_3) & -\sin(2\theta)\sin(\delta_3) \\ 1 & \cos(2\theta) & \sin(2\theta)\cos(\delta_4) & -\sin(2\theta)\sin(\delta_4) \end{bmatrix}, \tag{115}$$

and the determinant of Tr is given by

$$V = \det(Tr) = -2\sin^2(\theta)\sin^2(2\theta)[\cos(\delta_3) - \cos(\delta_4) + \sin(\delta_3 - \delta_4)]. \tag{116}$$

The number of variables in Eq. 114 is reduced from eight to three, with a minimum number of choices, therefore, simplifying the expression of $det(Tr)$ and allowing its graphical representation. This function is separable in $f_1(\theta) = [\sin(\theta)\sin(2\theta)]^2$ presented in Fig. 2.19 a, and $f_2(\delta_3, \delta_4) = \cos(\delta_3) - \cos(\delta_4) + \sin(\delta_3 - \delta_4)$ shown in Fig. 2.19 b as a surface plot for values of δ_3 and δ_4 between 0 and 2π. The maximum absolute value of $det(Tr)$ is 3.0789. One can see that $f_1(\theta)$ has a maximum value of 0.592 for $\theta = 55°$, and $f_2(\delta_3, \delta_4)$ has the maximum value of 2.598 for $\delta_3 = 330°$ and $\delta_4 = 210°$. This is one of the most intuitive configurations. Any other orientation of the tetrahedron would maximize $det(Tr)$ as long as the tetrahedron is regular. Table 2.1 shows the four sates

of polarization given the values of θ and δ as obtained in this example. The four input states of polarization corresponding to these values of θ and δ are shown in Fig. 2.20 a in the ellipse representation and in Fig. 2.20 b on the Poincarè sphere.

a)   b)
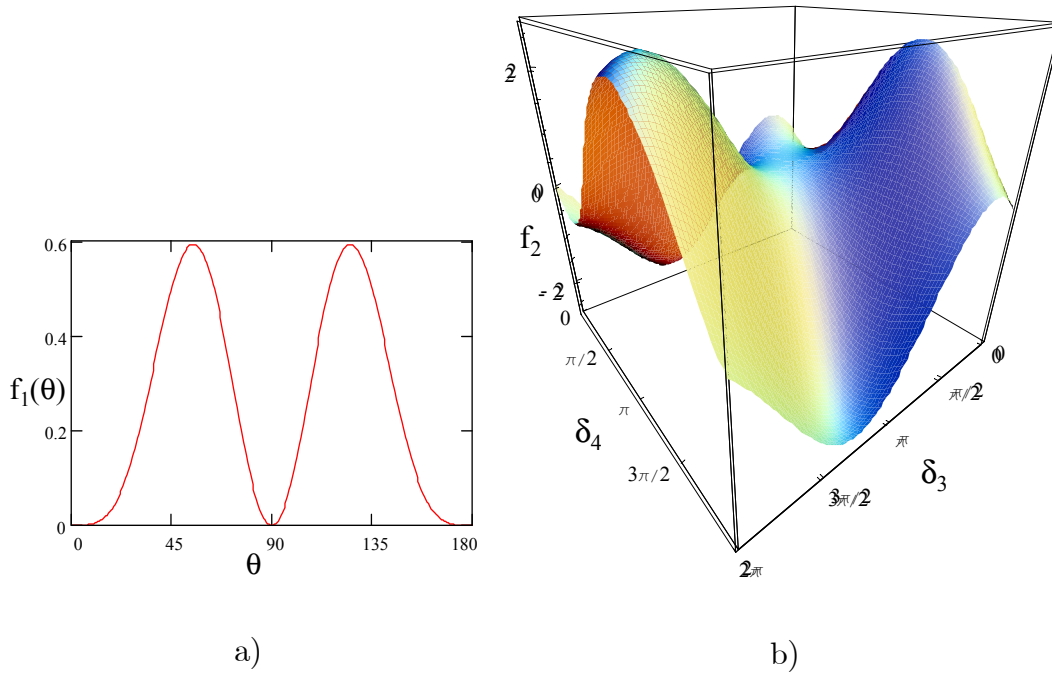
Figure 2.19. a) Plot of $f_1(\theta)$; b) plot of f_2 as function of δ_3 and δ_4.

Table 2.1. The four input states of polarization corresponding to our first example of optimum input configuration, given the orientation θ of the polarizer and the retardance δ of the variable retarder in the generation unit.

state #	$\theta(°)$	$\delta(°)$	q	u	v
1	0	90	1	0	0
2	55	90	-0.342	0	-0.940
3	55	330	-0.342	0.814	0.470
4	55	210	-0.342	-0.814	0.470

Figure 2.20. The four input states of polarization corresponding to our example of the optimum choice: a) in ellipse representation, and b) on the Poincare sphere.
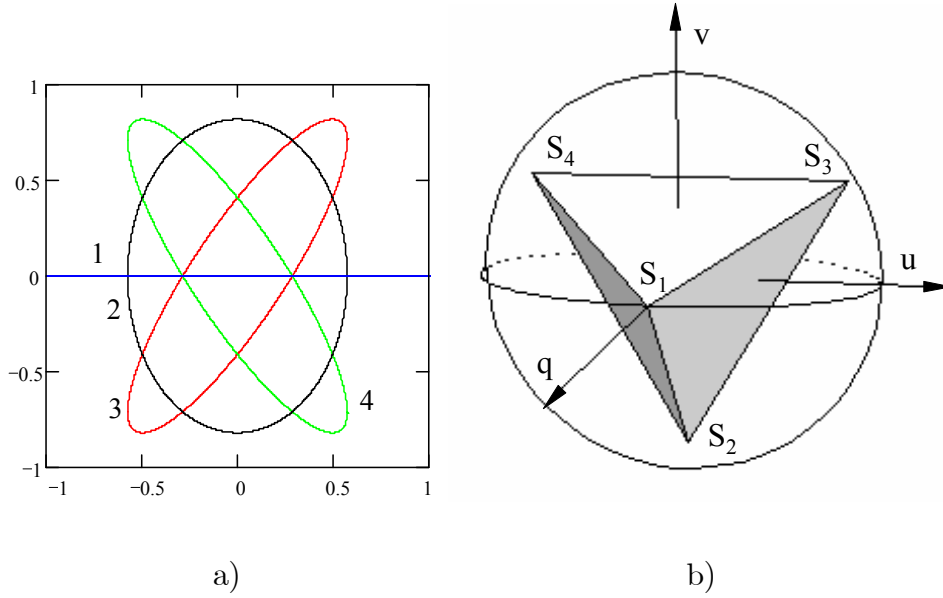
The surface represented in Fig. 2.19 b has four extrema, two maxima and two minima, but actually, only two of them are extrema for both variables in the interval $0 - 2\pi$ for θ and δ. Switching between δ_3 and δ_4 will change only the sign of f_2 but not the magnitude. The two pairs (δ_3, δ_4) given by $(210°, 330°)$ and $(330°, 210°)$ correspond geometrically to two orientations of the tetrahedron, one with one vertex in the positive v direction and two vertices in the negative v direction, and the second one, the other way around. The condition that S_2 is in the $(q0v)$ plane still allows S_2 to be placed in two positions on the Poincarè sphere, with positive or negative v. Due to the periodic nature of the trigonometric functions in f_2, enlarging the interval for θ and δ would just repeat the surface shown in Fig. 2.19 b. However, the two apparent extrema at (δ_3, δ_4) given by $(0°, 210°)$ and $(210°, 0°)$ would not be extrema anymore, the closest extrema being at $(-30°, 210°)$ and $(210°, -30°)$, which are equivalent to the ones discussed.

93

In order to experimentally confirm the validity of the procedure for choosing the four optimum input states of polarization, the Mueller matrix of a retarder was measured for different groups of four input states. The retarder, a quarter-wave plate for 532nm, was rotated 180° in steps of 2° around the normally incident laser beam. Nine different groups of four input states of polarization were used for this analysis. To evaluate the quality of the measured Mueller matrix, the absolute difference between the measured and the theoretical matrix element was calculated for each matrix element. An average error was calculated for each matrix element as the average of these absolute differences for all positions of the tested waveplate, and is shown in Fig. 2.21. This error represents the area between the theoretical and the experimental curve for each matrix element, normalized to the number of measurements (90 positions of the waveplate). The average of the errors for all matrix elements was calculated as a measure of the global goodness of the experimental Mueller matrix. Since the maximum value of any normalized Mueller matrix element is 1, this average error is expressed in percent as relative to unity.
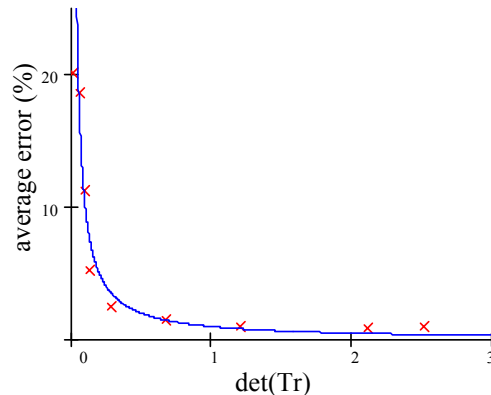

Figure 2.21. Average error of the measured Mueller matrix as function of $det(Tr)$.

As expected, the average error of the Mueller matrix decreases when increasing the value of $det(Tr)$, as it is shown in Fig. 2.21. The error increases to infinity (impossibility of measuring the Mueller matrix) as the determinant decreases to 0. The continuous line in Fig. 2.21 corresponds to $1/det(Tr)$; it is a reasonable good fit of the experimental points, confirming the validity of this procedure.

2.2.7.3. Practical considerations

As mentioned before, for complete determination of the Mueller matrix one needs a Stokes vector generator composed of one stationary polarizer and two variable retarders, because only one retarder cannot allow the matrix T to be invertible and the Eq. 110 cannot be solved. In the geometrical representation of Fig. 2.18, this requirement means that the four points representing the four input polarization states cannot be in one plane, because the volume of the tetrahedron reduces to zero. One ideal variable retarder preceded by a fixed polarizer can only generate ellipses with the same orientation that correspond to a vertical circle on the sphere. It is worth mentioning that, in practice, a variable retarder could also slightly rotate the ellipse. Different rotations for different ellipses could be enough to make the matrix T invertible. As seen in Fig. 2.21, given a certain value of the acceptable error in the experimental Mueller matrix, the four input states can be chosen such that $det(Tr)$ is quite far from the maximum, optimum value.

This analysis allows the estimation of the expected error in measuring the Mueller matrix given a specific setup. Also, once an acceptable experimental uncertainty is imposed, one can use this procedure to simplify the experimental setup.

95

In certain experiments, various restrictions do not allow all the desired input polarization states to be generated. For example, if LCVR's are used for generation of input states but the phenomena investigated have a short time scale, then the liquid crystal cells have to allow fast switching among the desired retardances. The switching time is directly related to the phase variation (proportional to the square of the phase variation[120] at large voltage). This limits the interval of the retardances that can be introduced by that cell, as well as the possible value of $det(Tr)$. Fig. 2.22 shows an example of four input states that give $det(Tr) = 0.5$, still allowing a decent 2% overall error, but reducing the span of the retardances that have to be generated. Table 2.2 gives the values of θ, δ and the normalized Stokes parameters for these four input states of polarization. The states 2 and 3 differ only through the handiness (sign of v), otherwise having the same ellipse.

Table 2.2. The values of θ, δ and the normalized Stokes parameters for the four input states of polarization corresponding to a reduced span of retardances.

state #	$\theta(°)$	$\delta(°)$	q	u	v
1	40	0	0.174	0.985	0
2	40	-46.25	0.174	0.681	0.711
3	40	46.25	0.174	0.681	-0.711
4	85	0	-0.985	0.174	0

Since the largest phase shift requires the longest switching time, it is preferable to reduce both spans at about the same value. For the optimum choice, θ varies 55° (corresponding to 110° phase shift on the first LCVR) and δ varies 240°. For the example given above, the variation for θ is reduced to 45° (90° phase shift), and that for δ is reduced to

96

92.5°. This represents a reduction of the initial span with 18.2% and 61.5%, respectively. As a result the switching time is reduced by a factor of 1.5 - first LCVR and 6.7 - second LCVR, allowing a significant increase of the speed in measuring the Mueller matrix. Reducing the switching time is of outmost importance in real-time imaging applications, as well as in biomedical applications that require following fast structural changes.
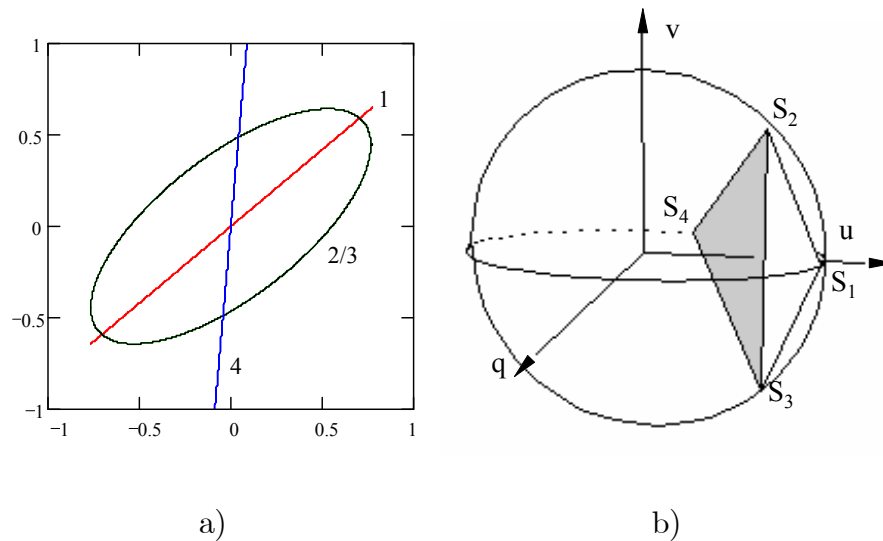
Figure 2.22. Choice of four input states with reduced span of introduced retardances: a) in ellipse representation, and b) on Poincare sphere.

It is also suggested here that only one variable retarder can be used for complete measurement of the Mueller matrix if both the ellipticity and the orientation of the input states are varied, as is the case of a real LCVR.

Given a specific setup, the analysis presented here provides an estimation of the expected error in measuring the Mueller matrix. When a certain value is set to be acceptable for the experimental uncertainty, this procedure can be used to simplify the experiment.

CHAPTER 3

POLARIZED LIGHT SCATTERING APPLICATIONS

The measurement techniques introduced previously are used in this Chapter for analyzing multiple scattering effects in random media. The polarimetric signatures of different particulate systems are related to their structural properties and to the size distribution, shape, orientation, birefringent or dichroic properties of the particles. Various scattering regimes and different geometries are discussed for applications relevant to the biomedical field, material science, and remote sensing.

The importance of polarized light scattering was demonstrated by the numerous applications reviewed in Section 1.5. Here, the polarimetric properties of random media are analyzed in terms of various anisotropies of either the global scattering system or the individual scattering centers.

An extreme case of asymmetric particles is represented by the particles with high aspect ratio, i.e. infinitely long cylinders. Bohren and Huffman[12] give an expression for the Mueller matrix for single scattering on a normally illuminated infinite cylinder

$$
M = \begin{pmatrix}
M_{11} & M_{12} & 0 & 0 \\
M_{12} & M_{11} & 0 & 0 \\
0 & 0 & M_{33} & M_{34} \\
0 & 0 & -M_{34} & M_{33}
\end{pmatrix}, \tag{117}
$$

98

which has the same form as that of a sphere. There are however differences between scattering on a sphere and on a normally illuminated cylinder, and it is worth noting that in the forward or the backward direction M_{12} does not necessarily vanish for a cylinder, but it is identically zero for a sphere. The consequence is that unpolarized light normally incident on a cylinder will be partially polarized in forward direction.[12] By rotating an ensemble of partially oriented cylinders that are normally illuminated, we analyze in this Section how this polarizing effect is also affecting other Mueller matrix elements.

The complex index of refraction of a medium is polarization dependent. The four possible effects are: linear birefringence, linear dichroism, circular birefringence and circular dichroism. Based on characteristics related to both the particle and the structure of the system, van de Hulst[9] discusses, in Chapters 5.4 and 19.4, interesting effects derived from particular cases of optical anisotropy. A few of them are reviewed in the following.

Optical anisotropy can be generated either by shape (form anisotropy) of the particle of homogeneous material, or by the internal structure of the scatterer. The structural anisotropy of a system of particles must also be considered. For example, linear birefringence can be produced by elongated particles of a homogeneous material having some degree of alignment (structural anisotropy), or by spheres of a substance that is itself birefringent. For linear dichroism also, the particles do not have to be dichroic themselves. If the material is isotropic but absorbing and the elongated particles are partially oriented, then the system presents an effective linear dichroism. Van de Hulst[9] shows that linear birefringence and dichroism occur only if both the following conditions are fulfilled: a) the particles are anisotropic due to either their form or their structure, and b) the

99

particles show preferred orientation in space. Random orientation cannot produce linear birefringence.

In the limit of small optical anisotropies, specific matrix elements are dominated by particular optical effects; circular dichroism - m_{41} and m_{14}, circular birefringence - m_{23} and m_{32}, linear dichroism - m_{12}, m_{13}, m_{21}, m_{31}, or linear birefringence - m_{24}, m_{34}, m_{42}, m_{43}. When the anisotropies are large, most of the matrix elements are superposition of different effects.[121] Comprehensive target identification procedures and medical investigations based on Mueller matrices must take into account all matrix elements.

The new results that will be presented in the following Sections include: depolarization effects in single scattering, polarizing effects and form birefringence for ensembles of partially aligned cylindrical fibers, depolarization in multiple scattering as function of the size and the shape of the particles, and of the input polarization, depolarization properties of multiply scattering optically active media, and of optically dense media.

3.1. Scattering matrix of distributions of spheres

The polarimetric properties of ensembles of spheres are analyzed here with the purpose of retrieving the size distribution.

A considerable number of reports exist in the literature which deal with experiments and theoretical calculations of light scattering from spherical particles.[122] For most of the practical applications in biology, material science or remote sensing however, monodisperse ensembles of spherical particles are just idealized representations. On the other hand, in the case of nonspherical particles, exact calculations for the single scattering problem can

100

be performed for a small number of regular geometrical shapes and intensive numerical calculations are usually implemented to approximate the scattering features for particles with more complex shapes or for ensembles of such particles.[123]

Experimental results are presented here for the scattering matrix of ensembles of spheres. An Atomizer from TSI Inc. was used to generate a spray of water droplets. Measurements were also performed on solutions of fructose and galactose and the results are shown in Fig. 3.1. These scattering matrices have all the characteristics for single scattering on ensembles of spheres as predicted by Mie theory. The block off diagonal elements m_{13}, m_{14}, m_{23}, m_{24}, m_{31}, m_{32}, m_{41} and m_{42} are all zero. m_{12} and m_{21} are equal, as well as m_{33} and m_{44}. m_{34} and m_{43} have the same magnitude and opposite signs. m_{22} is unity for all scattering angles, indicating spherical particles.
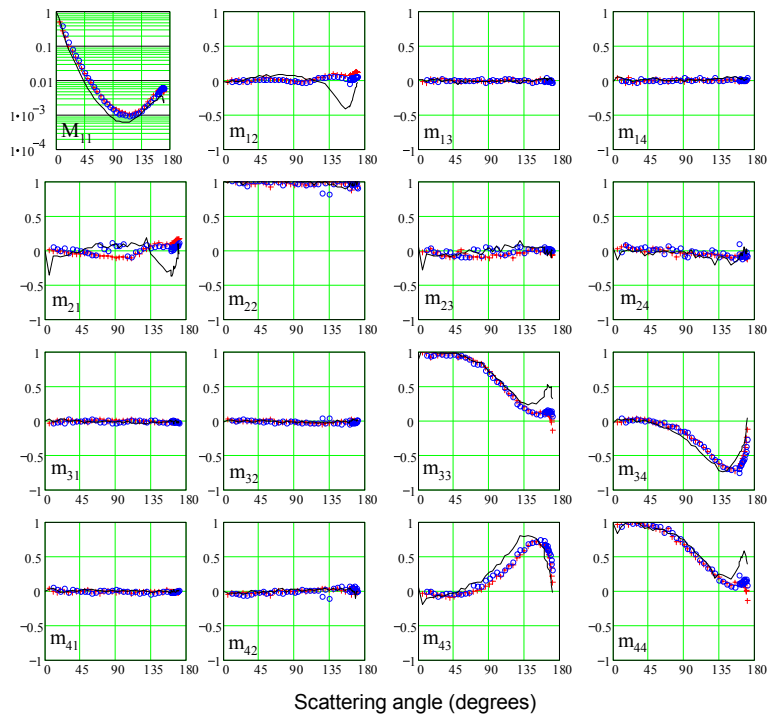

Figure 3.1. Scattering matrix for water droplets (line), fructose (+), and galactose (o).

The scattering matrix for a single sphere is described by the Mie theory for any radius of the sphere.[124] In practice, one performs scattering measurements on collections of scatterers and the common assumption is to consider them independent. This means that the light scattered from different particles does not interfere, and therefore, the Stokes vectors from individual particles scattered along a certain direction can be added (add intensities not fields). Subsequently, the scattering matrix of the ensemble can be obtained by integrating the individual scattering matrices for spheres of certain radius, each of them weighted with the probability to have spheres of that specific radius. Starting from the experimental scattering matrix, the size distribution can be determined quite accurately.
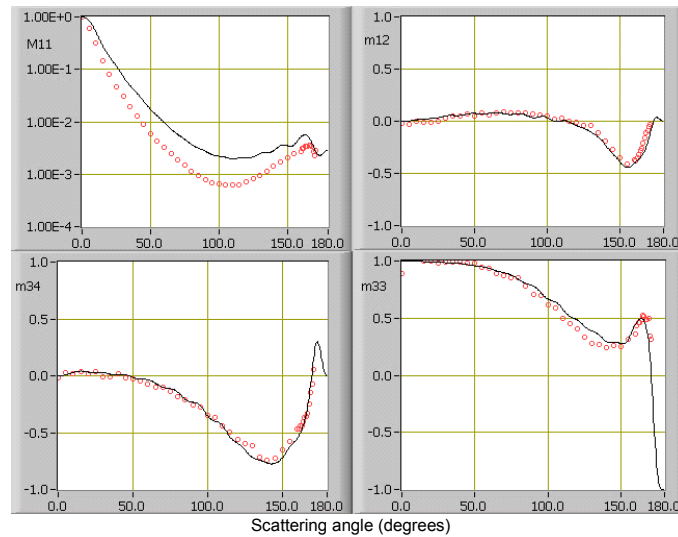

Figure 3.2. Mie calculation for a log-normal distribution of spheres to fit (continuous line) the experimental results (circles) in the relevant matrix elements from Fig. 3.1.

Fig. 3.2 shows an example of fitting the experimental results (circles) in the relevant matrix elements from Fig. 3.1 using Mie calculations for a log-normal distribution of

spheres (water droplets). The distribution is characterized by an average size of 100nm and a standard deviation of 400nm. Excellent agreement is shown in the matrix elements m_{12}, m_{34} and m_{33}.

It is worth mentioning here that the scattering matrix for a single sphere (or an ensemble of identical spheres) is a pure, non-depolarizing Mueller matrix. However, if the ensemble is polydisperse, even in the single scattering regime the scattering matrix of the ensemble exhibits depolarization effects, as shown in Fig. 3.3; the depolarization index (formula 5) is smaller that 4 for most of the scattering angles. A given input state of polarization is transformed along a certain direction in many different states of polarization by spheres with different radii. Each individual contribution is a pure state, however, a distribution of pure states is produced on a given direction of observation and the result is that a certain degree of polarization smaller that unity is actually measured. This effect has not been previously addressed.
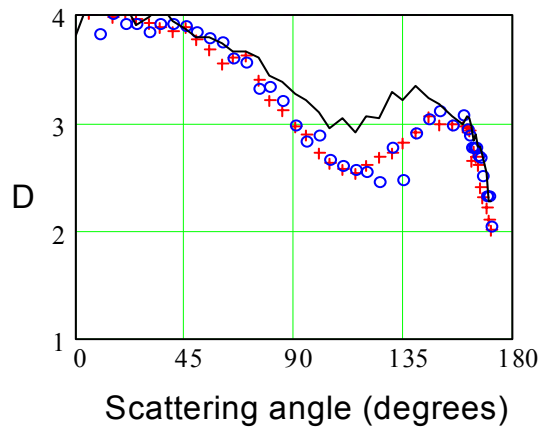

Figure 3.3. Depolarization index as function of the scattering angle.

103

Until now, it seemed to be generally accepted that depolarization effects can only be associated to multiple scattering. It is obvious from the analysis presented in this Section that depolarization can also be induced in single scattering on an ensemble of polydisperse spherical particles.

3.2. Forward scattering on cylindrical fibers

The polarization transfer through systems consisting of individual layers of partially aligned fibers with different degrees of alignment and packing fractions is analyzed in this Section. The analysis of this new scattering system permits to describe quantitatively the polarizing behavior observed for partially oriented cylinders.

In order to infer details of shape anisotropy, one can measure the polarization transfer function (Mueller matrix) associated with the specific scattering situation. Based on symmetries for ensembles of randomly oriented particles, the number of independent Mueller matrix elements can be reduced, while some of them can be shown to be identically zero.[9] However, not all these symmetries hold true for ensembles of nonspherical particles that have a partial orientation, and some of the off-diagonal elements may vary as function of the scatterers structure and orientation.

3.2.1. Polarizing effect

The effects of partial orientation at different packing fractions of long cylindrical objects was investigated experimentally. The scattering media consisted of synthetic

www.manaraa.com

cotton-like cylindrical fibers with diameter of about $15-20\mu m$. The index of refraction of the fibers is about 1.5 and the white appearance indicates negligible absorption. A microscopic image of the fibers is shown in Fig. 3.4. In compact media, having long cylinders closely packed together, implies that they are necessarily aligned perpendicular to the packing direction and a layer description is therefore appropriate. Within such a layer, the cylinders could be randomly oriented or partially aligned. The packing fraction of the fibers in a layer is given by the number of fibers within the unit area of the layer.

For the present measurements, a collimated He-Ne laser beam is spatially filtered and is normally incident on the tested media consisting of layers of fibers. The transversal cross-section of the beam (the illuminated area on the sample) has a diameter of $3mm$. Using apertures, an angularly narrow forward scattered beam is selected for measuring the output state of polarization.

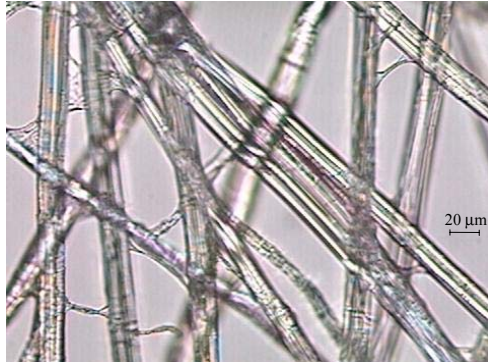Figure 3.4. Synthetic cotton-like cylindrical fibers having in average a diameter of 20μm.

As mentioned earlier, a layer description is appropriate for densely packed cylinders. Systematic investigations on the Mueller matrices corresponding to individual layers of partially oriented scatterers were performed to get insight into the general depolarization

105

behavior of such systems. Based on symmetry arguments, van der Hulst[9] showed that the Mueller matrix for single scattering on a cloud of particles with random orientations is generally symmetric about the diagonal, at least in magnitude (some elements might have different sign). However, for systems of particles showing certain degree of alignment, none of those symmetries hold true, and it is expected that most of the Mueller matrix elements are independent. Bickel and Stafford[15] describe measurements of the Mueller matrix for biological scatterers (viruses, bacteria) where m_{34} proved to be uniquely characteristic for scatterers that could not be distinguished in any other way. Also, measurements on ocean water performed by Kadyshevich[24] show that the scattering matrix is not necessarily symmetric about the diagonal. The Mueller matrix for single scattering on a normally illuminated infinite cylinder is symmetric about the diagonal, as given by Eq. 117, but for an ensemble of partially oriented cylinders some matrix elements are more sensitive than others to the packing fraction and the degree of alignment, as it will be seen here.

In this study, single layers of cylinders were rotated 360°, in steps of 10°, about the direction of the laser beam that is normal to the layer, while the Mueller matrix was recorded for each orientation of the structure. Fig. 3.5 illustrates typical single layers investigated in this experiment. A system of randomly oriented fibers is shown in Fig. 3.5 a, while Fig. 3.5 b and c display systems of partially oriented fibers with different packing fractions and degrees of alignment. The inset of each picture shows the 2D Fourier transform of the structure indicating also a preferential orientation of the fibers. Fig. 3.6 summarizes the variation with the angle of rotation of the Mueller matrix elements corresponding to the structure shown in Fig. 3.5 c.
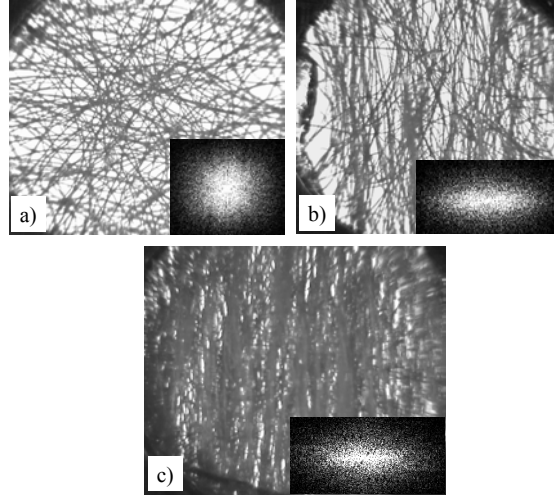
Figure 3.5. Typical samples with different degree of alignment and packing fractions. The insets show the corresponding Fourier transforms.

To quantify the relationship between structural anisotropy of the scattering layer and the corresponding features in the Mueller matrix, a *polarizing efficiency* is defined as the amplitude of the sinusoidal variation of the Mueller matrix elements while rotating the layers. Also, the *structure parameter* is determined as the ellipticity of the equal strength ellipse of the 2D Fourier transform (structure factor) of the structure. For randomly oriented fibers, the Fourier transform has circular symmetry, the structure parameter being unity. For partially oriented fibers on the other hand, the structure factor increases as the number of fibers aligned along a certain direction increases. In principle, for a good diffraction grating, the structure factor tends to infinity, while the polarizing efficiency has to saturate at 0.5 for matrix elements 23, 33 and 32, and at 1 for matrix elements 13 and 31.
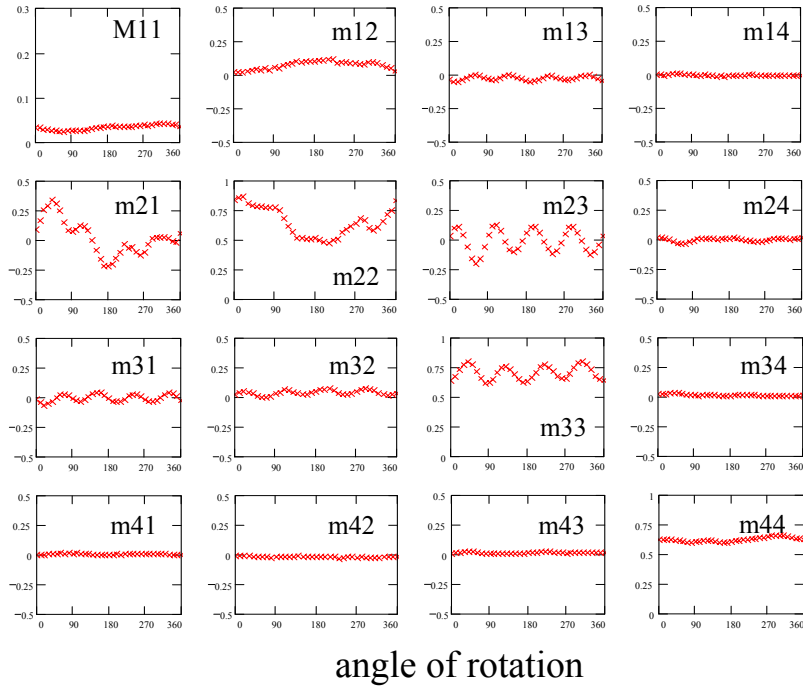
107

Figure 3.6. The Mueller matrix corresponding to the structure shown in Fig. 3.5 c, as function of the angle of rotation.

The polarizing efficiency was measured for six layers with different anisotropy levels and the results are summarized in Fig. 3.7 in a semilogarithmic scale. Different symbols indicate the matrix elements, and the dotted lines represent an exponential fit for each matrix element. One can notice a certain exponential increase of the polarizing efficiency with the structure parameter. The more fibers aligned (the larger the structure parameter), the better the polarizing efficiency. Also, the larger the number of aligned fibers in the structure (the smaller the transmission that is inversely proportional to the packing fraction), the better the polarizing efficiency. The polarizing efficiency depends on both the degree of alignment and the packing fraction as shown in Fig. 3.7. Note that the slopes of the exponential dependences are similar for the five matrix elements of interest but the magnitudes of the polarizing efficiencies are quite different. In the present series

108

of experiments, it was apparent that the matrix elements 12, 21 and 22 are most sensitive to the structural non-uniformities across the investigated area, while the matrix elements 23, 32, 33,13 and 31 are mostly sensitive to the degree of structural anisotropy (structure parameter) and the packing fraction (transmission). Structural non-uniformities are the result of local variations of the number density of the fibers. While rotating the sample, the investigated area might vary slightly at the edge, due to fibers coming in and out of the illuminated area. This seems to have effect only on the matrix elements 12, 21 and 22, without affecting however the structure parameter and the overall packing fraction.

a)   b)
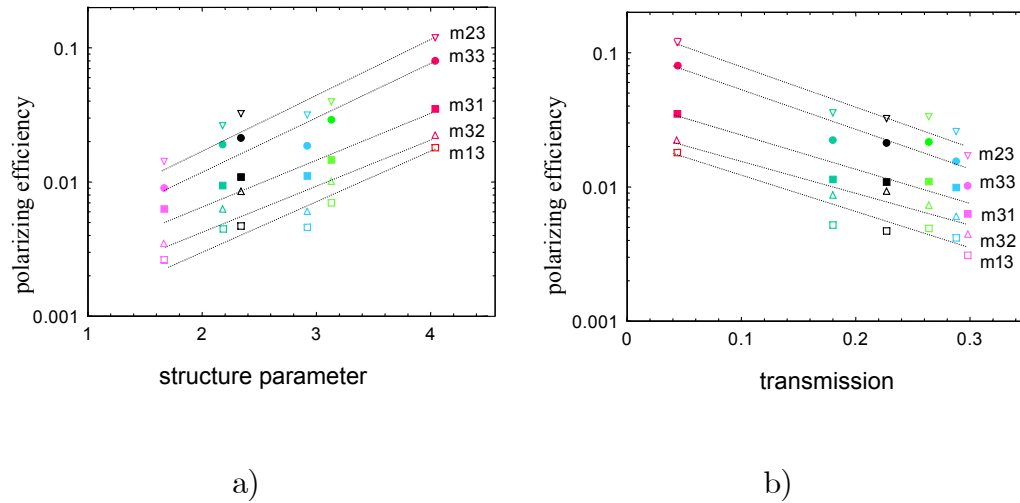
Figure 3.7. Dependence of polarization efficiency on a) the structure parameter and b) overall transmission. Different symbols represent the specific matrix elements as indicated.

It is worth mentioning that the optical anisotropy of the scatterers can manifest itself as linear or circular birefringence (the real part of the index of refraction) and linear or circular dichroism (the imaginary part of the index).[9] When these effects are small, they can be identified within specific Mueller matrix elements,[121] but when their

109

magnitude becomes considerable, each of them will affect groups of matrix elements, and the identification is more difficult. Van der Hulst[9] shows that nonspherical particles with net orientation should exhibit form (or sometimes called scattering) linear and/or circular dichroism and/or birefringence. Partial orientation is required in order to observe linear birefringence or dichroism, since random orientation averages to zero these effects. The Onuki-Doi theory[26] of form birefringence and dichroism, that is appropriate for systems where dipole scattering is the dominant mechanism, relates the birefringence and the dichroism to the structure factor. The Onuki-Doi theory has been developed for dilute systems, where the distance between scattering centers should be much larger than the size of the particles. This theory cannot be directly applied to our case for fibers with diameter much larger than the wavelength, where the major contribution to scattering field arises from interaction with particle boundary (Fraunhofer diffraction).[121] The polarizing effect observed in these experiments is generated by the shape anisotropy of the fibers in combination with their partial alignment. In the present case, due to a relatively low degree of alignment, the overall polarizing efficiency is small. This polarizing behavior is just one example of the effects that result from partial alignment of nonspherical particles and that can be explained through linear or circular birefringence or dichroism. The form birefringence effects are described below, as observed in a different experiment.

3.2.2. Form birefringence

When embedded in a flow, cylindrical particles, like alumina fibers shown in Fig. 3.8, and polyhedral alumina particles acquire necessarily a degree of alignment.

110

Figure 3.8. Alumina fibers.

The diameter of the fibers is $3\mu m$, and the aspect ratio has a very broad distribution, as seen in Fig. 3.8. The suspension of alumina fibers in water was flown through a rectangular cuvette. The cell, which was mounted on a rotation stage, was rotated normal to the incident laser beam and the Mueller matrix, shown in Fig. 3.9, was measured in transmission.
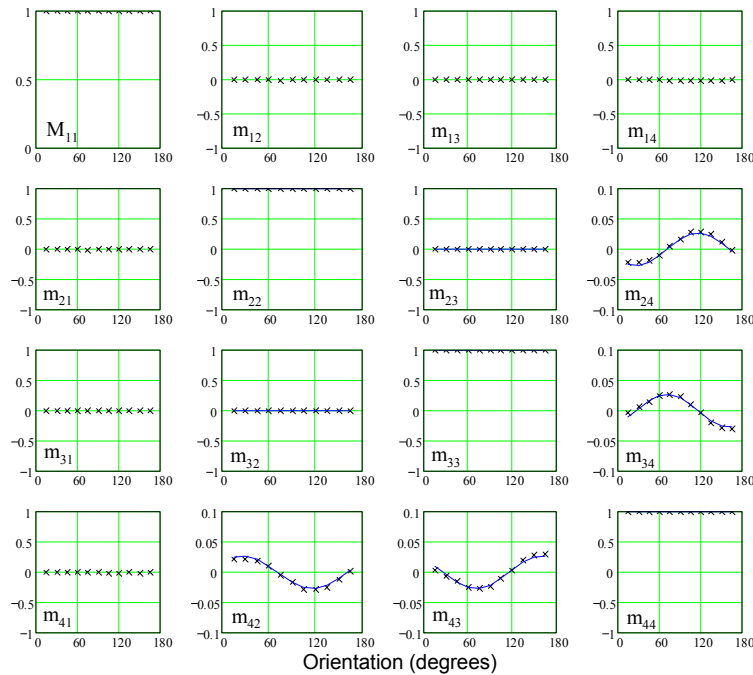

Figure 3.9. The Mueller matrix of a flowing suspension of alumina fibers as function of orientation of the cell.

111

The retardance values shown in Table 3.1 were obtained using the formalism described in Section 2.2.6. The diattenuation (formula 106) was negligible.

Table 3.1. Total retardance

material	total retardance
alumina fibers ($3\mu m$ diam.)	$(1.58 \pm 0.19)°$
alumina powder ($3.2\mu m$)	$(1.13 \pm 0.08)°$
silica spheres ($1.5\mu m$ diam.)	$(0.97 \pm 0.31)°$

The residual birefringence of the glass cuvette, measured with only water flowing through the system, was $\delta = (0.93 \pm 0.22)°$. Subtracting this residual birefringence from the values shown in Table 3.1, the form birefringence associated to the aligned particles is obtained as $0.65°$ for alumina fibers, $0.2°$ for polyhedral alumina, and $0.04°$ for silica spheres. As expected, the form birefringence for fibers is larger than for polyhedral particles, while for spheres can be neglected, being much smaller than the error.

The birefringent properties resulting from form anisotropy and partial alignment are related to structural characteristics of the random media in polymer science, biomedical applications, and remote sensing. The measurement of form birefringence and dichroism is a promising noninvasive investigation technique in such applications.

3.3. Multiple scattering

The polarimetric characteristics of multiple scattering media depend on the size and shape of the individual particles, as well as on the optical density and the structure of

112

the entire system. In remote sensing and for imaging in turbid media it is important to know what type of polarization is better preserved in propagation through optically dense media. In this Section, the polarization transfer in systems consisting of spherical, polyhedral and cylindrical particles is investigated.

3.3.1. Spheres

A systematic study of the Mueller matrix associated with particulate systems was performed[89] in transmission through media with various optical densities. A rectangular sample cell was divided in two triangular-base compartments as shown in Fig. 3.10. One compartment is filled with the scattering sample, while the other one is filled only with water. Translating the cuvette transversal to the beam, the physical thickness d of the sample along the laser beam direction can be changed between $80\mu m$ and $5mm$, modifying this way the optical density of the sample.
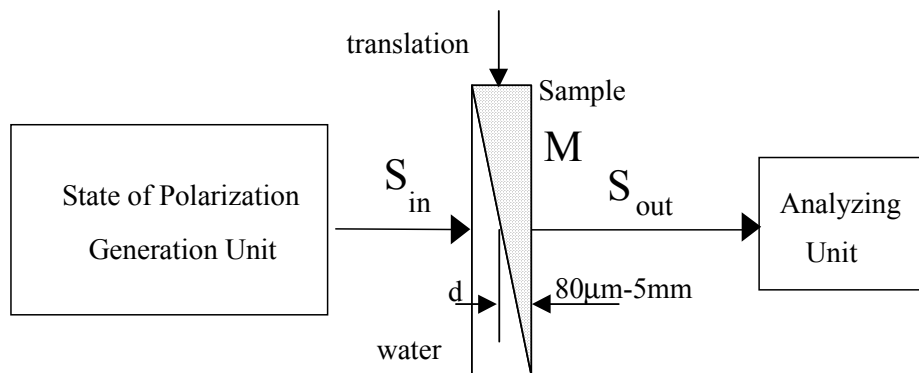

Figure 3.10. Experimental setup for measuring the Mueller matrix as function of optical density.

The polarization transfer was measured in transmission for spherical silica particles. Measurements were performed on suspensions of silica particles with three different sizes, $0.2\mu m$, $0.5\mu m$, and $1.0\mu m$ average diameter, but having the same volume fraction 3%. The anisotropy factor g as given by Mie theory for silica particles with $0.2\mu m$ (sample 1), $0.5\mu m$ (sample 2), and $1.0\mu m$ (sample 3) diameter is 0.303, 0.8207, and 0.938, respectively. The corresponding size parameters ka (where $k = 2\pi/\lambda$, $\lambda = 632.8nm$, and a is the radius of the particle) are 1.32, 3.3, and 6.6, respectively.

Fig. 3.11 presents the measured Mueller matrix for the three samples as function of the optical density defined as the ratio between the physical width of the sample d, and the transport mean free path l^* (l^* is the average distance after which the scattering direction is randomized).
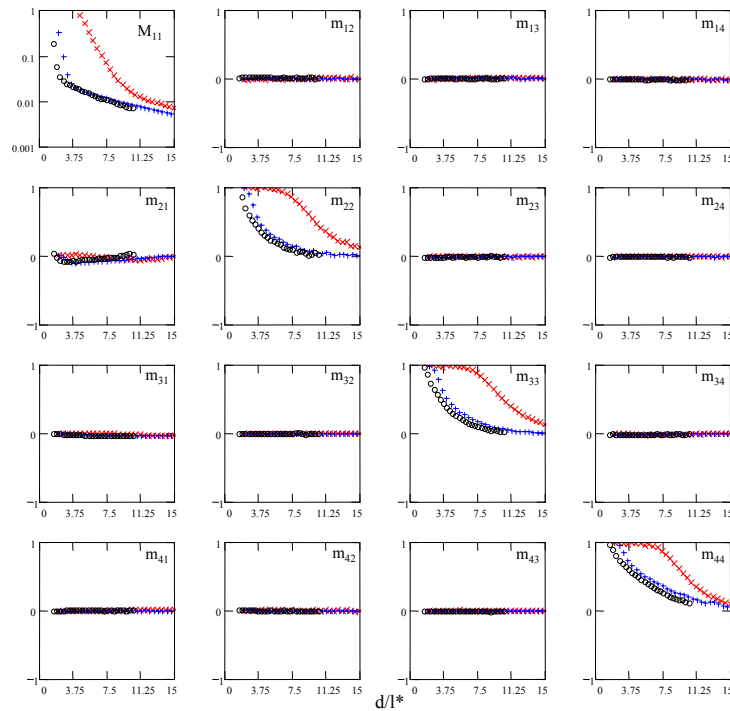

Figure 3.11. Experimental Mueller matrix for silica particles of different sizes. Symbols: X-0.2μm, +-0.5μm, O-1.0μm.

114

All matrix elements shown in Fig. 3.11 are normalized to the first element M_{11}, and are represented in a linear scale, except for M_{11} that is shown in a semilogarithmic scale. Other plots will be shown here in terms of the number of scattering events d/l, where l is the average distance between two scatterers, also called scattering mean free path. The relation between l and l^* is $l^* = l/(1-g)$ where g is the anisotropy factor.

Based on symmetry considerations, van de Hulst[9] finds the Mueller matrix for single scattering on a collection of randomly oriented identical particles each of which has a plane of symmetry to be of the form:

$$
M = \begin{bmatrix} 1 & 0 & 0 & 0 \\ 0 & m_{22} & 0 & 0 \\ 0 & 0 & m_{22} & 0 \\ 0 & 0 & 0 & m_{44} \end{bmatrix}.
\tag{118}
$$

For spheres in exact forward scattering $m_{22} = m_{44} = 1$. In multiple scattering however, this relation is not true anymore, as it can be seen in Fig. 3.11. It it also expected that light of arbitrary incident polarization impinging on an optically thick, multiple scattering medium emerges diffusely and totally depolarized. As shown in Fig. 3.11, when increasing the optical density, the transfer matrix evolves toward that of a total depolarizer which has all elements equal to zero except for M_{11}. Also, the depolarization process depends on the size parameter of the scattering particles; owing to a smaller scattering anisotropy for the particles with the size parameter close to 1, the total depolarization stage is reached at higher optical density than for larger particles (ka equal to 3.3 or 6.6). The transmission of unpolarized light (M_{11}) through a sample follows an exponential decay with pathlength

115

as given by Lambert-Beer's law. Two different regimes can be identified in terms of optical density d/l^*: i) a steep slope for low optical densities, which corresponds to the attenuation of ballistic photons, and ii) a slower decay for large optical densities, corresponding to the diffusive regime. As shown in Fig. 3.11 for the element M_{11}, the optical density required to eliminate the ballistic photons is larger for smaller particles. In the diffusive regime, the decay rate is similar for the three samples and depends only on the volume fraction of the scattering medium.

Previous studies investigated the depolarization effects for a specific type of input state of polarization (linear or circular).[69] These results can be easily derived from our analysis of the Mueller matrix. The first element, M_{11} describes the transmission of the unpolarized incident light, m_{22} and m_{33} relate the linear components of the scattered light to the linear components of the incident light, while m_{44} has only contributions from the transfer of circular components of the incident light.

The transmission of unpolarized light (M_{11}) through a sample follows an exponential decay with the pathlength as given by Beer's law $I(d) = I_o \exp(-\alpha d) = I_o \exp(-\alpha' d/l^*)$, where α is the attenuation coefficient. In a semilogarithmic scale, as shown in Fig. 3.12 a, the slope α' is approximately the same for the three samples. The effective coefficient of attenuation α' depends only on the volume fraction of the scattering medium. Deviations from this exponential decay are shown for small number of effective scattering events, where the thickness of the sample is very small and many ballistic photons pass through. The decrease in the number of ballistic photons follows also an exponential decay, but the effect is more pronounced for the smallest particle $(0.2 \mu m)$, where the length of the

sample required to eliminate all ballistic photons is larger. Fig. 3.12 b shows the decay of M_{11} in d/l scale. One can note that the smaller the particle, the steeper the decay in this representation.
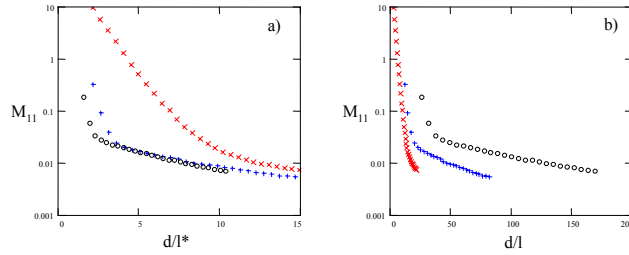

Figure 3.12. Matrix element M_{11} - transmission of unpolarized light. Symbols: X-$0.2\mu m$, +-$0.5\mu m$, O-$1.0\mu m$.

The dependence of the diagonal elements m_{22}, m_{33}, m_{44} on the number of scattering events d/l is plotted in Fig. 3.13. The variation with d/l^* of the diagonal Mueller matrix elements m_{22} (+), m_{33} (X), m_{44} (O) is shown in Fig. 3.14 for each individual sample (1 - $0.2\mu m$, 2 - $0.5\mu m$, and 3 - $1.0\mu m$). We note that for samples 2 and 3, m_{44} is always larger than the other two elements which are about equal, as apparent in Eq. 118. This is not the case for sample 1 where all three elements are equal, following the same decay.
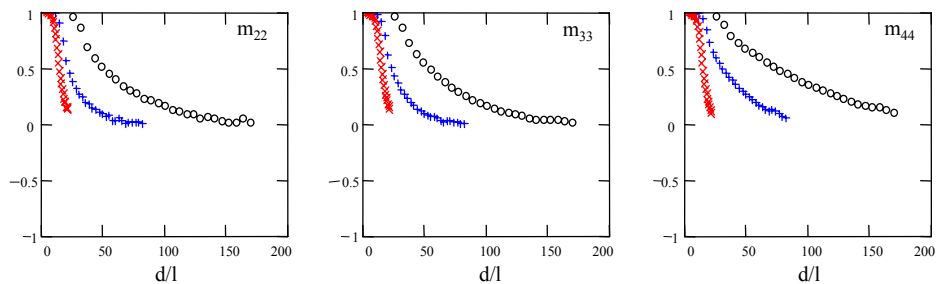

Figure 3.13. Diagonal elements m_{22}, m_{33}, m_{44}. Symbols: X-$0.2\mu m$, +-$0.5\mu m$, O-$1.0\mu m$.

117

For an input state of polarization as described by Eq. 3, the output state of polarization can be obtained from $S_{out} = MS_{in}$. In the case of a diagonal type matrix, the re-normalized output Stokes vector is

$$S_{out} = \begin{bmatrix} 1 & qm_{22} & um_{33} & vm_{44} \end{bmatrix}^T.$$ (119)
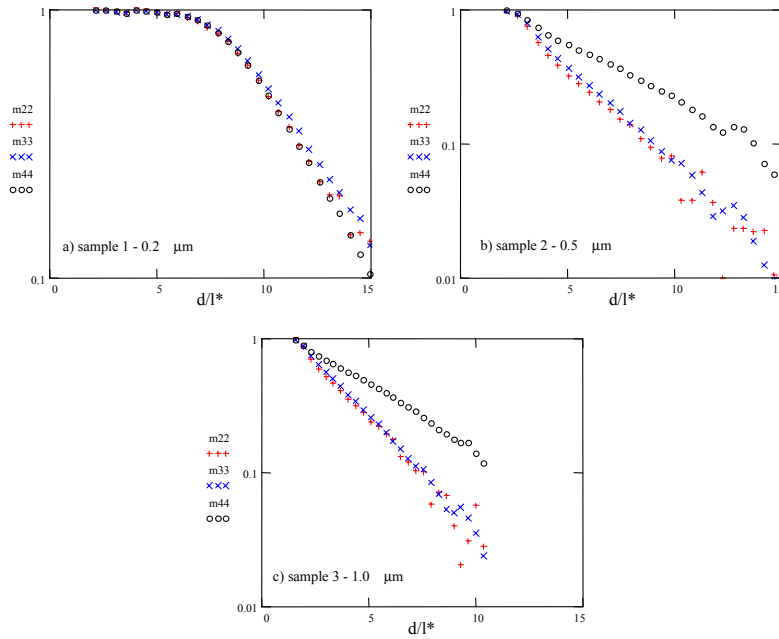
Figure 3.14. Diagonal elements in semi-logarithmic scale for each sample (a) - $0.2\mu m$, b) - $0.5\mu m$, and c) - $1.0\mu m$). Symbols: +-m22, X-m33, O-m44.

The degree of polarization of the scattered light can be obtained from Eq. 119 using Eq. 4 for any input state. The results of this analysis are presented in Fig. 3.15 and 3.16 for linear and circular input, respectively. As can be seen, for samples 2 and 3 the slope for linear input is always steeper than for circular input, indicating that circularly polarized light is less depolarized than linearly polarized light for the same sample thickness.

118

However this behavior is different for small particles in the transition regime (sample 1) between Mie scattering (samples 2 and 3) and Rayleigh regime (ka <<1).
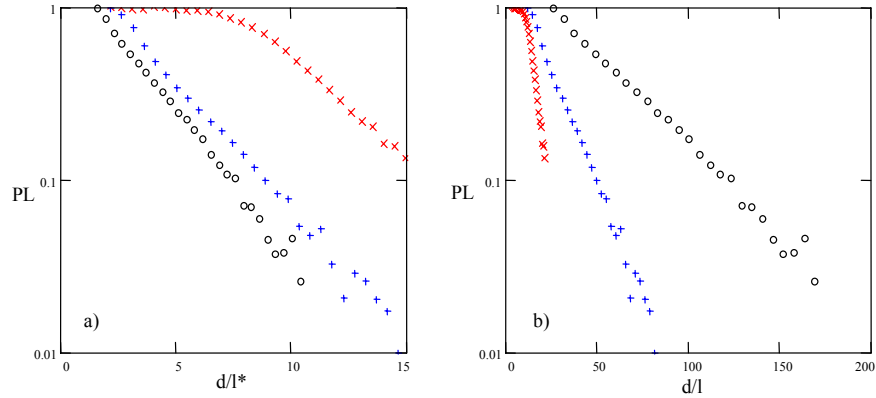
Figure 3.15. Degree of polarization of output light, for linear input. a) - d/l^* scale, b) - d/l scale. Symbols: X-sample 1, +-sample 2 and O-sample 3.

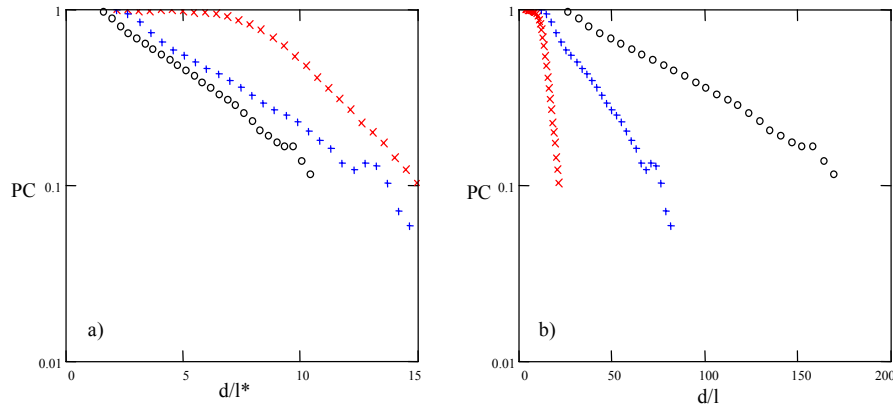Figure 3.16. Degree of polarization of output light, for circular input. a) - d/l^* scale, b) - d/l scale. Symbols: X-sample 1, +-sample 2 and O-sample 3.

It is expected that, as soon as the diffusive regime is reached, multiple scattering will completely depolarize the incident optical wave. The three samples investigated show similar decays of the depolarization index D (formula 5) as function of d/l^* (Fig. 3.17

119

a). For sample 1 (symbol X) the deviation for small number of effective scattering events indicates again the contribution of ballistic photons. In d/l scale (Fig. 3.17 b), the behavior is different. One can conclude that the larger the particle, the larger the number of scattering events required to depolarize the incident light.
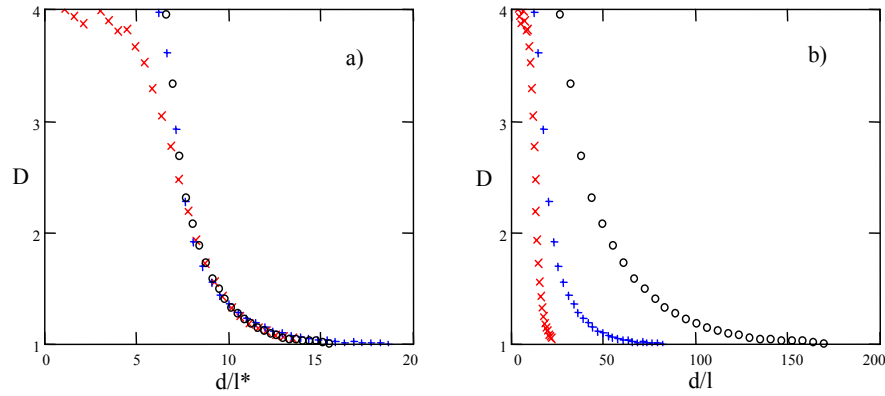
Figure 3.17. Depolarization index D. Symbols: X - sample 1, + - sample 2, O - sample 3.

Knowing the complete Mueller matrix, the state of polarization of scattered light can be estimated for any input state of polarization. A detailed analysis can also predict which type of illumination is better preserved while propagating through the scattering medium. This is particularly important in applications such as long-range target identification where one must take into account depolarization effects due to propagation.

3.3.2. Fibers

As discussed before on the basis of symmetry considerations, it can be shown that[9] the Mueller matrix for single scattering on a collection of randomly oriented identical particles,

120

each of which has a plane of symmetry, is of the form shown in formula 118. In forward scattering, for randomly oriented rotationally symmetric particles much larger than the wavelength, the diagonal elements of the Mueller matrix should be always equal.[9,125,126] If the off-diagonal elements do not vanish for a collection of elongated particles with mirror symmetry (cylinders in our case), then certain degree of alignment is implied.[12] Also, in the transition regime from single to multiple-scattering, it will be shown here that the diagonal elements decrease and the Mueller matrix evolves toward that of a total depolarizer. In order to understand the effect of optical density on the scattering properties of the system, the polarization transfer through systems consisting of layers of randomly oriented fibers stacked together was analyzed. To date, there are no published theoretical results, numerical simulations or experimental investigations addressing the dependence of the scattering properties on optical density for cylindrical scatterers in random orientation, ranging from single to multiple scattering regime.

Fig. 3.18 shows the experimental values of the Mueller matrix elements corresponding to scattering media with an increasing number of normally illuminated layers that have similar scattering properties. Results are presented for systems of up to 20 layers of average thickness $60\mu m$; it can be considered that the number of layers is proportional with the overall optical density of the scattering medium. All the Mueller matrix elements presented in Fig. 3.18 are normalized to the first element M_{11} (and denoted by small letter m), while the top-left corner shows in logarithmic scale the measured element M_{11}.

As can be seen in Fig. 3.18, all the off-diagonal elements are zero indicating no particular orientation of the scatterers, as well as no overall birefringence or dichroism. A

121

careful analysis of the dependence of the diagonal elements with the optical density shows that, up to about four layers forward scattered and ballistic photons are dominant and the degree of polarization is well preserved. As predicted for randomly oriented particles much larger than the wavelength, in single scattering regime the three diagonal elements are equal. In multiple scattering regime they decay in about the same manner, as seen in Fig. 3.18. When multiple scattering starts to act significantly on the balance of energy transfer, an initially exponential decay sets in and, after about 15 scattering layers, a diffusive regime evolves where the slope of the decay depends on scattering properties of individual scattering centers. This effect is clearly visible for the element M_{11}.
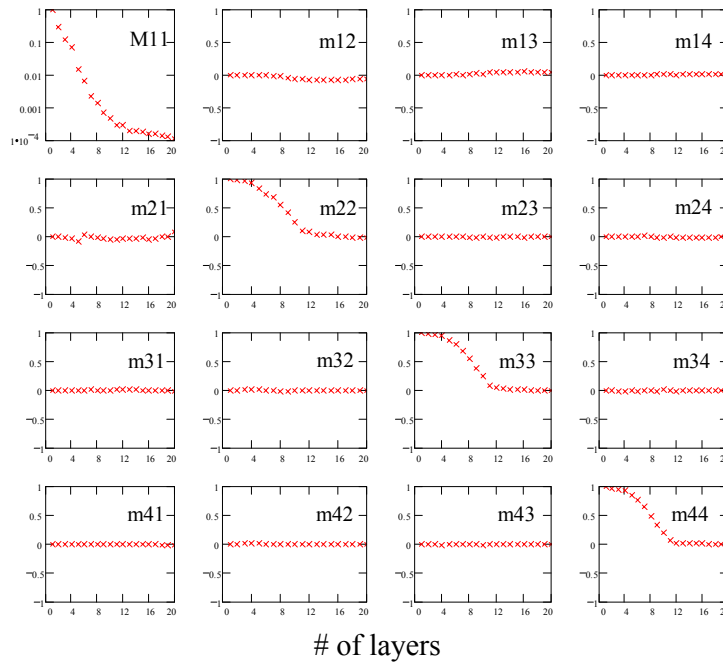

Figure 3.18. Evolution of the Mueller matrix with the number of layers of cylinders stacked together.

With the increase of optical density, the Mueller matrix evolves toward that of an ideal depolarizer which is also shown in Fig. 3.19 which presents the variation of the depolarization index D (formula 5) with the optical density (directly proportional to the number of layers).

Forward (single) scattered and ballistic components preserve the input state as seen in Fig. 3.18 for up to four layers (the Mueller matrix is practically identity). This represents the single scattering regime distinctively seen for the diagonal elements in Fig. 3.18 and for the depolarization index in Fig. 3.19. The multiple scattering, on the other hand, is characterized by very small values of the diagonal elements, a value of the depolarization index D almost unity, and small values of the degree of polarization of the transmitted light. This regime is clearly seen in Fig. 3.18 and 3.19 for stacks of 15 to 20 layers. The transition regime between single and multiple scattering, for stacks between 4 and 15 layers, is characterized by an exponential decay of the diagonal elements of the Mueller matrix, of the depolarization index D, and of the polarization degree of the scattered light.
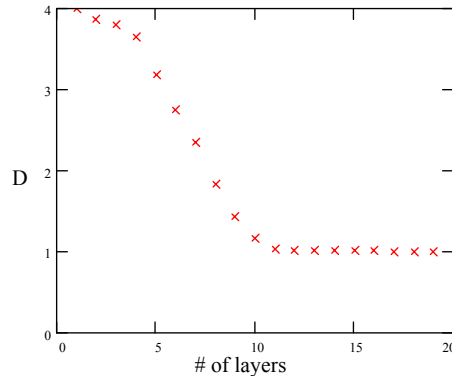

Figure 3.19. Depolarization index D as function of the number of layers.

123

In certain applications such as long range target identification, it is important to know what type of polarization is better preserved during propagation through atmosphere. Once the Mueller matrix is known for a specific scattering medium, the transmitted light can be investigated for any input state of polarization. For a normalized input Stokes vector $S_{in} = \{1, q, u, v\}^T$, and the measured Mueller matrix of the type specified by Eq. 118 and presented in Fig. 3.18, the Stokes vector of the scattered light is given by Eq. 119. The degree of polarization of the scattered light is then expressed by $P = \sqrt{q^2 m_{22}^2 + u^2 m_{22}^2 + v^2 m_{44}^2}$, and can be calculated for linear (PL) or circular(PC) input.
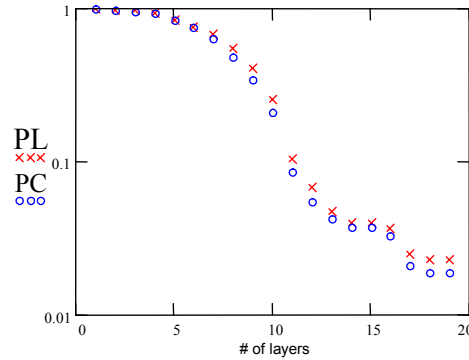
Figure 3.20. Degree of polarization of the transmitted light corresponding to linear (PL) and circular (PC) input state of polarization, as function of the number of layers.

Fig. 3.20 depicts the degree of polarization of the transmitted light corresponding to linear (PL - symbol X) and circular (PC - symbol O) input, respectively. For spherical particles, in multiple scattering regime, the ratio $R = PL/PC$ relates to the size of the particle.[69, 89] In Fig. 3.21 a the dependence of R on the optical density is shown for spherical silica particles with diameter of $0.2\mu m$ (symbol - filled circle) and $1\mu m$ (symbol - open circle) as compared with polyhedral, alumina particles with an average

124

size of $1.2\mu m$ (symbol - diamond). For spherical particles, $R > 1$ corresponds to Rayleigh scatterers, while $R < 1$ indicates scatterers with size parameter larger than unity. The absolute difference between size parameter and unity is proportional with the slope of R. However, this does not seem to hold for nonspherical particles with either random or partial orientation. Fig. 3.21 a shows that polyhedral alumina particles with random orientation behave like smaller spheres than indicated by conventional light scattering methods (the slope of R is smaller than for silica spheres). As can be seen in Fig. 3.21 b, R is slightly increasing with the optical density of fibers, behaving somehow unexpected, similar to the case of scatterers with size parameter close to unity.

a)   b)
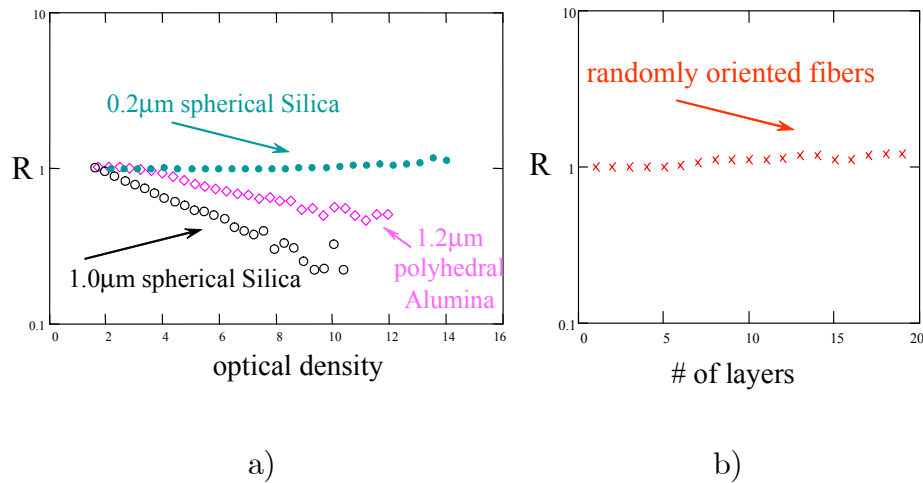
Figure 3.21. Values of the ratio R plotted as function of optical density for a) alumina particles - $1.2\mu m$ (diamond), silica particles - $0.2\mu m$ (filled circle), silica particles - $1.0\mu m$ (empty circle), and b) randomly oriented cylindrical fibers.

It is sometimes considered that ensembles of randomly oriented nonspherical particles are equivalent to distributions of spherical particles and the only outstanding problem is to

125

choose the right size distribution;[12] the motivation behind this is that random orientation results in spherical symmetry.

For Rayleigh regime, the scattering can be considered as being due to spheres with equivalent volume accounting for an equivalent number of re-radiating dipoles. In the case of scattering from large particles, spheres with equivalent projection area are considered; this approach is based on Fraunhofer diffraction theory with main contribution from the edge of large particles. This is especially true for large particles where the scattering is concentrated mostly in forward direction,[121] but the scattering is azimuthally dependent for oriented nonspherical particles, unlike scattering from spheres.[12] This type of equivalence might be valid for a scalar model based on intensity measurement only. In polarimetry however, this equivalence is not always true, as this analysis suggests. Large cylindrical fibers, and polyhedral particles do not behave like equivalent spheres, as can be seen in Fig. 3.21.

3.4. Optical activity

Optical activity manifests as either circular birefringence, or circular dichroism. Certain materials have the ability of rotating linear polarization (due to the different propagation speed of the orthogonal circular polarizations), or to attenuate differently orthogonal circular polarizations. Measurements of optical activity have been performed for a long time on homogeneous materials. The effect can be magnetically induced, or it can be a natural, intrinsic property of the material due to its internal structure. The polarimetric

126

characteristics of optically homogeneous materials are first presented here, and then a model for the optical activity effects in multiple scattering media is developed.

3.4.1. Circular birefringence in homogeneous materials

3.4.1.1. Magneto-optical activity

The Mueller matrix of an optical system having a small linear birefringence δ_o (with axis orientation ρ) and circular birefringence (CB) δ_c that is magnetic field B dependent is given for small values of δ_c by

$$M(B) = \begin{bmatrix} 1 & 0 & 0 & 0 \\ 0 & 1 & -\delta_c(B) & -\sin(2\rho)\sin(\delta_o) \\ 0 & \delta_c(B) & 1 & \cos(2\rho)\sin(\delta_o) \\ 0 & \sin(2\rho)\sin(\delta_o) & -\cos(2\rho)\sin(\delta_o) & 1 \end{bmatrix}. \tag{120}$$

The material investigated here, a magnetic crystal ($Cd_{1-x}Mn_xTe$, $x = 0.45$, 1.1mm thick), exhibits Faraday effect. The magnetic field B is applied along the direction of propagation of the laser beam, being perpendicular to the electric field of light. Fig. 3.22 shows the measured Mueller matrix for the magnetic crystal as function of the applied magnetic field B. The matrix elements m_{23} and m_{32} show circular birefringence δ_c that depends on the magnetic field B, while m_{24}, m_{34}, m_{42}, and m_{43} indicate an intrinsic linear birefringence ($\delta_o = 14.24°$ at an angle $\rho = 8.6°$) independent of the magnetic field B. The CB dependence on the magnetic field B is $\delta_c(B) = VBL$, where V is the Verdet constant characteristic to this material and L is the length of the sample. The value of the Verdet constant obtained here is $V = 4000 m^{-1}T^{-1}$.

127
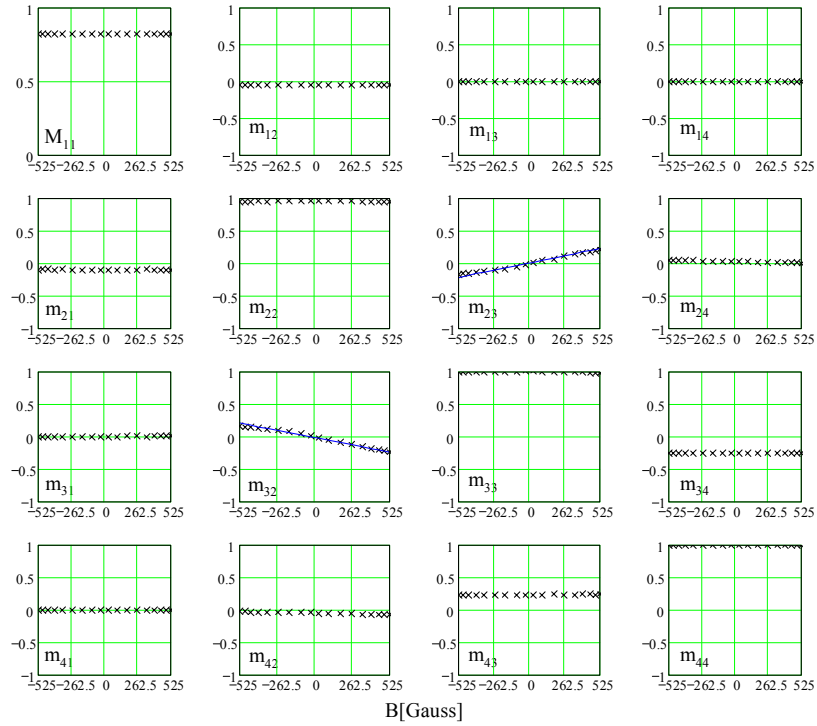
Figure 3.22. The Mueller matrix of a magnetic crystal as function of the magnetic field.

3.4.1.2. Natural optical activity

The Mueller matrices for fructose (shown in Fig. 3.23) and galactose were measured for testing the natural optical activity exhibited by solutions of sugar in water. The measurements were made in transmission through a glass cell with adjustable length.

The matrix elements m_{12}, and m_{21} show a residual polarizing effect due to the cell as indicated by the ellipsometric parameter Ψ in Eq. 97, while the elements m_{24}, m_{34}, m_{42}, and m_{43} show a residual birefringence ($4.15°$) of the adjustable width cell, at an angle of $15°$, according to the Eq. 120. These effects do not depend on the length d of the cell.

128
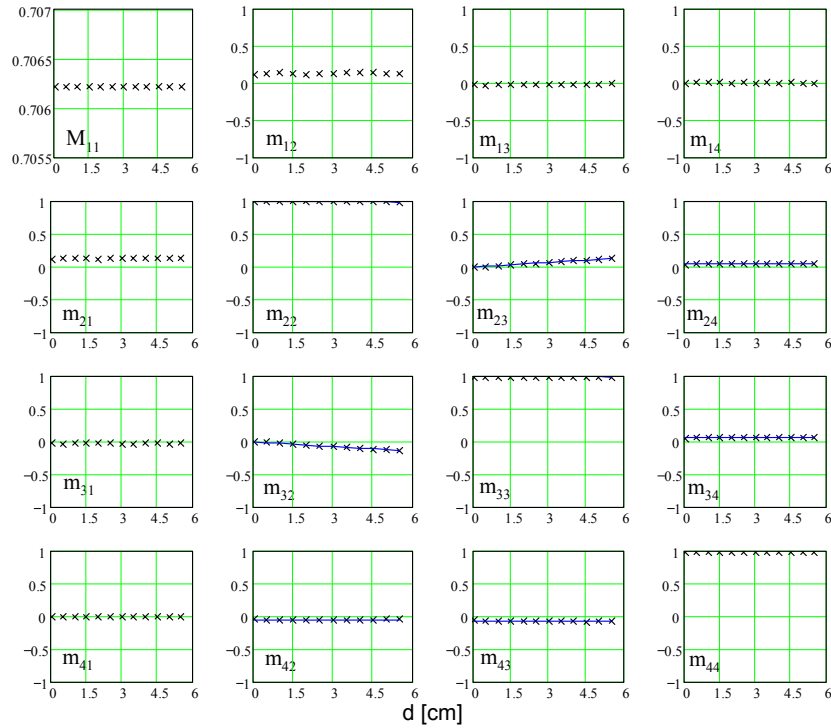
Figure 3.23 Mueller matrix for fructose solution as function of length d of the cell.
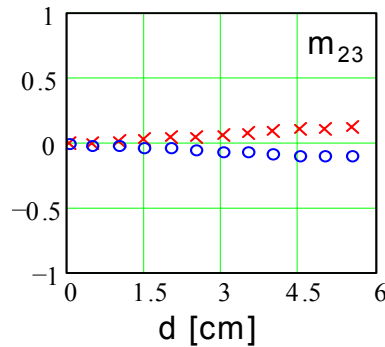
Figure 3.24 Matrix element 23; red crosses - fructose, blue circles - galactose.

The elements m_{23} and m_{32} are fitted with $\sin(2\theta)$ and $-\sin(2\theta)$ respectively, where the rotation angle θ is directly proportional to the length d of the cell $\theta = \alpha d$, and α is the rotatory power. Also, the elements m_{22} and m_{33} are fitted with $\cos(2\theta)$, close to 1 for small values of θ. Fig. 3.24 shows the element m_{23} for fructose - red crosses,

129

and galactose - blue circles. The rotation has opposite signs confirming the two types of clockwise (dextrorotatory) and anti-clockwise (levorotatory) enantiomers. For these particular samples, $\alpha = 0.012 deg./cm$ for fructose, and $\alpha = 0.008 deg./cm$ for galactose.

The effects described here are the building blocks of the model that will be presented in the following Section describing optical activity in multiple scattering.

3.4.2. Optical activity in scattering media

The purpose of this study is to help us understand the effect of optical activity in multiple scattering regime and to evaluate the magnitude of this effect that would subsequently set the constraints on the experimental measurement. This study is relevant for medical applications and for remote sensing of biological material.

The geometry under consideration is shown in Fig. 3.25. Only the photons collected along the same direction as the incident ones are considered here in a slab configuration in transmission.

Figure 3.25. Slab configuration in transmission.
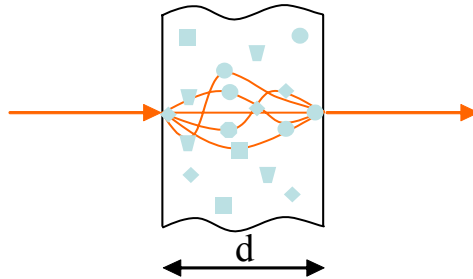
130

The incident photons propagate through the scattering medium following various trajectories which can be considered as tortuous cylinders of active material with a cross-section of the order of λ^2. Along each path of length s, the incident state of polarization rotates due to circular birefringence (CB) and acquires a certain ellipticity due to circular dichroism (CD). The rotation and the ellipticity depend on the pathlength s and optical activity properties of the medium

$$\theta(s) = \frac{2\pi}{\lambda}(n_L - n_R)s = \alpha s \tag{121}$$

$$\delta''(s) = \frac{2\pi}{\lambda}(n'_L - n'_R)s = \beta s \tag{122}$$

where n_L and n_R are the refractive indices for the two circular polarizations, and the prime terms represent the corresponding absorptions. At the output face, the state of polarization in each particular point is determined by incoherently adding the Stokes vectors for all trajectories that end up there, each of them being weighted with its corresponding probability. From the output Stokes vector one can determine the overall rotation, ellipticity and degree of polarization of the transmitted light.

The model outlined here is applicable to two different cases: (1) non-chiral scatterers suspended in a chiral medium, and (2) chiral scatterers in a non-chiral medium. In both cases, the rotation and the ellipticity are proportional to s, but the proportionality constants α and β in Eqns. 121-122 have to take into account the amount of active material along each path. For large particles, such as droplets and grains, the phase function is mostly peaked forward resulting in a large probability of forward scattering. In this case, the Mueller matrix for non-active particles is generally diagonal, close to identity matrix. This model allows neglecting the scattering properties of the particles,

131

and permits considering only snake-like trajectories without sharp turns. In other words, individual scattering events determine various propagation channels without affecting the output polarization.

The probability distribution function is calculated as a solution of the photon diffusion equation for the slab geometry[127]

$$T\left(OD, l^*, z_o, s\right) = s^{-\frac{5}{2}} \sum_{i=1,odd}^{\infty} \left\{ (i \cdot OD - z_o) \, exp \left[-\frac{3l^*}{4} \frac{(i \cdot OD - z_o)^2}{s} \right] - \right. \tag{123}$$

$$\left. - (i \cdot OD + z_o) \, exp \left[-\frac{3l^*}{4} \frac{(i \cdot OD + z_o)^2}{s} \right] \right\},$$

where l^* is the transport mean free path, z_o is the extrapolation length, s is the pathlength, and $OD = d/l^*$ is the slab's optical density (d is the thickness of the slab).

Fig. 3.26 illustrates the pathlength probability distribution for different optical densities, as indicated in the legend. As can be seen, when the optical density increases, the probability distribution becomes broader and its maximum value decreases.
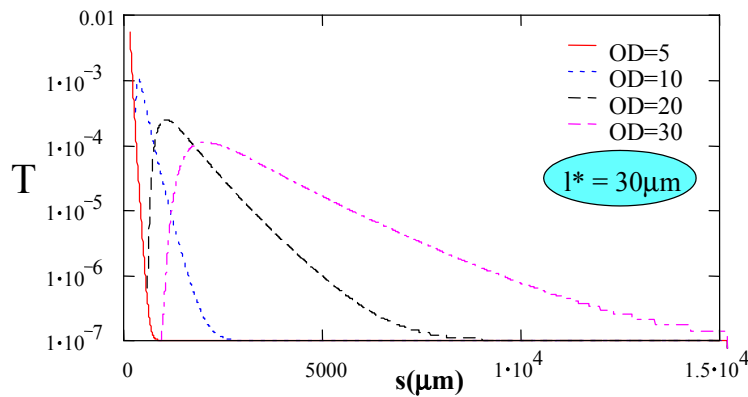
Figure 3.26. Pathlength distribution for various optical densities.

As mentioned before, circular birefringence manifests as a rotation of a linear input with an angle proportional to the length s of the path (see Eq. 121). Using the matrix $M(\theta)$ of a rotator (formula 9), the Stokes vector at the end of a path of length s can be written as

$$S(\theta) = M(\theta) \begin{bmatrix} 1 \\ 1 \\ 0 \\ 0 \end{bmatrix} = \begin{bmatrix} 1 \\ \cos(2\theta) \\ -\sin(2\theta) \\ 0 \end{bmatrix}. \tag{124}$$

One can notice that the output for any individual path is still linear, i.e. CB does not generate ellipticity.

The output Stokes vector $S = [1, q, u, 0]^T$ is obtained by integrating all Stokes vectors (over the probability function for pathlength):

$$q(\alpha, OD, l^*) = \int_d^\infty \cos(2\alpha s) T(s) ds \tag{125}$$

$$u(\alpha, OD, l^*) = -\int_d^\infty \sin(2\alpha s) T(s) ds. \tag{126}$$

The degree of polarization P is then obtained using Eq. 4, while the rotation is calculated as $\theta = \frac{1}{2} \arctan \frac{u}{q}$.

The Mueller matrix corresponding to this effect is

$$M(\alpha, OD, l^*) = \begin{bmatrix} 1 & 0 & 0 & 0 \\ 0 & q & u & 0 \\ 0 & -u & q & 0 \\ 0 & 0 & 0 & 1 \end{bmatrix}. \tag{127}$$

One can notice that a circular input is eigenvector for this transformation, and there is no change of intensity and degree of polarization.

133

Fig. 3.27 depicts the Stokes components q and u as function of OD for $l^* = 10, 30, 60$, and $100\mu m$ and $\alpha = 0.0006 rad/\mu m$. One can see that both q and u tend to zero with the optical density and strongly depend on l^*.
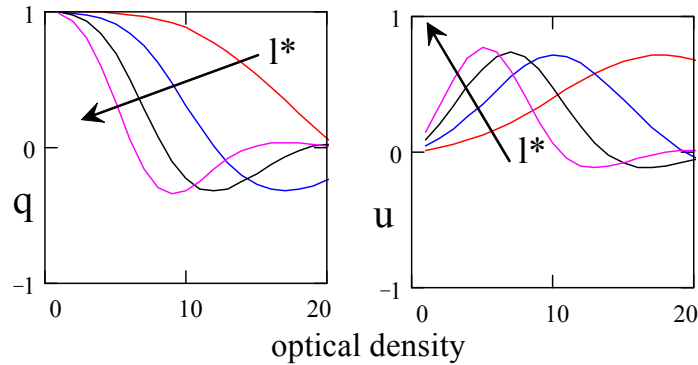
Figure 3.27. Stokes vector components q and u.

Fig. 3.28 shows the degree of polarization P and the rotation θ as function of OD for various l^*, and for different values of the CB. One can notice a significant dependence on l^*, as well as a strong dependence on the rotatory power and the concentration of the optically active material (both included in the proportionality constant α). The output light is stronger depolarized as the optical density increases, the slope of the degree of polarization being proportional to both l^* and α. Similarly, the rotation θ of the linearly polarized component increases with OD with a slope proportional to both l^* and α.
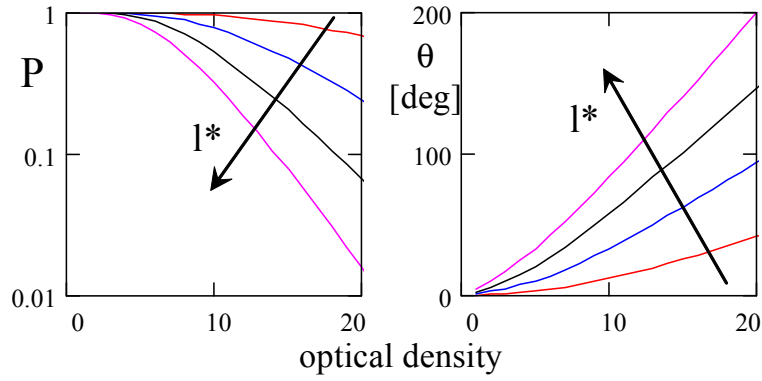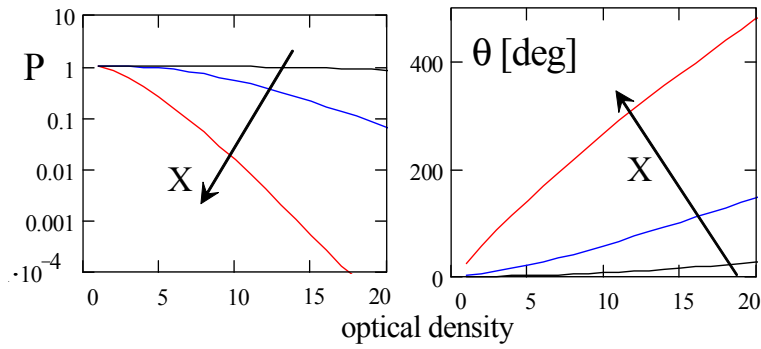
Figure 3.28. Degree of polarization P and rotation θ as function of OD a) for various l^*, and b) for different values of the CB (l*=60μm, and α=0.06, 0.006, 0.0006rad/μm).

A similar calculation can be applied to situations involving circular dichroism. Using

the Mueller matrix for CD[121]

$$
M(\delta'') = \begin{bmatrix} 1 & 0 & 0 & \tanh(\delta'') \\ 0 & \frac{1}{\cosh(\delta'')} & 0 & 0 \\ 0 & 0 & \frac{1}{\cosh(\delta'')} & 0 \\ \tanh(\delta'') & 0 & 0 & 1 \end{bmatrix} \tag{128}
$$

the Stokes vector is obtained as

$$S(\delta'') = M(\delta'') \cdot \begin{bmatrix} 1 \\ 1 \\ 0 \\ 0 \end{bmatrix} = \begin{bmatrix} 1 \\ \frac{1}{\cosh(\delta'')} \\ 0 \\ \tanh(\delta'') \end{bmatrix}. \tag{129}$$

In this case, a linear input maintains its orientation, but acquires an ellipticity proportional to the length of the path. Integrating the individual Stokes vectors weighted by the corresponding probability one obtains the output Stokes vector $S = [1, q, 0, v]^T$ where

$$q(\beta, OD, l^*) = \int_d^\infty \frac{1}{\cosh(\beta s)} T(s) ds \tag{130}$$

$$v(\beta, OD, l^*) = \int_d^\infty \tanh(\beta s) T(s) ds. \tag{131}$$

The degree of polarization P is obtained again using the Eq. 4. The ellipticity is given by $\varphi = \frac{1}{2} \arcsin(v)$.

The Mueller matrix corresponding to this effect is

$$M(\alpha, OD, l^*) = \begin{bmatrix} 1 & 0 & 0 & v \\ 0 & q & 0 & 0 \\ 0 & 0 & q & 0 \\ v & 0 & 0 & 1 \end{bmatrix}. \tag{132}$$

A circular input is again eigenvector for this transformation, however the intensity is now decreasing, as opposed to the birefringent case.

Fig. 3.29 shows the Stokes components q and v as function of OD for $l^* = 10, 30, 60,$ $100\mu m$ and $\beta = 0.0003 rad/\mu m$. One can see that q deceases to zero while v increases to unity with the optical density, the slope of these variations depending on l^*.

136
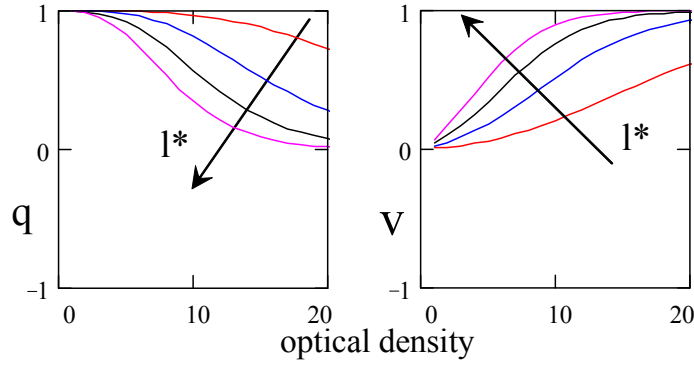
Figure 3.29. Stokes vector components q and v.

Fig. 3.30 illustrates the degree of polarization P and the ellipticity φ as function of OD for various l^*, and for different values of the CD. In this case as well, one can notice significant differences with l^*, and a strong dependence on the amount of dichroism included in the proportionality constant β.

It is worth noting in Fig. 3.30 that the degree of polarization P slightly decreases and returns to 1 while the ellipticity saturates at $45°$ as OD increases. If one decomposes the linear input in the two circular components, one component is attenuated stronger than the other one while propagating through the medium (this is the meaning of circular dichroism). At some point, the more attenuated component becomes negligible, and what is left from all trajectories is the circular component less attenuated. P becomes 1 and φ is $45°$, meaning circular light. For what OD does this happen, it depends on both l^* and β, as seen in Fig. 3.30.

137
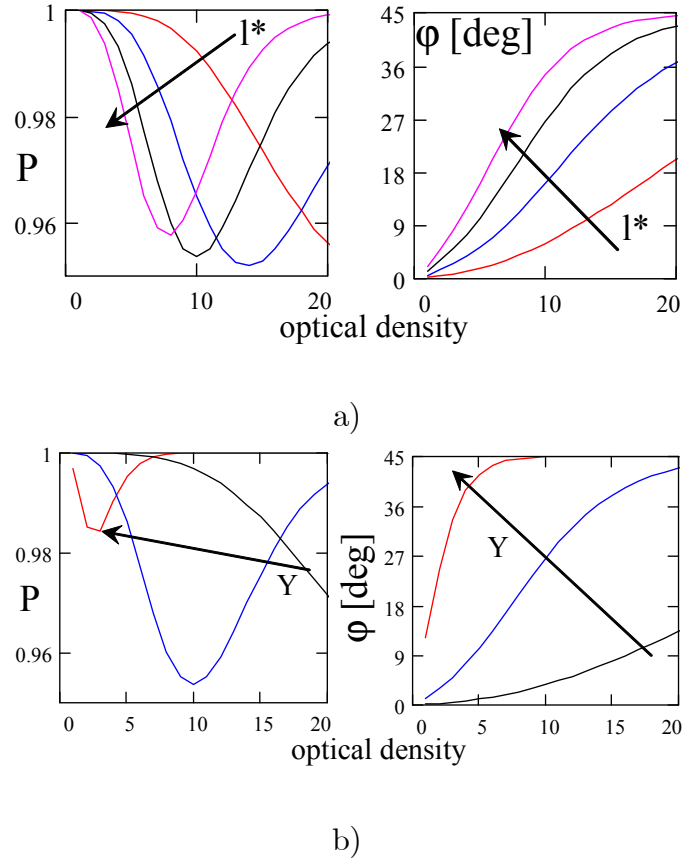
Figure 3.30. Degree of polarization P and rotation θ as function of OD a) for various l^*, and b) for various values of the CD ($l^* = 60\mu m$, and $\beta = 0.003, 0.0003, 0.00003 rad/\mu m$).

For unpolarized input, the output is still unpolarized in the CB case

$(S(\theta) = M(\theta)[1,0,0,0]^T = [1,0,0,0]^T)$. For CD however,

$$S(\delta'') = M(\delta'') \begin{bmatrix} 1 \\ 0 \\ 0 \\ 0 \end{bmatrix} = \begin{bmatrix} 1 \\ 0 \\ 0 \\ \tanh(\delta'') \end{bmatrix} = \qquad (133)$$

$$= (1 - |\tanh(\delta'')|) \begin{bmatrix} 1 \\ 0 \\ 0 \\ 0 \end{bmatrix} + |\tanh(\delta'')| \begin{bmatrix} 1 \\ 0 \\ 0 \\ sign(\delta'') \end{bmatrix}.$$

The output has two components, an unpolarized one and a circularly polarized one as illustrated by the decomposition in the second line of the Eq. 133. As OD increases the ratio of these two components changes, and at some point the output becomes fully polarized as shown in Fig. 3.31. This demonstrates the possibility of obtaining a diffuse circular polarizer if optical activity effects are present.
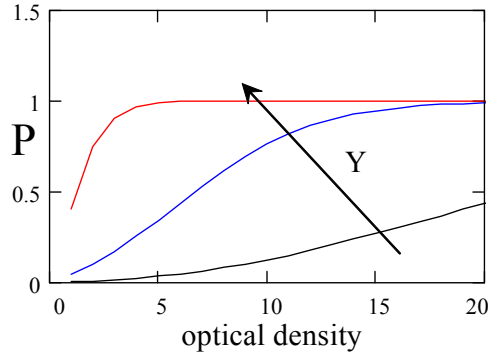
Figure 3.31. Degree of polarization as function of OD for unpolarized input, for $l^* = 60\mu m$, and $\beta = 0.003,\ 0.0003,\ 0.00003 rad/\mu m$.

A more realistic model should also include scattering effects at the level of each scatterer. These effects depend on the size and the shape of the particle, and if one considers the type of the matrices discussed in Section 3.3 for forward multiple scattering regime, the matrix is in general diagonal with the diagonal elements decaying exponentially with OD. Considering that optical activity and multiple scattering are multiplicative effects,

139

one obtains the output Stokes vector for CB and CD respectively as $[1, qa, 0, 0]^T$ and $[1, qa, 0, vc]^T$, where a and c are exponential functions of OD (experimentally obtained for polyhedral alumina particles of $3.2 \mu m$ average size for the example illustrated in Fig. 3.32).
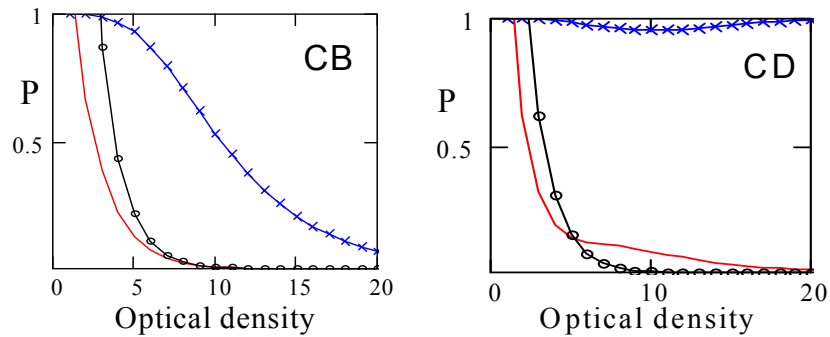
Figure 3.32. P as function of OD for: only scattering (o), only optical activity (X), and combined effects (continuous line).

Fig. 3.32 shows the degree of polarization P as function of OD for only scattering, only optical activity, as well as for the combined effects. One can notice that in the CB case, the two effects work together toward depolarizing the light, and the result is a stronger depolarization. In the dichroic case however, the two effects compete with each other and a certain preservation of the degree of polarization is apparent when the optical density increases.

3.5. Characterization of optically dense media

Light scattering from dense scattering media is of interest for many scientific and technological applications including characterization of paints and papers,[128] rough sur-

faces,[129–131] remote sensing,[132–134] as well as various medical noninvasive investigation techniques.[18, 20, 38] There are many theoretical models[135, 136] and numerical procedures[137–139] used for analyzing the polarized scattering pattern from rough surfaces and multiply-scattering media, but they are generally computational extensive, time consuming and the mathematical treatment generally lacks a physical, intuitive description of the scattering phenomena involved. The extensive depolarization and the general symmetries occurring in dense media significantly reduce the polarized component of the scattered light, making long calculations of multiply scattered light quite inefficient. A simple and intuitive model is outlined in this Section for characterization of dense scattering media. To accomplish this task, scattering effects are separated into the surface and volume components, and then examined by using the Mueller matrix formalism.

3.5.1. Physical model

In order to analyze the backscattering Mueller matrix, one must first define the main characteristics of the system. The scattering systems analyzed here are composed of compacted powders with a certain size distribution. The result of compressing the powder is an overall flat surface with a certain orientation with respect to the incident beam. The microscopic surface characteristics are related to the mean size of the particles and the standard deviation of the distribution, as well as the shape of the particles. Since the scatterers are closely packed together, the characteristic scattering length for the bulk of the system is expected to depend only on the size of the particles and not on the density of particles as in the case of colloidal systems.

141

In this model, the scattering contribution can be divided into two main categories treated independently, surface scattering and volume scattering, assuming incoherent addition of the light retroreflected by the surface and the bulk. Surface scattering consists of any scattering that occurs in-plane on the surface; it also accounts for light that may scatter to adjacent particles on the surface, but does not penetrate into the bulk of the sample. Volume scattering consists of scattering events occurring within the bulk of the sample and it comprises both low and high order scattering events; the light is therefore returned partially depolarized.

3.5.1.1. Surface scattering

The specular reflection on a flat surface with a complex relative refractive index n is completely described by the following Mueller matrix[73]

$$M\left(\theta\right) = \frac{1}{2}\begin{bmatrix} r_s^2 + r_p^2 & r_s^2 - r_p^2 & 0 & 0 \\ r_s^2 - r_p^2 & r_s^2 + r_p^2 & 0 & 0 \\ 0 & 0 & 2r_s r_p \cos\left(\delta\right) & 2r_s r_p \sin\left(\delta\right) \\ 0 & 0 & -2r_s r_p \sin\left(\delta\right) & 2r_s r_p \cos\left(\delta\right) \end{bmatrix}, \tag{134}$$

where r_s and r_p are the complex Fresnel reflection coefficients ($r_s = |r_s|\exp(i\varphi_s)$, $r_p = |r_p|\exp(i\varphi_p)$) given by

$$r_s\left(\theta\right) = \frac{\cos\left(\theta\right) - \sqrt{n^2 - \sin^2\left(\theta\right)}}{\cos\left(\theta\right) + \sqrt{n^2 - \sin^2\left(\theta\right)}}, r_p\left(\theta\right) = \frac{n^2 \cos\left(\theta\right) - \sqrt{n^2 - \sin^2\left(\theta\right)}}{n^2 \cos\left(\theta\right) + \sqrt{n^2 - \sin^2\left(\theta\right)}}, \tag{135}$$

and $\delta = \varphi_s - \varphi_p$. For dielectric, nonabsorbing materials, r_s and r_p are real (since n is real) and $\delta = 0$. Formula 134 simplifies in this case to

142

$$M(\theta) = \frac{\left(r_s^2 + r_p^2\right)}{2} \begin{bmatrix} 1 & \frac{r_s^2 - r_p^2}{r_s^2 + r_p^2} & 0 & 0 \\ \frac{r_s^2 - r_p^2}{r_s^2 + r_p^2} & 1 & 0 & 0 \\ 0 & 0 & \frac{2 r_s r_p}{r_s^2 + r_p^2} & 0 \\ 0 & 0 & 0 & \frac{2 r_s r_p}{r_s^2 + r_p^2} \end{bmatrix}. \tag{136}$$

At normal incidence, $\theta = 0$, $r_s^2 = r_p^2 = \left(\frac{n-1}{n+1}\right)^2$, and the Mueller matrix becomes

$$M(0) = \left(\frac{n-1}{n+1}\right)^2 \begin{bmatrix} 1 & 0 & 0 & 0 \\ 0 & 1 & 0 & 0 \\ 0 & 0 & -1 & 0 \\ 0 & 0 & 0 & -1 \end{bmatrix}. \tag{137}$$

Backscattering from a smooth surface results in a well-defined specular reflection, while a rough surface broadens this specular reflection peak. The diagonal elements 22, 33, and 44 will remain 1, -1 and -1, respectively, since only the facets normal to the incident direction will reflect light into the backscattering direction. In such a facet model that we briefly describe below, a rough surface is non-depolarizing while the intensity profile will depend on the surface characteristics.

The facet model considers that the surface is composed of microfacets having orientations (slopes) that follow a certain probability distribution $P(\epsilon)$. For surfaces with a single correlation length a simple model consists of randomly oriented facets with horizontal projections equal to L (see Fig. 3.33). For describing the surface we consider a distribution of heights $P(h)$ as measured from a reference plane following Gaussian statistics with zero mean and σ as the rms roughness.[133] This problem is treated using a geometric optics

143

approach where the characteristic length L of the facets and the standards deviation σ of the heights distribution are larger than the wavelength.

The statistical character of the surface is described by the probability density $P(\epsilon)$ of the distribution of local slopes. In this model, the heights of points separated by L, $h_1(x)$ and $h_2(x + L)$, are statistically independent random variables that have the same probability density. Hence, the joint probability density $P(h_1, h_2)$ factors as $P(h_1)P(h_2)$. It follows that $P(\epsilon)$ also has a Gaussian shape and can be written as

$$P\left(\epsilon\right) = \frac{\exp\left[-\left(\frac{L}{2\sigma}\tan\epsilon\right)^2\right]}{\pi\cos^2\left(\epsilon\right)}. \tag{138}$$
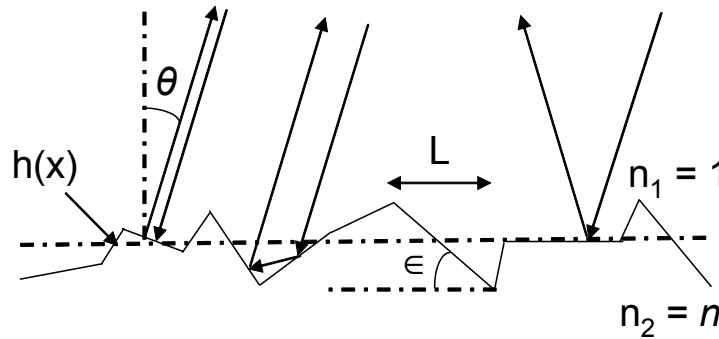
Figure 3.33. Facet model: ϵ - local slope, h(x) local height, L - horizontal projection of facets, n - refractive index, θ - incident (analyzing) direction.

For a compacted powder consisting of polyhedral alumina particles one can assume that the surface of the powder is well described by such a facet model. This description cannot however be directly applied for a powder made of identical spheres. If one considers the spherical surface of a particle as being composed of discrete flat facets, all facets with slopes between $\pm 60°$ have the same probability of occurrence. Therefore, $P(\epsilon)$ is $1/\pi$

for $-\pi/3 < \epsilon < \pi/3$, and zero for larger angles since facets at larger angles are hidden to normal incidence by the neighboring spheres. However, if the powder consists of an ensemble of polydisperse spheres (as is generally the case), smaller spheres will fill in the spaces between larger spheres and the overall surface can be described by the Eq. 138.

Double reflection on adjacent facets is also possible. In order to have light backscattered along the incident direction, the two facets have to be orthogonal. The polarimetric contribution for such a facet pair is given by $M(\theta + \epsilon)M(\frac{\pi}{2} - \theta - \epsilon)$ where θ is the global orientation of the surface and ϵ is the local slope of the first facet. This contribution has to be integrated over a range of slopes between 0 and $\pi/2$ for the first slope (allowing for the second slope to vary between $-\pi/2$ and 0) with the appropriate probability to have a pair of adjacent orthogonal facets. Assuming independent statistics for the two slopes, the joint probability to have such a pair is $P(\epsilon)P(\frac{\pi}{2} - \epsilon)$. Therefore, the contribution of this effect to the backscattered light can be safely neglected at least for narrow distributions of slopes (surfaces that are not very rough).

In the geometry considered here, only those facets that are normal to the incident direction contribute to the backscattered intensity. Specular reflections of the type shown on the right side of the Fig. 3.33 are not detected. The main outcome is that the Mueller matrix corresponding to back-reflection at an angle θ is given by the matrix $M(0)$ for reflection at normal incidence (formula 137) weighted by the probability $P(\theta)$ of having facets oriented at θ.

The probability distribution described by the formula 138 has been derived for the case of rough surfaces[133] having randomly oriented facets with the same horizontal projec-

tion L. This assumption might not always be valid, and different probability distributions should be considered depending on the scattering system. Our measurements on compacted powders are well described by a Lorentzian distribution of slopes, as it will be seen below.

3.5.1.2. Volume scattering

For the volume scattering contribution, the bulk of the sample is considered as being composed of particles closely packed together (see Fig. 3.34). To a first approximation, however, the scatterers are treated as independent and collective scattering is disregarded. It is also assumed that the sample is semi-infinite with no real boundaries and the volume scattering is analyzed separately from the surface effects.
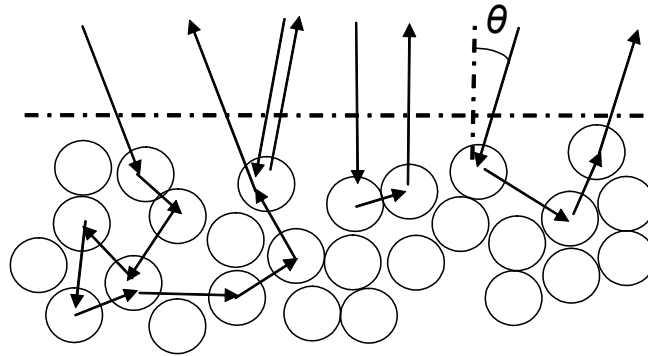

Figure 3.34. Volume scattering.

In transmission configuration through a slab, the Mueller matrix is diagonal with its elements decaying exponentially to zero when the optical density increases.[69, 89] The contribution of ballistic and forward scattered photons, that preserve the incident state of

146

polarization, vanishes for large optical densities, and the scattering system behaves like a total depolarizer. In reflection geometry, however, it is expected that low-order scattering events have always a significant contribution in the power balance. Short trajectories preserve to some extent the input state of polarization, while for long trajectories, multiple scattering completely depolarize the input light. For example, in the case of small particles the phase function is almost isotropic and 2-3 scattering events are highly probable; the reflected light is partially polarized. For large particles, on the other hand, the phase function is strongly peaked forward, short trajectories being less probable than long ones; short trajectories have in this case a small contribution to the back-scattered power, the reflected light being strongly depolarized.

Considering the symmetries discussed for a cloud of particles in Ref.[9] and extending the average over a large number of trajectories inside the compacted powder, it is assumed that the Mueller matrix corresponding to backscattering has a diagonal form

$$M_{vol} = w \begin{bmatrix} 1 & 0 & 0 & 0 \\ 0 & a & 0 & 0 \\ 0 & 0 & b & 0 \\ 0 & 0 & 0 & c \end{bmatrix}, \tag{139}$$

where w, a, b, and c depend on the size of the particles as described above. To a first approximation it is also assumed that the volume scattering is isotropic, independent on the observation direction.

It is also helpful to analyze the extreme cases of particles which are very small and very large as compared to the wavelength. In both cases the amount of multiply scattered, depolarized light is significantly reduced. For very small particles, such as dipoles, the bulk

147

can be considered as a cloud of randomly oriented dipoles (still considered independent) for which the Mueller matrix is diagonal (1, 1, -1, -1). For very large particles, the system becomes homogeneous, behaving like a single rough particle. It is reasonable to assume that the depolarization index, that describes the global depolarization properties of a scattering medium, has a minimum for Mie particles, somewhere in between these limits. The experimental data that is presented in the next Section confirms this assumption.

The surface effects and the volume scattering are considered to be independent processes, and their contributions add on an intensity basis. Therefore, the total Mueller matrix is

$$
M_{total}(\theta) = P(\theta) \left(\frac{n-1}{n+1} \right)^2 \begin{bmatrix} 1 & 0 & 0 & 0 \\ 0 & 1 & 0 & 0 \\ 0 & 0 & -1 & 0 \\ 0 & 0 & 0 & -1 \end{bmatrix} + w \begin{bmatrix} 1 & 0 & 0 & 0 \\ 0 & a & 0 & 0 \\ 0 & 0 & b & 0 \\ 0 & 0 & 0 & c \end{bmatrix}, \tag{140}
$$

where w is the weight of the volume scattering with respect to the surface scattering. Outside the specular reflection peak, where the surface effect becomes negligible, as compared to the volume scattering, the diagonal elements 22, 33, and 44 are determined by a, b, and c respectively.

3.5.2. Experimental results and discussions

The setup comprises a polarization state generator, a sample situated on a rotation stage, and a polarization state analyzer as shown in Fig. 3.35. The laser operates at 532 nm and the polarization generator (Section 2.2.2) produces sequentially 4 states of

148

polarization. The scattered Stokes vector is measured by the polarization state analyzer (Section 2.2.4) for each input polarization and the backscattering Mueller matrix is then calculated. The measurement system is completely automated (LabVIEW controlled).

Seven samples consisting of Silica (size parameter 1.7, 4.3, 8.6, and 12.9, respectively) and Alumina (size parameter 12.7, 32.8, and 105.7, respectively) powders were prepared. The powders were placed into a cylindrical mold and pressed until the surface of the powder was flush with the surface of the mold, providing a flat rigid surface from which to scatter the incident beam. The mold was then mounted on the rotating stage.
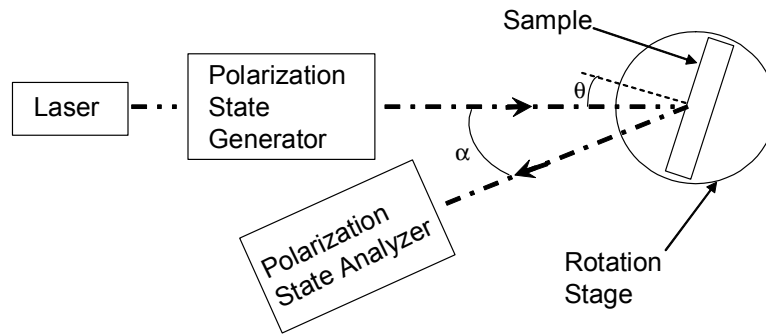
Figure 3.35. Experimental setup.

The angle α between the illumination and analyzing directions (Fig. 3.35) was kept constant at approximately $16°$, resulting in a specular reflection peak at about $8°$ incidence angle, as seen in Fig. 3.36. The experimental errors in determining the Mueller matrix elements is about 2% as confirmed by testing the system on standard optical elements such as quarter and half waveplates and polarizers.

149
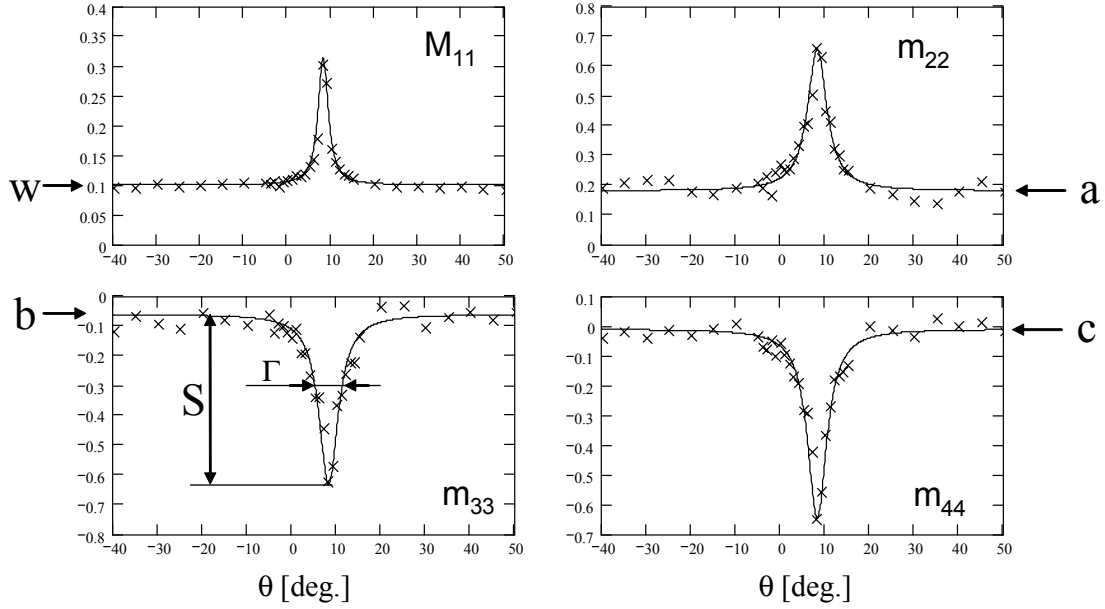
Figure 3.36. Typical experimental results, shown here for Silica particles $1.5\mu m$ diameter.

Measurements of the Mueller matrix began at $-70°$ off normal incidence, and were taken in steps of $5°$ until reaching $-5°$ off normal incidence. From $-5°$ to $15°$ measurements were taken in steps of $1°$ in order to increase the resolution of the specular peak. Measurements from $15°$ to $70°$ were again taken in steps of $5°$.

Fig. 3.36 illustrates typical experimental results. The experimental data is very well fitted with a Lorentzian distribution for slopes,

$$P\left(\theta\right) = \frac{1}{\pi}\frac{\left(\Gamma/2\right)^2}{\left(\theta - \alpha\right)^2 + \left(\Gamma/2\right)^2} \tag{141}$$

where Γ is full width half maximum of the specular reflection peak.

The volume scattering contribution (w, a, b, c) is angularly independent and is evaluated outside the specular reflection peak for each matrix element (as indicated in Fig. 3.36). The magnitude S of the specular reflection peak is measured from this angularly-

150

independent baseline (Fig. 3.36). The base and the magnitude of the peak are determined similarly for the depolarization index D (formula 5).

As predicted by our simple model, the width of the peak depends on the size of the particles, as shown in Fig. 3.37. It is interesting to notice that for spherical Silica particles, the width of the peak is the same for all 3 diagonal elements 22, 33, and 44, but is different for polyhedral Alumina particles. This could indicate a certain sensitivity of the measurement to the shape of the particle which was not included in our model.
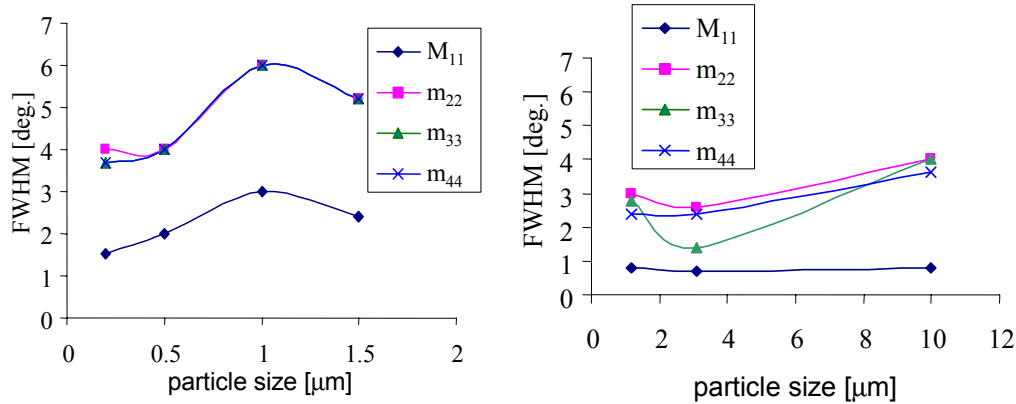
Figure 3.37. Full width half maximum of the specular reflection peak as function of particle size for Silica (left) and Alumina (right).

As seen in Fig. 3.38, the magnitude S of the specular reflection peak changes from element to element, and varies with the size of the particle.

151
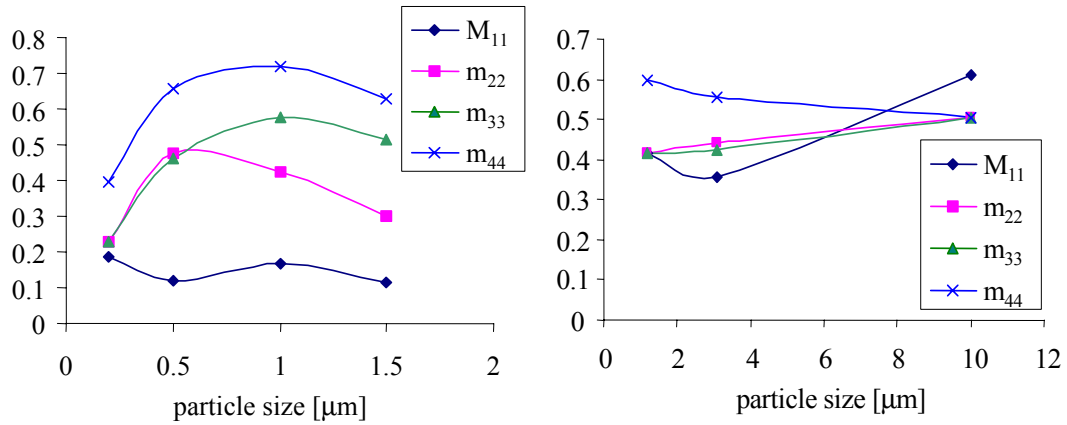
Figure 3.38. Magnitude S of the specular reflection peak as function of particle size for Silica (left) and Alumina (right).

Examining the volume scattering contribution, as shown in Fig. 3.39, one notices that the factor w, which measures the amount of light backscattered from the bulk is fairly independent of the particle size for both spherical Silica particles and polyhedral Alumina particles. The other diagonal elements, a, b, and c, vary significantly with the particle size.
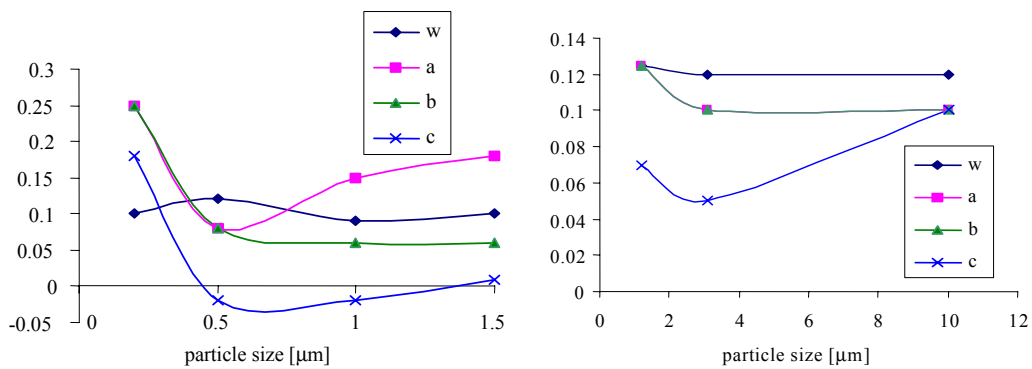
Figure 3.39. Volume scattering contribution as function of particle size for Silica (left) and Alumina (right).

152

Figures 3.40 and 3.41 show the base and the magnitude of the peak for the depolarization index D (formula 5) for Silica (left) and Alumina (right) particles. One can notice that the scattering system is strongly depolarizing the incident light for large angles (base - Fig. 3.40) confirming that the depolarization is mainly due to volume scattering. Fig. 3.40 also indicates significant differences among the depolarization levels corresponding to different particle sizes following the trend suggested by our physical model. One can also notice that the powder is not depolarizing as much for angles corresponding to the specular reflection peak (Fig. 3.41) because in this region the main contribution comes from surface scattering as described by the facet model. The magnitude of the peak is, however, fairly independent on the size of the particles indicating that there is a certain ratio between nondepolarizing surface scattering and the partially depolarizing volume scattering. It is believed that the difference in the peak magnitude between Silica and Alumina is related to the index of refraction of the particles.
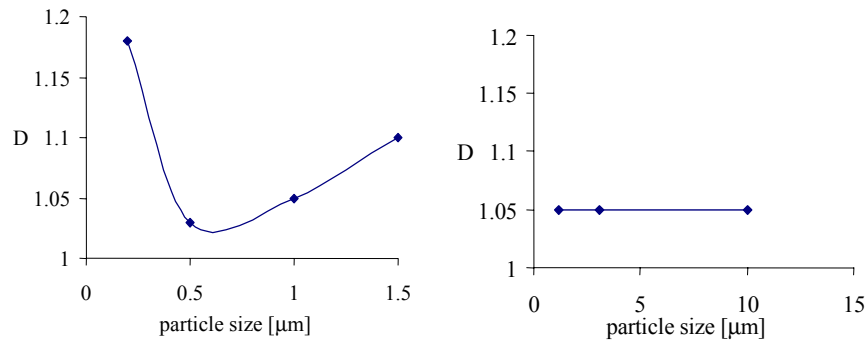
Figure 3.40. Base of the depolarization index D as function of particle size for Silica (left) and Alumina (right).
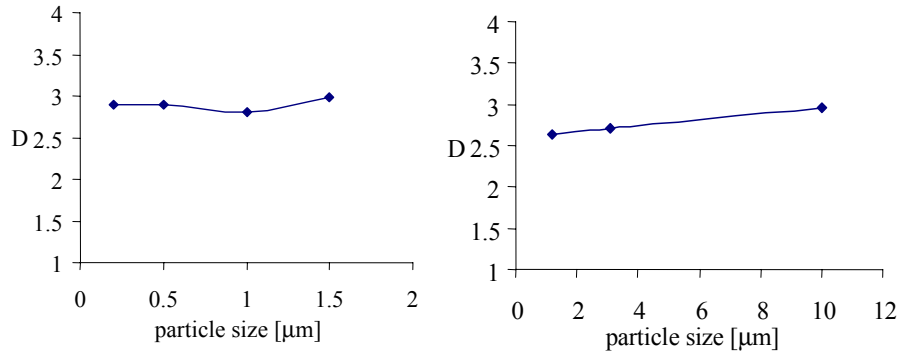
Figure 3.41. Peak magnitude of the depolarization index D as function of particle size for Silica (left) and Alumina (right).

Using the Mueller matrix formalism, a model was developed describing the light scattering depolarization effects that occur in backscattering from highly scattering media. The surface effects are accounted for by using a facet model in which the intensity profile depends on the correlation length and roughness of the surface. The volume effects are derived by considering the bulk as a system of closely packed independent particles where low-number scattering events are nondepolarizing. The model explains the main features observed experimentally for backscattering on compacted powders, but cannot explain the differences in the width of the specular reflection peak for the diagonal elements of the Mueller matrix. Also, some features observed in the off-diagonal elements of the matrix cannot be elucidated. Additional refinements, such as accounting specifically for low-number scattering events, are needed to completely describe the experimental results. This simple model has direct applications in characterization of optical coatings, paints and papers, remote sensing, and medical applications.

154

CHAPTER 4

SUMMARY OF ORIGINAL CONTRIBUTIONS AND CONCLUSIONS

Measuring the polarization of light is an important tool for investigating the interaction of light with matter. This dissertation presented theoretical and experimental studies of the polarimetric characteristics of random electromagnetic beams, and of the polarimetric signatures of different scattering systems. New experimental techniques were developed and used for studying various scattering regimes and configurations pertinent to random media characterization.

The basic concepts and notations of the Jones, Stokes-Mueller, polarization matrix, and cross-spectral density matrix formalisms, used for the description of random electromagnetic beams, the state of polarization, and the polarization transfer phenomenology were reviewed in the Introduction. A broad range of applications relying on polarimetry was also summarized.

Chapter 2 described four new techniques for polarimetric characterization of random electromagnetic beams and of the transfer of these beams through various systems. The degree of polarization rather than the full description of the state of polarization is of interest in multiple scattering regime. In such applications, the statistical nature and not the deterministic component of light bears relevant information. A new interferometric technique was developed for determining polarimetric characteristics of light governed by Gaussian statistics. Based on only two measurements of the contrast of the intensity

155

fluctuations in a Mach-Zehnder interferometric setup*, the method allows simultaneous determination of the degree of polarization and of the second normalized Stokes component. Since both outputs of the interferometer are used for measurements, another significant advantage is that no input light is wasted, as opposed to the case where polarizers are used. It was also shown that the signal-to-noise ratio can be increased using phase modulation in certain conditions. Using spatial light modulators it is possible to control the contrast and therefore the SNR in every point across the beam, a capability which should be of interest for applications involving the control of random electromagnetic beams.

In order to investigate the situations where the degree of polarization bears the relevant information one needs a light source with a controllable degree of polarization. Therefore, we developed a method for generating such complex random electromagnetic beams based on a Mach-Zehnder interferometer. For describing a random electromagnetic field one has to specify its spectral, coherence, and polarization properties. These properties are related to each other, and in general, they change on propagation. Optical beams are superposed in certain applications, and therefore, it is desirable to understand how these characteristics combine. The recently developed unified theory of coherence and polarization of random electromagnetic beams[8] provides a theoretical framework, namely the cross-spectral density matrix, for deriving the spectral density, the spectral degree of coherence and the spectral degree of polarization. As a direct application of this theory, it was shown in Chapter 2 that, under certain conditions, the spectral and the

---

* **M. Mujat**, **A. Dogariu**, and **G. S. Agarwal**, "Interferometric measurement of the degree of polarization and control of the contrast of intensity fluctuations", *Optics Letters* (in press)

polarimetric characteristics can be controlled by adjusting the correlation between parallel components of polarization propagating through the two arms of a Mach-Zehnder interferometer[*]. A novel light source with controllable spectral density and degree of polarization was demonstrated using phase modulators in a Mach-Zehnder interferometer illuminated with broadband unpolarized light.

The interferometric techniques discussed above for tuning and measuring the degree of polarization require a good understanding of how random electromagnetic beams are superposed. A closer examination of the interference of such beams lead to a second interferometric measurement technique that actually provides complete description of the state of polarization. A generalization of the laws of Fresnel and Arago was first developed[†] for the interference of electromagnetic beams with any state of coherence and polarization. It was found that one single formula and three generalized laws describe all possible cases of interference. As a direct application of this new generalized interference law, an original imaging polarimeter was proposed based on a modified Sagnac interferometer. Very good agreement with standard Stokes polarimetry is demonstrated[‡]. This measurement technique has, in certain situations, a significant advantage over the standard Stokes imaging polarimetry: one needs only one frame to obtain both the degree of polarization and the retardance, as opposed to least three images required in classical Stokes polarimetry. In this novel approach, orthogonal components of the polarization are projected along the

[*] **M. Mujat** and **A. Dogariu**, "Polarimetric and Spectral Changes in Random Electromagnetic Fields", Optics Letters **28**(22), p.2153-2155, 2003.

[†] **M. Mujat**, **A. Dogariu** and **E. Wolf**, "Generalized Interference Laws of Fresnel and Arago for Any State of Coherence and Polarization", *in preparation*

[‡] **M. Mujat**, **E. Baleine**, and **A. Dogariu**, "Interferometeric imaging polarimeter", *submitted to JOSA A*

same direction by a polarizer, and their interference is directly related to the degree of polarization of the analyzed light. An additional benefit is that the fringe spacing is easily adjustable allowing for tunable spatial resolution in determining the state of polarization, as opposed to previous interferometric techniques.

The measurement of the state of polarization is required for analyzing the polarization transfer through systems that alter it. The choice of the measurement technique is based on the particularities of the system to be investigated. An electronically agile device with no moving components and high sensitivity, simple and relatively inexpensive is generally desired. In the second part of Chapter 2, after a review of the current measurement techniques, two methods for performing Mueller polarimetry based on intensity measurements were presented. Practical considerations like calibration and optimization of Mueller polarimeters, as well as decomposition and noise filtering of Mueller matrices were also discussed.

The first method can be described as sequential generation - simultaneous analysis*. It allows simultaneous measurement of all four Stokes vector components. Four input states of polarization are sequentially produced and the Mueller matrix is obtained after measuring the corresponding four output states of polarization. In this original technique, there are no moving parts, which simplifies the mechanical setup and the control of the measurement process. The entire process (control of the polarization generation unit, measurement and analysis) is efficiently controlled in LabVIEW eliminating the need for lock-in amplifiers, sophisticated electronics and optics, high-voltage amplifiers and

---

* **M. Mujat** and **A. Dogariu**, "Real-time measurement of the polarization transfer function", Applied Optics **40**(1), p. 34-44, 2001

158

power supplies for electro-optic modulators. Through measurements on standard optical elements, an overall accuracy better than 2.5% was demonstrated. The ability to complete a Mueller matrix measurement in less than 50ms is appealing for monitoring structural dynamics in a variety of applications. The setup is designed to specifically investigate the polarization signature of particulate systems with high volume fractions.

The second method based on intensity measurements involves no time modulation of the retardance for any of the active elements in the Stokes generator or analyzer and it uses photomultipliers as detectors. The main advantage of this technique is that it provides a high dynamic range in measuring very low power optical signals typical for multiple scattering. In the experimental setup, the Stokes analyzer is mounted on a rotation stage and revolves around the sample, allowing the full measurement of the scattering matrix. A computer controls the Stokes generator, the counter, the rotation stage, and the data acquisition.

A practical aspect of Mueller polarimetry is selecting the optimal input Stokes vectors. Based on the maximization of the determinant of the transfer matrix, a novel procedure was developed* to minimize the effect of (i) power variations between the measurement of input and output states and (ii) fluctuations of the retardances introduced by the Stokes vector generator. An intuitive representation of the optimization procedure was described using the Poincarè sphere and an experimental validation was also presented. The analysis developed in Chapter 2 permits to estimate the expected error in measuring the Mueller

---

* **M. Mujat** and **A. Dogariu**, "Practical considerations on the design of Mueller polarimeters" - OSA Annual Meeting 2002, 29 Sep. - 03 Oct. 2002, Orlando, Florida USA.

matrix with a specific setup and can be used to optimize a measurement designed to attain a certain experimental precision.

The novel polarimetric techniques described in Chapter 2 were used for analyzing new effects in random media in several applications of practical interest. The polarimetric properties of various scattering systems were analyzed in Chapter 3, and they were then related to the structural properties of the global system, and to the size distribution, shape, orientation, birefringent or dichroic properties of the individual scatterers. The analysis was made in various scattering regimes, in forward and backward scattering configurations, or as function of the scattering angle.

A considerable number of reports exist in the literature which deal with experiments and theoretical calculations of light scattering from spherical particles. For most of the practical applications however, monodisperse ensembles of spherical particles are just idealized representations. The analysis presented in Chapter 3 elucidated some practical aspects of single and multiple scattering on polydisperse systems.

The experimental results were first presented for ensembles of spheres, a spray of droplets of water or solutions of fructose and galactose. The scattering matrix for a single sphere (or an ensemble of identical spheres) is a pure, non-depolarizing Mueller matrix. However, if the ensemble is polydisperse, even in the single scattering regime, the scattering matrix of the ensemble exhibits depolarization effects. This effect has not been previously addressed. It seems to be generally accepted that depolarization effects can only be associated to multiple scattering. However, our analysis proved that depolarization also occurs in single scattering on polydisperse spherical particles. This

could be easily explained considering that along a certain observation direction particles with different diameters scatter light differently and the detector records an ensemble of pure states of polarization that is equivalent to partially polarized light.

Another case of practical interest investigated in Chapter 3 was the polarization transfer through systems consisting of individual layers of partially aligned fibers not previously addressed. The analysis aimed at describing the polarizing behavior observed for partially oriented cylinders. It was demonstrated that a certain degree of alignment has the effect of a partial polarizer and the efficiency of this polarizer depends on the degree of alignment and of the packing fraction of the system[*]. This polarizing effect is generated by the shape anisotropy of the fibers in combination with their partial alignment.

In specific applications such as long range target identification, it is important to know what type of polarization is better preserved during propagation through atmosphere. Previous studies investigated the depolarization effects for specific types of input state of polarization. These results can be easily derived from our analysis of the Mueller matrix[†]. The Mueller matrix associated with particulate systems of various optical densities was measured in transmission. The measurements demonstrate that for small spherical particles, as compared with the wavelength of light, linear polarization is better preserved than circular polarization as light propagates through turbulent media. For large particles, the situation is reversed, circular polarization is better preserved than the linear component.

[*] **M. Mujat** and **A. Dogariu**, "Measurements of structure-induced polarization features in forward scattering from collections of cylindrical fibers", J. Quant. Spectrosc. Radiat. Transfer **70**(4-6), p.555-567, 2001.

[†] **M. Mujat** and **A. Dogariu**, "Real-time Mueller matrix measurement for particulate systems", in *Laser Radar Technology and Applications V*, G. W. Kamerman, U. N. Singh, C. Werner, and V. V. Molebny, eds., Proc. SPIE **4035**, p. 390-400, 2000.

It was also demonstrated here that this is not true for polyhedral or cylindrical particles, that behave differently. These effects need to be considered in remote sensing and long range communications.

Optical activity measurements have been performed for a long time on homogeneous materials. However, for medical applications and remote sensing of biological media it is imperative to understand and quantify the effect of optical activity in multiple scattering regime. The analysis[*] presented in Chapter 3 shows that the output state of polarization depends not only on the optical density of the scattering medium, but it is also strongly influenced by the optical rotatory power and the amount of circular dichroism associated to the scattering medium. It was shown that in the circular birefringence case, the scattering and optical activity work together in strongly depolarizing the light, while in the dichroic case the two effects compete with each other resulting in a preservation of the degree of polarization due to optical activity.

Light scattering from dense scattering media is of interest in material sciences including the characterization of paints, papers, and rough surfaces, as well as in remote sensing and various noninvasive medical investigation techniques. There are many theoretical models and numerical procedures used for analyzing the polarized scattering pattern from rough surfaces and multiply-scattering media, but they are in general computational extensive and time consuming. A simple and intuitive model to characterize dense scattering media[†] was proposed in Chapter 3. In this model, scattering was split into

[*] **M. Mujat** and **A. Dogariu**, "Light scattering in granular chiral media" - OSA Annual Meeting 2001, October 14-18, 2001, Long Beach, California USA.

[†] **M. Mujat**, **A. Spier** and **A. Dogariu**, "Polarimetric signature of dense scattering media", in *Polarization Science and Remote Sensing*, J. A. Shaw, J. S. Tyo, eds., Proc. SPIE **5158**, p.217-225, 2003.

a surface and a volume component, which were examined by using the Mueller matrix formalism. The nondepolarizing surface contribution was interpreted using a facet model, while the depolarizing volume effects were explained by considering the system to consist of closely packed independent particles and accounting for nondepolarizing low-order scattering events.

This dissertation presented novel theoretical and experimental contributions to polarimetric characterization of random electromagnetic beams, and random media. Innovative experimental techniques were developed and used for studying various scattering systems which are relevant for applications in biology, medicine, material sciences, and remote sensing.

APPENDIX A

PUBLICATIONS AND CONFERENCES

A 1. Referred publications

1. M. Mujat, A. Dogariu and E. Wolf, "Generalized Interference Laws of Fresnel and Arago for Any State of Coherence and Polarization", in preparation.

2. M. Mujat, E. Baleine, and A. Dogariu, "Interferometric imaging polarimeter", submitted to JOSA A.

3. M. Mujat, A. Dogariu, and G. S. Agarwal, "Interferometric measurement of the degree of polarization and control of the contrast of intensity fluctuations", Opt. Lett (in press).

4. M. Mujat, and A. Dogariu, "Polarimetric and Spectral Changes in Random Electromagnetic Fields", Opt. Lett. **28**(22), 2153-2155 (2003).

5. M. Mujat, and A. Dogariu, "Real-time measurement of the polarization transfer function", Appl. Opt. **40**(1), 34-44 (2001).

6. M. Mujat, and A. Dogariu, "Measurements of structure-induced polarization features in forward scattering from collections of cylindrical fibers", J. Quant. Spectrosc. Radiat. Transfer **70**(4-6), 555-567 (2001).

A 2. Proceedings

7. M. Mujat, A. Spier and A. Dogariu, "Polarimetric signature of dense scattering media", in *Polarization Science and Remote Sensing*, J. A. Shaw, J. S. Tyo, eds., Proc. SPIE **5158**, 217-225 (2003).

8. M. Mujat, and A. Dogariu, "Real-time Mueller matrix measurement for particulate systems", in *Laser Radar Technology and Applications V*, G. W. Kamerman, U. N. Singh, C. Werner, and V. V. Molebny, eds., Proc. SPIE **4035**, 390-400 (2000).

A 3. Conferences

1. M. Mujat, A. Dogariu and E. Wolf, "Polarimetric and Spectral Changes in Random Electromagnetic Fields" - OSA Annual Meeting 2003, October 5-9, 2003, Tucson, Arizona USA.

2. M. Mujat, A. Spier and A. Dogariu, "Polarimetric signature of dense scattering media" - SPIE Annual Meeting 2003, August 3-8, 2003, San Diego, California USA.

3. M. Mujat and A. Dogariu, "Practical considerations on the design of Mueller polarimeters" - OSA Annual Meeting 2002, September 29 - October 03, 2002, Orlando, Florida USA.

4. M. Mujat and A. Dogariu, "Light scattering in granular chiral media" - OSA Annual Meeting 2001, October 14-18, 2001, Long Beach, California USA.

5. M. Mujat and A. Dogariu, "Measurements of structure-induced polarization features in forward scattering from collections of cylindrical fibers" - Fifth International Conference on Light Scattering by Nonspherical Particles, August 21- September 1, 2000, Halifax, Canada.

6. M. Mujat and A. Dogariu, "Real-time Mueller matrix measurement for particulate systems", Aerosense 2000, April 24 - 28, 2000, Orlando, Florida USA.
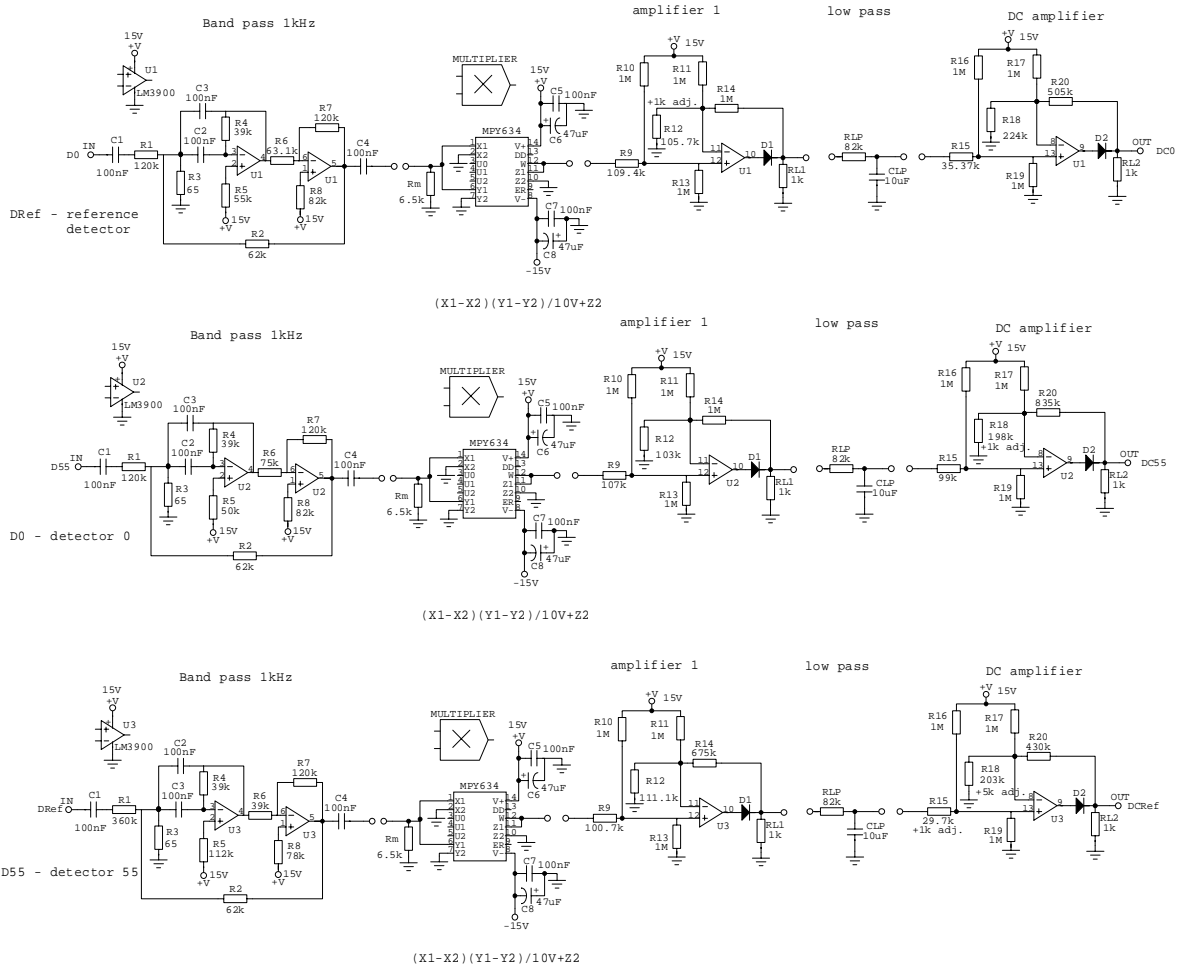
APPENDIX B
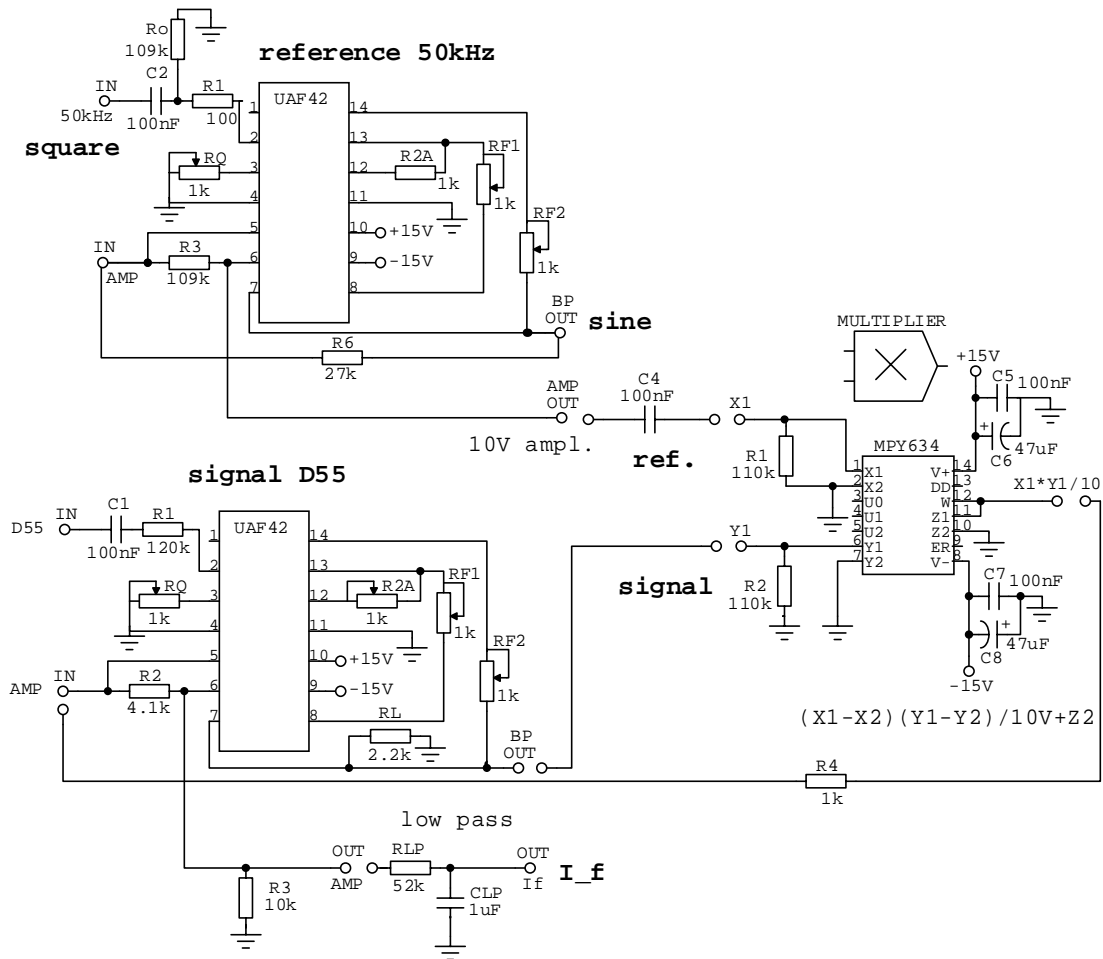# ELECTRONIC BLUEPRINTS
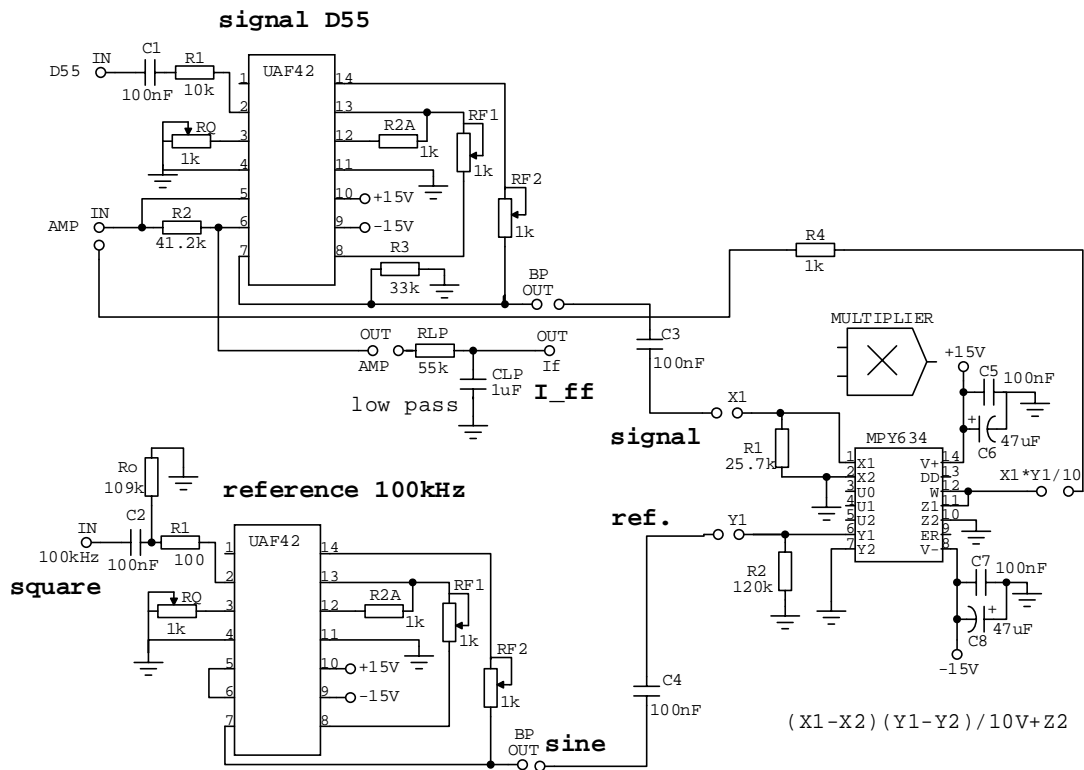
Figure B1. DC channels.

Figure B2. 50kHz channel.

Figure B3. 100kHz channel.

LIST OF REFERENCES

[1] D. F. J. Arago and A. J. Fresnel, "On the action of rays of polarized light upon each other", Annales de Chimie et de Physique, p. 288, (1819), republished in *The wave theory of light. Memoires by Huygens, Young and Fresnel*, edited by Henry Crew, (American Book Company, New York 1900).

[2] G. C. Stokes, "On the composition and resolution of streams of polarized light from different sources", Trans. Cambridge Philos. Soc. **9**, 399-416 (1852).

[3] R. C. Jones, "A new calculus for the treatment of optical systems", J.Opt.Soc.Am. **31**, 488-493 (1941); **32**, 486-493 (1942); **37**, 107-110 (1947).

[4] H. Mueller, "The Foundations of Optics", J.Opt.Soc.Am. **38**, 661 (1948).

[5] M. Born and E. Wolf, *Principles of Optics* (Cambridge University Press, Cambridge, 7th ed., 1999).

[6] N. Wiener, "Generalized harmonic analysis", Acta. Math. **55**, 119-260 (1930).

[7] E. Wolf, "Optics in terms of observable quantities", Nuovo Cimento **12**, 884-888 (1954).

[8] E. Wolf, "Unified Theory of Coherence and Polarization of Random Electromagnetic Beams", Phys. Lett. A. **312** 263-267 (2003) .

[9] H. C. van de Hulst, *Light Scattering by Small Particles* (Dover Publications, Inc., New York 1981).

[10] W. A. Shurcliff, *Polarized Light*, (Harvard University Press, Cambridge 1966).

[11] C. Brosseau, *Fundamentals of Polarized Light, A Statistical Optics Approach* (John Wiley&Sons, Inc., New York 1998).

[12] C. F. Bohren and D. R. Huffman, *Absorption and Scattering of Light by Small Particles* (Wiley, New York 1983).

[13] J. Cariou, B. L. Jeune, J. Lotrian, Y. Guern, "Polarization effects of seawater and underwater targets", Appl. Opt. **29**(11), 1689-1695 (1990).

[14] R. M. A. Azzam, N. M. Bashara, *Ellipsometry and Polarized Light*, (North-Holland Publishing Company, Amsterdam 1997).

[15] W. S. Bickel, M. E. Stafford, "Biological particles as irregularly shaped particles" in *Light Scattering by Irregularly Shaped Particles*, D. Schuerman, Plenum, New York, 299-305 (1980).

170

[16] G. C. Salzman, C. T. Gregg, W. K. Grace, R. D. Hiebert, "Biological particle identification apparatus", U.S.Patent **4884886**, December 5, 1989.

[17] B. DeVolk, F. Allen, C. D. Newman, R. J. Frastz, "Particle identifying apparatus", U.S. Patent **4953980**, September 4, 1990.

[18] J. M. Bueno and P. Artal, "Double-pass imaging polarimetry in the human eye", Opt. Lett. **24**(1), 64-66 (1999).

[19] J. E. Bille, "Ellipsometer", U.S. Patent **5822035**, October 13, 1998.

[20] A. H. Hielscher, A. A. Eick, J. R. Mourant, D. Shen, J. P. Freyer, and I. J. Biggio, "Diffuse backscattering Mueller matrices of highly scattering media", Opt. Expr. **1**(13), 441-453 (1997).

[21] B. V. Bronk, S. D. Druger, J. Czege, and W. P. Van de Merwe, "Measuring Diameters of Rod-Shaped Bacteria in Vivo with Polarized Light Scattering", Biophys. J. **69**, 1170-1177 (1995).

[22] D. B. Shapiro, P. G. Hull, A. J. Hunt, and J. E. Hearst, "Calculations of the Mueller scattering matrix for a DNA plectonemic helix", J. Chem. Phys. **101**(5), 4214-4221 (1994).

[23] M. S. Quinby-Hunt, P. G. Hull, and A. J. Hunt, Chapter 18 in *Light Scattering by Nonspherical Particles; Theory, Measurement and Applications*, M. I. Mishchenko, J. W. Hovenier, L. D. Travis, (Academic Press, San Diego 2000).

[24] Y. A. Kadyshevich, Y. S. Lyubotseva, I. N. Plakhina, "Measurements of matrices for light scattered by sea water", Izv. Acad. Sci. USSR Atmos. Ocean. Phys. **7**, 367-371 (1971).

[25] A. Kouzoubov, M. J. Brennan, and J. C. Thomas, "Treatment of polarization in laser remote sensing of ocean water", Appl. Opt. **37**(18), 3873-3885 (1998).

[26] A. Onuki, M. Doi, "Flow birefringence and dichroism of polymers. I General theory and application to the dilute case", J. Chem. Phys. **85**(2), 1190-1197 (1986).

[27] Y. Shindo, "Application of polarized modulation technique in polymer science", Opt. Eng. **34**(12), 3369-3384 (1995).

[28] R. Walraven, "Polarization imagery", Opt. Eng. **20**(1), 14-18 (1981).

[29] G. W. Katawar, "Virtues of Mueller matrix detection of objects embeded in random media", in *Laser-Tissue Interaction XI: Photochemical, Photothermal, and Photomechanical*, D. D. Duncan, J. O. Hollinger, S. L. Jacques eds., Proc. SPIE **3914**, 478-488 (2000).

[30] P. Gerligand, M. H. Smith, R. A. Chipman, "Polarimetric images of a cone", Opt. Expr. **4**(10), 420-430 (1999).

171

[31] J. D. Howe, M. A. Miller, R. V. Blumer, T. E. Petty, M. A. Stevens, D. M. Teale, M. H. Smith, "Polarization sensing for target acquisition and mine detection", in *Polarization Analysis, Measurement, and Remote Sensing III*; D. B. Chenault, M. J. Duggin, W. G. Egan, D. H. Goldstein, eds., Proc. SPIE **4133**, 202-213 (2000).

[32] B. W. Bell, "Mueller matrix: an experimental and analytical tool for magneto-optics", Opt. Eng. **28**(2), 114-119 (1989).

[33] K. Oka, T. Yamaguchi, Y. Ohtsuka, "Spatiotemporal Strain Distribution Mapping Using Novel Optical Heterodyne Polarimeter", in *Polarization Analysis and Measurement II*; D. H. Goldstein, D. B. Chenault, eds., Proc. SPIE **2265**, 40-47, (1994).

[34] L. Mandel and E. Wolf, *Optical Coherence and Quantum Optics* (Cambridge, Cambridge University Press, 1995).

[35] K. Kim, L. Mandel, and E. Wolf, "Relationship between Jones and Mueller matrices for random media", J.Opt.Soc.Am. A **4(3)**, 433-437 (1987).

[36] A. R. Hill, B. D. Cameron, J. R. Chung, J. S. Baba, G. L. Cote, "Development and calibratin of an automated Mueller matrix polarimeter system for skin lession differentiation", in *Optical Tomography and Spectroscopy of Tissues IV*, B. Chamce, R. R. Alfano, B. J. Tromberg, M. Tamura, E. M. Sevick-Muraca, eds., Proc. SPIE **4250**, 449-454 (2001).

[37] S. L. Jacques, "Video imaging of superficial biological tissue layers using polarized light", US Patent **6,177,984**, January 23, 2001.

[38] M. H. Smith, P. Burke, A. Lompado, E. Tanner, L. W. Hillman, "Mueller matrix imaging polarimetry in dermatology", in *Biomedical Diagnostic, Guidance, and Surgical-Assist Systems II*, T. Vo-Dinh, W. S. Grundfest, D. A. Benaron, eds., Proc. SPIE **3911**, 210-216 (2000).

[39] M. H. Smith, "Interpreting Mueller matrix images of tissues", in *Laser-Tissue Interaction X1I*, D. Duncan, S. Jacques, P. Johnson, eds., Proc. SPIE **4257**, 82-89 (2001).

[40] J. F. Federici, N. Guzelsu, H. C. Lim, G. Jannuzzi, T. Findley, H. R. Chaudhry, A. B. Ritter, "Noninvasive Light-Reflection Technique for Measuring Soft-Tissue Stretch", Appl. Opt. **38**(31), 6653-6660 (1999).

[41] M. O'Donnell, A. Skovoroda, B. Shapo, S. Emelianov, "Internal Displacement and Strain Imaging using Ultrasonic Speckle Tracking", IEEE Trans. Ultrason. Ferroelect. Freq. Cont. **41**, 314-325 (1994).

[42] K. R. Denninghoff, M. H. Smith, L. Hillman, "Retinal Imaging Techniques in Diabetes", Diabetes Technology & Therapeutics **2**(1), 111-113 (2000).

172

[43] A. Lompado, M. H. Smith, and V. Krishnaswamy, "Measurement of the transmission and reflection Mueller matrices of a thin blood column", in *Optical Diagnostics and Sensing of Biological Fluids and Glucose and Cholesterol Monitoring*, A.V. Priezzhev, G. L. Cote, eds., Proc. SPIE **4263**, 161-169 (2001).

[44] S. Jiao, L. V. Wang, "Two-dimentional depth-resolved Mueller matrix of biological tissue measured with double-beam polarization-sensitive optical coherence tomography", Opt. Lett. **27**(2), 101-103 (2002).

[45] B. D. Cameron, G. L. Cote, "Polarimetric Detection of Gloucose in Biological Based Fluids", in *Optical Diagnostics of Biological Fluids and Advanced Techniques in Analytical Cytology*, A. V. Priezzhev, T. Asakura, R. C. Leif, eds., Proc. SPIE **2982**, 308-313 (1994).

[46] R. O. Esenaliev, K. V. Larin, I. V. Larina, M. Motamedi, "Noninvasive monitoring of glucose concentration with optical coherence tomography", Opt. Lett. **26**(13), 992-994 (2001).

[47] A. A. Kokhanovsky, "Radiative transfer in chiral random media", Phys. Rev. E **60**(4), 4899-4907 (1999).

[48] A. Diaspro, G. Radicchi, C. Nicolini, "Polarized Light Scattering: A Biophysical Method for Studying Bacterial Cells", IEEE Trans. Biomed. Engr. **42**(10), 1038-1043 (1995).

[49] W. S. Bickel, M. E. Stafford, "Polarized light scattering from biological systems: A technique for cell differentiation", J. Biol. Phys. **9**, 53-81 (1981).

[50] J. E. Solomon, "Polarization imaging", Appl. Opt. **20**(9), 1537-1544 (1981).

[51] J. S. Tyo, M. P. Rowe, E. N. Pugh, Jr., and N. Engheta, "Target detection in optically scattering media by polarization-difference imaging", Appl. Opt. **35**(11), 1855-1870 (1996).

[52] J. W. Hovenier, H. C. van de Hulst, C. V. M. van de Mee, "Conditions for the elements of the scattering matrix", Astron. Astrophys. **157**, 301-310 (1986).

[53] A. P. Bates, K. I. Hopcraft, E. Jakeman, "Particle shape determination from polarization fluctuatins of scattered radiation", J. Opt. Soc. Am. A. **14**(12), 3372-3378 (1997).

[54] F. Delplancke, "Automated high-speed Mueller matrix scatterometer", Appl. Opt. **36**(22), 5388-5395 (1997).

[55] M. P. Silverman, W. Strange, J. Badoz, I. A. Vitkin, "Enhanced optical rotation and diminished depolarization in diffusive scattering from a chiral liquid", Opt. Com. **132**, 410-416 (1996).

[56] B. Kaplan, E. Compain, B. Drevillon, "Phase-modulated Mueller ellipsometry characterization of scattering by latex sphere suspensions", Appl. Opt. **39**(4), 629-636 (2000).

[57] R. A. Chipman, E. A. Sorsin, J. L. Pezzaniti, "Mueller matrix imaging polarimetry: An overview", in *Polarization Analysis and Applications to Device Technology*, T. Yoshizawa, H. Yokota, eds., Proc. SPIE **2873**, 5-12 (1996).

[58] M. H. Smith, E. A. Sorsin, T. J. Tayag, R. A. Chipman, "Mueller matrix imaging of GaAs/AlGaAs self-imaging beamsplitting waveguides", in *Polarization: Measurement, Analysis, and Remote Sensing*, D. H. Goldstein, R. A. Chipman, eds., Proc. SPIE **3121**, 47-54 (1997).

[59] S. Krishnan, P. C. Nordine, "Fast ellipsometry and Mueller-matrix ellipsometry using the division-of-amplitude photopolarimeter", in *Polarization Analysis and Applications to Device Technology*, T. Yoshizawa, H. Yokota, eds., Proc. SPIE **2873**, 152-156 (1996).

[60] S. Krishnan, K. J. Yugawa, P. C. Nordine, "Optical properties of Liquid metals Studied by Spectroscopic Ellipsometry", in *Polarization Analysis and Applications to Device Technology*, T. Yoshizawa, H. Yokota, eds., Proc. SPIE **2873**, 314-315 (1996).

[61] D. L. Jordan, G. D. Lewis, E. Jakeman, "Emission polarization of roughened glass and aluminum surfaces", Appl. Opt. **35**(19), 3583-3590 (1996).

[62] J. H. Rommers, J. Howard, "A new scheme for heterodyne polarimetry with high temporal resolution", Plasma Phys. Control. Fusion **38**, 1805-1816 (1996).

[63] J. M. Schmitt, A. H. Gandjakhche, R. F. Bonner, "Use of polarized light to discriminate short-path photons in a multiply scattering medium", Appl. Opt. **31**(30), 6535-6546 (1992).

[64] K. Shimuzu, A. Ishimaru, L. Reynolds, A. P. Bruckner, "Backscattering of a picosecond pulse from densely distributed scatterers", Appl. Opt. **18**, 3484-3488 (1979).

[65] J. C. Hebden, R. A. Kruger, K. S. Wong, "Time-resolved imaging through a highly scattering medium", Appl. Opt. **30**, 788-794 (1991).

[66] M. Toida, M. Kondo, T. Ichimura, H. Inaba, "Two-dimensional coherent detection imaging in multiple scattering media based on the directional resolution capability of the optical heterodyne method", Appl. Phys. B. **52**, 391-394 (1991).

[67] K. M. Yoo, Q. R. Xing, R. R. Alfano, "Imaging objects hidden in highly scattering media using femtosecond second-harmonic-generation cross-correlation time gating", Opt. Lett. **16**, 1019-1021 (1991).

[68] M. Mujat, and A. Dogariu, "Polarimetric and Spectral Changes in Random Electromagnetic Fields", Opt. Lett. **28**(22), 2153-2155 (2003).

174

[69] D. Bicout, C. Brosseau, A. S. Martinez, J. M. Schmitt, "Depolarization of multiply scattered waves by spherical diffusers: Influence of the size parameter", Phys. Rev. E **49**(2), 1767-1770 (1994).

[70] D. F. V. James, "Change of polarization of light beams on propagation in free space", J. Opt. Soc. Am. A **11**(5), 1641-1643 (1994).

[71] G. Gbur, and D. F. V. James, "Unpolarized sources that generate highly polarized fields outside the source", J. Mod. Opt. **47**(7), 1171-1177 (2000).

[72] F. Gori, M. Santarsiero, G. Piquero, R. Borghi, A. Mondello, and R. Simon, "Partially polarized Gaussian Schell-model beams", J. Opt. A **3**, 1-9 (2001).

[73] E. Collett, *Polarized Light, Fundamentals and applications*, (New York, Marcel Dekker, Inc. 1993).

[74] E. Wolf, "Invariance of the Spectrum of Light on Propagation", Phys. Rev. Lett. **56**(13), 1370 (1986).

[75] A. Dogariu and E. Wolf, "Coherence theory of pairs of correlated wave fields", J. Mod. Opt. **50**(11), 1791-1796 (2003).

[76] L. Mandel and E. Wolf, *Optical Coherence and Quantum Optics*, Section 4.7.2, (Cambridge University, Cambridge, 1995).

[77] S. T. Wu, D. K. Yang, *Reflective Liquid Crystal Displays*, (Wiley, New York, 2001).

[78] R. Hanau, "Interference of Linearly Polarized Light with Perpendicular Polarizations", Amer. J. Phys. **31**, 303-304 (1963).

[79] E. Collett, "Mathematical Formulation of the Interference Laws of Fresnel and Arago", Amer. J. Phys. **39**, 1483-1495 (1971), and E. Collett, *Polarized Light, Fundamentals and applications*, (New York, Marcel Dekker, Inc. 1993).

[80] G. Parrent and P. Roman, "On the Matrix Formulation of the Theory of Partial Polarization in Terms of Observables", Il Nuovo Cimento **10**, 370-388 (1960).

[81] E. Wolf, "Coherence Properties of Partially Polarized Electromagnetic Radiation", Il Nuovo Cimento **13**, 1165-1181 (1959).

[82] R. M. A. Azzam, "Photopolarimetric measurement of the Muelle matrix by Fourier analysis of a single detected signal", Opt. Lett. **2**(6), 148-150 (1978).

[83] J. L. Pezzaniti, R. A. Chipman, "Mueller matrix imaging polarimetry", Opt. Eng. **34**, 1558-1568 (1995).

[84] B. D. Cameron, M. J. Rakovic, M. Mehrubeoglu, G. W. Kattawar, S. Rastegar, L. V. Wang, G. L. Cote, "Measurement and calculation of the two-dimensional backscattering Mueller matrix of a turbid medium", Opt. Lett. **23**, 485-487 (1998).

175

[85] A. H. Hielscher, A. A. Eick, J. R. Mourant, D. Shen, J. P. Freyer, and I. J. Bigio, "Diffuse backscattering Mueller matrices of highly scattering media", Opt. Exp. **1**, 441-453 (1997).

[86] J. L. Pezzaniti, J. M. Lindberg, "Apparatus and process for the noninvasive measurement of optically active compounds", US Patent **5,788,632**, August 4, 1998.

[87] J. D. Barter, P. H. Lee, H. R. Thompson, T. G. Schneider , "Stokes Parameter Imaging of Scattering Surfaces", in *Polarization: Measurement, Analysis, and Remote Sensing*, D. H. Goldstein, R. A. Chipman, eds., Proc. SPIE **3121**, 314-320 (1997).

[88] J. D. Barter, "Visible Stokes polarimetric imager", US Patent **6,122,404**, September 19, 2000.

[89] M. Mujat, A. Dogariu, "Real-time Mueller matrix measurement for particulate systems", in *Laser Radar Technology and Applications V*, G. W. Kamerman, U. N. Singh, C. Werner, V. V. Molebny, eds., Proc. SPIE **4035**, 390-400 (2000).

[90] K. Oka, T. Kaneko, "Compact complete imaging polarimeter using birefringent wedge prisms", Opt. Expr. **11**(13), 1510-1519 (2003).

[91] E. Collett, "Measurement of the four Stokes polarization parameters with a single circular polarizer", Opt. Commun. **52**(2), 77-80 (1996).

[92] A. Ambirajan, D. C. Look, "Experimental investigation of the multiple scattering of a polarized laser beam", J. of Thermophysics and Heat Transfer **12**(2), 153-163 (1998).

[93] W. S. Bickel, W. M. Bailey, "Stokes vectors, Mueller matrices, and polarized scattered light", Am.J.Phys. **53**(5), 468-478 (1985).

[94] W. M. McClain, W. Jeng, B. Pati, Y. Shi, D. Tian, "Measurement of the Mueller scattering matrix by use of optical beats from a Zeeman laser", Appl. Opt. **33**(7), 1230-1241 (1994).

[95] D. H. Goldstein, "Infrared laser polarimeter", U.S. Patent **5247176**, September 21, 1993.

[96] R. M. A. Azzam, "Polarimeter", U.S. Patent **4306809**, December 22, 1981.

[97] Z. Sekera, "Light Scattering in the Atmosphere and the Polarization of Sky Light", J.Opt.Soc.Am. **47**(6), 484-490 (1957).

[98] G. D. Lewis, D. L. Jordan, "Backscattering Mueller Matrices from Bead-Blasted Aluminum Surfaces", in *Polarization: measurement, analysis, and remote sensing*, D. H. Goldstein, R. A. Chipman, eds., Proc. SPIE **3121**, 434-443 (1997).

[99] G. D. Lewis, D. L. Jordan, E. Jakeman, "Backscatter linear and circular polarization analysis of roughened aluminum", Appl. Opt. **37**(25), 5985-5992 (1998).

[100] R. M. A. Azzam, "Division-of-amplitude photopolarimeter (DOAP) for the simultaneous measurement of all four Stokes parameters of light", Optica Acta **29**(5), 685-689 (1982).

[101] R. M. A. Azzam, "Photodetector arrangement for measuring the state of polarization of light", U.S. Patent **4681450**, July 21, 1987.

[102] A. M. El-Saba, R. M. A. Azzam, M. A. G.Abushagur, "Performance optimization and light-beam-deviation analysis of the parallel-slab division-of-amplitude photopolarimeter", Appl. Opt. **38**(13), 2829-2836 (1999).

[103] S. Krishnan, P. C. Nordine, "Mueller matrix ellipsometry using the division-of-amplitude photopolarimeter: a study of depolarization effects", Appl. Opt. **33**(19), 4184-4192 (1994).

[104] S. Jasperson, S. E. Schnatterly, "An Improved Method for high Reflectivity Ellipsometry Based on a New Modulation Technique", Rev. Sci. Instrum. **40**, 761-767 (1969).

[105] A. J. Hunt, D. R. Huffman, "A new polarization-modulated light scattering instrument", Rev. Sci. Instrum. **44**(12), 1753-1762 (1973).

[106] R. Anderson, "Measurement of Mueller matrices", Appl. Opt. **31**(1), 11-13 (1992).

[107] G. E. Jellison, F. A. Modine, "Two modulator generalized ellipsometer for complete Mueller matrix measurement", U.S. Patent **5956147**, September 21, 1999.

[108] R. C. Thompson, J. R. Bottiger, E. S. Fry, "Measurement of polarized light interactions via the Mueller matrix", Appl. Opt. **19**(8), 1323-1332 (1980).

[109] E. Compain, B. Drevillon, "Complete high-frequency measurement of Mueller matrices based on a new coupled-phase modulator", Rev. Sci. Instrum. **68**(7), 2671-2680 (1997).

[110] E. Compain, B. Drevillon, J. Huc, J. Y. Parey, J. E. Bouree, "Complete Mueller matrix measurement with a single high frequency modulation", Thin Solid Films **313**, 47-52 (1998).

[111] E. Compain, B. Drevillon, "High-frequency modulation of the four states of polarization of light with a single phase modulator", Rev. Sci. Instrum. **69**(4), 1574-1580 (1998).

[112] E. Compain, B. Drevillon, "Broadband division-of-amplitude polarimeter based on uncoated prisms", Appl. Opt. **37**(25), 5938-5944 (1998).

177

[113] B. Kaplan, E. Compain, B. Drevillon, "Scattering - Phase-modulated Mueller ellipsometry characterization of scattering by latex sphere suspensions", Appl. Opt. **39**(4), 629-636 (2000).

[114] F. L. Roy-Brehonnet, B. L. Jeune, P. Elies, J. Cariou, J. Lotrian, "Optical media characterization by Mueller matrix decomposition", J.Phys. D: Appl. Phys. **29**, 34-38 (1996).

[115] R. M. A. Azzam, I. M. Eliminyawi, and A. M. El-Saba, "General-analysis and optimization of the 4-detector photopolarimeter", J. Opt. Soc. Am. A. **5**(5), 681-689 (1988).

[116] R. M. A. Azzam and K. A. Giardina, "Photopolarimeter based on planar grating diffraction", J. Opt. Soc. Am. A **10**(6), 1190-1196 (1993).

[117] K. Brudzewski, "Static Stokes ellipsometer - General-analysis and optimization", J. Mod. Opt. **38**(5), 889-896 (1991).

[118] A. Ambirajan and D. C. Look, "Optimum angles for a polarimeter.1 and 2", Opt. Eng. **34** (6), 1651-1655 and 1656-1658 (1995).

[119] D. S. Sabatke, M. R. Descour, E. L. Dereniak, W. C. Sweatt, S. A. Kemme, and G. S. Phipps, "Optimization of retardance for a complete Stokes polarimeter", Opt. Lett. **25**(11), 802-804 (2000).

[120] I. C. Khoo and S. T. Wu, *Optics and Nonlinear Optics of Liquid Crystals* (World Scientific, Singapore 1993).

[121] G. G. Fuller, *Optical Rheometry of Complex Fluids*, (Oxford University Press, New York, 1995).

[122] See for example the references for Chapters 9, 10 and 11 in H. C. van de Hulst, *Light Scattering by Small Particles*, (Dover, New York, 1981).

[123] M. I. Mishchenko, L. D. Travis, A. Macke, "T-Matrix Method and Its Applications" Chapter 6 in *Light Scattering by Nonspherical Particles; Theory, Measurement and Applications*, M. I. Mishchenko, J. W. Hovenier, L. D. Travis, (Academic Press, San Diego 2000).

[124] G. Mie, "Beiträge zur Optik trüber Medien, speziell Koloidaler Metalösungen", Ann. Phys. **25**, 377-445 (1908).

[125] F. Perrin, "Polarization of light scattered by isotropic opalescent media", J. Chem. Phys. **10**, 415-427 (1942).

[126] J. W. Hovenier, D. W. Mackowski, "Symmetry relations for forward and backward scattering by randomly oriented particles", J. Quant. Spectrosc. Radiat. Transfer. **60**(3), 483–492 (1998).

[127] M. S. Patterson, B. Chance, B. C. Wilson, "Time resolved reflectance and transmittance for the noninvasive measurement of tissue optical properties", Appl. Opt. **28**(12), 2331-2336 (1989).

[128] T. A. Germer, M. E. Nadal, "Modeling the appearance of special effect pigment coatings", in *Surface Scattering and Diffraction for Advanced Metrology*, Z. Gu, A. A. Maradudin, eds., Proc. SPIE **4447**, 77-86 (2001).

[129] T. A. Germer, C. C. Asmail, "Polarization of light scattered by microrough surfaces and subsurface defects", J. Opt. Soc. Am. **16**(6), 1326-1332 (1999).

[130] T. A. Germer, "Polarized light scattered by microroughness and small defects in dielectric layers", J. Opt. Soc. Am. **18**(6), 1279-1288 (2001).

[131] A. Sentenac, H. Giovannini, M. Saillard, "Scattering from rough inhomogeneous media: splitting of surface and volume scattering", J. Opt. Soc. Am. **19**(4), 727-736 (2002).

[132] J. Ellis, P. Caillard, A. Dogariu, "Off-diagonal Mueller matrix elements in backscattering from highly diffusive media", J. Opt. Soc. Am. **19**(1), 43-48 (2002).

[133] A. Dogariu, G. D. Boreman, "Facet model for photon-flux transmission through rough dielectric interfaces", Opt. Lett. **21**(10), 701-703 (1996).

[134] G. D. Lewis, D. L. Jordan, Eric Jakeman, "Backscatter linear and circular polarization analysis of roughened aluminum", Appl. Opt. **37**(25), 5985-5992 (1998).

[135] C. Lam, A. Ishimaru, "Mueller matrix representation of a slab of random medium with discrete particles and random rough surfaces with moderate surface roughness", Math. Gen. **260**, 111-125 (1993).

[136] J. M. Elson, "Theory of light scattering from a rough surface with an inhomogeneous dielectric permittivity", Phys. Rev. B **30**, 5460-5480 (1984).

[137] G. Pelosi, R. Coccioli, "A finite element approach for scattering from inhomogeneous media with a rough interface", Waves Random Media **7**, 119-127 (1997).

[138] D. W. Mueller, A. L. Crosbie, "Three-dimensional radiative transfer with polarization in a multiple scattering medium exposed to spatially varying radiation", J. Quant. Spectrosc. Radiat. Transfer **57**(1), 81-105 (1997).

[139] H. H. Tynes, G. W. Kattawar, E. P. Zege, I. L. Katsev, A. S. Prikhach, L. I. Chaikovskaya, "Monte Carlo and multicomponent approximation methods for vector radiative transfer by use of effective Mueller matrix calculations", Appl. Opt. **40**(3), 400-412 (2001).